Changes in the Mn 2p3d RIXS during operando OER experiment by $NiMn_2O_4$

M. al Samarai [1], A. Hahn [1], O. Rüdiger [1], J. Miyawaki [2], Y. Harada [2], S. DeBeer [1]
[1] *Max Planck Institute for Chemical Energy Conversion,*
Stiftstrasse 34−36, 45470 Mülheim an der Ruhr, Germany
[2] *Institute for Solid State Physics, The University of Tokyo,*
Kashiwa, Chiba 277-8581, Japan

Introduction:

Splitting of water by utilization of sunlight is a clean and sustainable solution to reduce the environmental issues caused by the emission of fossil fuels. However, to realize an efficient solar induced water oxidation cycle, a highly active water oxidation catalyst is required. Within this context, in recent years, manganese-oxide-based systems have been widely investigated for photochemical reactions [1-4].
However, in order to meet the required specifications, there is an increased need to understand the catalytic background and improve the activity and stability of the catalysts. By increasing our knowledge about the morphology, dispersion, and electronic structure of elements involved in the catalytic active phase, we will be able to design better catalyst materials for the water oxidation reaction. We planned to study the role of manganese-site during the operando electrochemical oxidation of water by the graphene supported $NiMn_2O_4$ system by measuring the Mn 2p3d RIXS. This powerful technique in combination with 2p FY-XAS can determine the accurate strength of the 3d spin−orbit coupling, distortions in symmetries, and superexchange interactions, leading to predictions of the strengths of these effects interactions.

Samples, experiment method, equipment used, experiment/measurement conditions

In the first stage of the beamtime Mn 2p3d FY XAS of the dry catalyst sample was measured followed by the resonant emission from the main absorption peak positions. Then for the operando experiment the $NiMn_2O_4$ catalyst was first dispersed in ethanol solution and after a sonication step drop-casted on a Au-coated Si_3N_4 membrane.

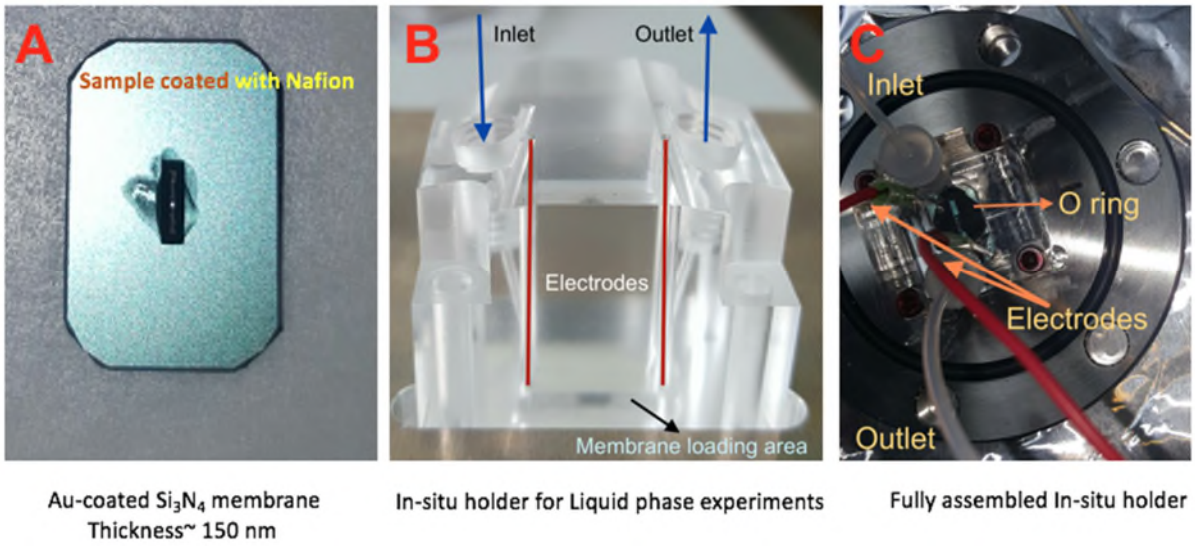

Figure 1: Overview of the applied Si_3N_4-membrane (A) and the assembled sample-holder used for the in-situ water oxidation experiments (B and C).

For the in-situ reaction the loaded Si_3N_4 membrane was loaded in a specially designed holder for liquid phase reactions as shown in Figure 1. The holder of this electrochemical cell is leak-tight and allows for both continuous flow of water while and application of current for electrochemical reaction.
During the subsequent steps the reactor was filled with the liquid cell is filled with 0.1 M KOH solution and the changes in the Ni-oxide compounds was measured by Mn 2p3d RIXS. During this in-situ

reaction the fresh sample was firstly wetted in 0.1 M KOH solution without applying a potential (0 V). Then during the subsequent of the experiment, the sample was voltage/bias was applied at 0.8 V, 1.5 V, and 1.8 V.

Results:

The obtained Mn L_3-edge absorption spectra for the fresh, wet, and 1.8V Catalyst as well as a combination of the reference manganese oxides (MnO, Mn_2O_3, Mn_3O_4, α-MnO_2) and manganese oxyhydroxide (MnOOH) are shown in Figure 2. As it is evident from the figure the XAS already confirms that the catalyst at its fresh/dry state is a Mn(II) Oh and upon wetting the manganese site is oxidized to Mn (IV). Interestingly the manganese at its catalytic active state is not a oxyhdroxy compound but rather a high valent oxide.

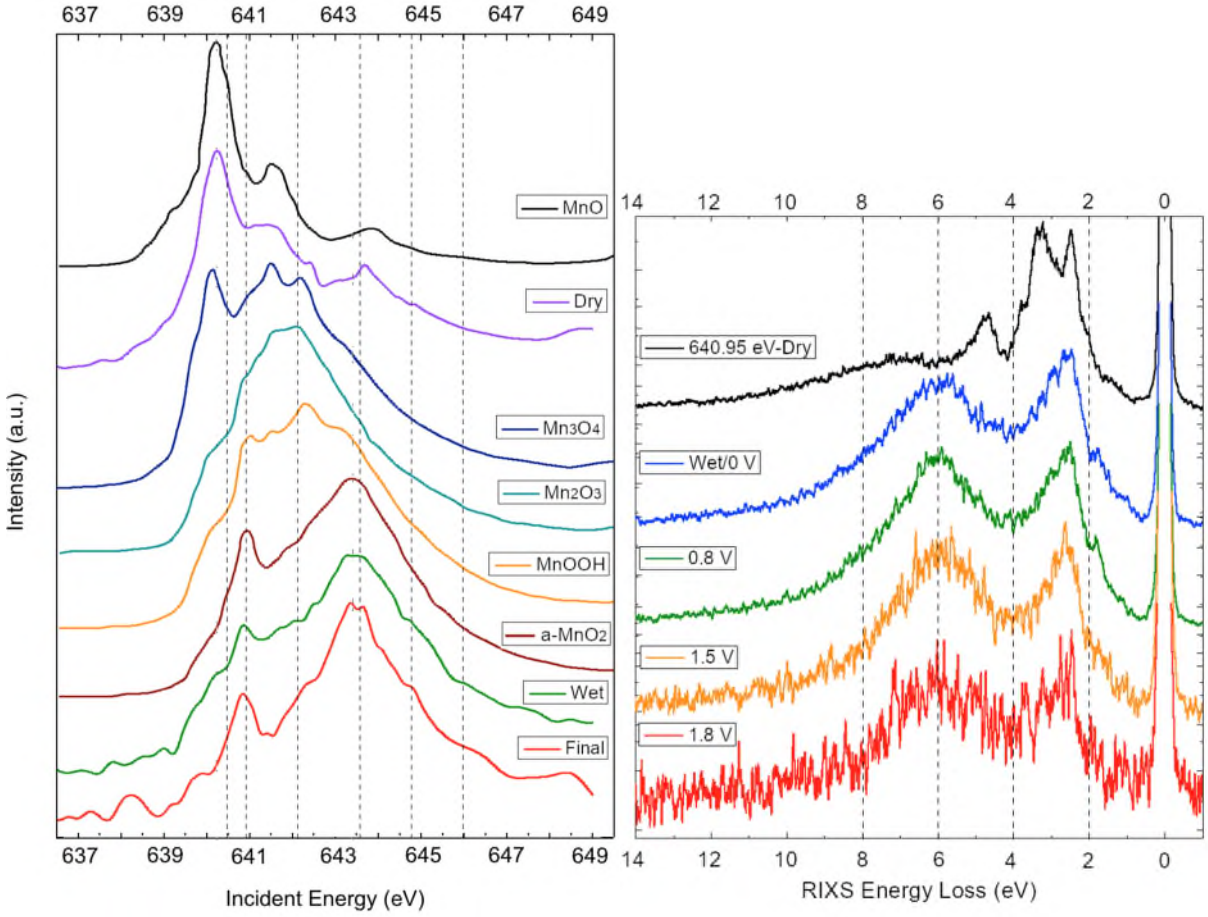

Figure 1: (Left) Mn L3-edge of the NiMn2O4 sample during various steps of the Electrochemical oxygen evolution reaction (OER). In addition, L-edge spectra of various manganese- oxides and oxyhydroxides are added as reference. In Right the Mn 2p3d RIXS energy Loss from the 640.95 eV absorption feature is plotted as a function of reaction condition during operando Echem OER.

Conclusions:

The Manganese site in the fresh/dry catalyst is a MnO-like compound with Mn(II) at octahedral site. However, interestingly both the XAS as well as the RIXS data confirm that upon immersion in 0.1M KOH solution Mn is oxidized to Mn (IV) oxide resembling the structure of a α-MnO_2. After the electrochemical oxidation, the $Ni^{(II)}$ component is partially transformed into Ni^{2+} species with larger CF (10Dq) parameter. We suggest that at high potentials and under OER conditions Mn (IV) is formed and not the as previously speculated Mn(III) OOH species that is formed by application of potentials at basic pH conditions. Hence confirming that the catalytic active site is rather the nickel site.

Photoelectron nano-spectroscopy of reactive ion etching-induced damages to the trench sidewalls and bottoms of 4H-SiC trench-MOSFETs

[1]Masaharu Oshima and [2]Naoka Nagamura
[1]*Institute for Solid State Physics, The University of Tokyo, Tokyo, Japan,*
[2]*National Institute for Materials Science (NIMS), Tsukuba, Ibaraki, Japan*

Silicon carbide has attracted great attention in order to be applied to high-power devices for devices that depict low power consumption, low on-resistance, and high blocking voltage[1], because of its superior material properties such as high voltage endurance and saturation velocity. Recently, 4H-SiC metal-oxide-semiconductor field-effect transistors (MOSFETs), especially trench-gate MOSFETs have been regarded as one of the most promising device structures to reduce on-resistance because of their high cell density and the lack of a junction-FET region. Furthermore, the non-polar 1-100 plane (m-plane) of 4H-SiC can offer the highest channel mobility among various SiC crystal planes and can be used as a channel plane for the trench sidewall in trench-gate MOSFETs. However, only a few reports have been published regarding the effects of MOS channel planes, considerably affecting the MOS channel properties and the overall MOSFET performance. So, we have attempted to characterize the trench sidewalls in terms of chemical and electronical properties by 3D-Nano-ESCA.

Samples were SiC trench structures having a width of 0.6 μm and a depth of 2.0 μm fabricated by reactive ion etching (RIE) with a gas mixture of SF_6, Ar, and O_2. The RIE etching rate of SiC was approximately 350 nm/min. The cross-sectional SEM observations revealed that the verticality, i.e., the tilted angle of the trench sidewalls was about 85°, which is approximately at a distance of 5 degrees from the m-plane. SiC trench structures are cleaved to expose the sidewall for the channel region of a trench MOSFET. We performed scanning photoelectron emission microscopic (SPEM) measurements using a three-dimensional nanoscale electron-spectroscopy chemical analysis (3D nano-ESCA) system that was installed at BL07LSU of SPring-8. The lateral and energy resolutions were set to 100 nm and 300 meV, respectively, at an excitation photon energy of 1000 eV. Figure 1 shows schematic of SPEM measurements, and AFM image of SiC trench sidewall.

F 1s and C 1s photoelectron spectra shown in Fig. 2 revealed that around 2 nm-thick homogeneous carbon-rich layer containing 1%-2 % F forms on the SiC sidewalls. This may be caused due to the re-deposition of RIE reaction products, CF_4, and SiF_4 components observed in F 1s spectra under appropriate conditions to fabricate the trench walls that are approximately vertical using RIE. From the deepest point (X=1.8 μm) to the shallowest point (X=0.1 μm), among the RIE products (CF_4 and SiF_4) the heavier SiF_4 may be re-deposited near the bottom of the sidewall, while the lighter CF_4 component is more likely to be re-deposited near the exit or surface. Oshima[2] reported that on the Si (001) bottom surface etched by RIE with the C_2F_6 gas both CF and CF_2 components were clearly detected at approximately 287.5 and 288.8 eV of binding energy, respectively, along with a dominant C-C bond at approximately 284.2 eV, indicating that the chemical shifts of the CF and CF_2 components from the C-C component are approximately 3.3 and 4.6 eV, respectively. Therefore, the 289.5 eV peak in Fig. 2 can be allocated to the CF_2 component, whereas the peak at 286.9 eV may be attributed to the CF component. Further, a carbon-rich layer having a thickness of about 2.4 nm is also formed on the bottom of the SiC trench, suggesting the possibility of selective etching of Si from the SiC substrates.

It is important to characterize the RIE-induced defects on the as-etched and annealed

surfaces of the trench sidewalls in order to fabricate trench MOSFETs that depict high channel mobility. Band bending features can be evaluated by measuring the Si 2*p* binding energy of the SiC components, because the energy difference between the Fermi level and valence band maximum (VBM) for the *n*-type 4H-SiC is calculated to be 3.06 eV and the energy difference between VBM and the Si 2*p* binding energy is reported to be 99.5 eV for 4H SiC[3]. Therefore, the Si 2*p* binding energy of 101.1 eV that is measured for the sidewall corresponds to a band bending of 1.50 eV, as depicted in Fig. 4. In the previous study, deep-level transient spectroscopy (DLTS) analysis of 4H-SiC irradiated with 9 MeV electron beam has revealed mainly four traps: EH1 (0.41 eV below the conduction band minimum (CBM)) , Z1/Z2 (0.68 eV), EH3 (0.71 eV) and EH7 (1.54 eV)[4]. Further, theoretical calculations using DFT (density functional theory) reportedly revealed that the dominant EH7 trap can be attributed to the presence of positively charged carbon vacancies (V_C^+) whose energy level is 1.73 eV below the CBM. Based on these experiments and calculations the observed band bending of 1.50 eV may be attributed to the dominant EH7 trap or to the positively charged carbon vacancy (V_C^+).[5] Further study including DLTS and other defect characterization techniques is required to reach definitive conclusions.

We'd like to thank D. Mori, A. Takigawa, A. Otsuki, S. Konno, Y. Takahashi, M. Kotsugi and H. Nohira for their collaborations.

REFERENCES:

[1] J. A. Cooper *et al.*, IEEE Trans. Electron Devices **49**, 658 (2002).
[2] M. Oshima, Surf. Sci. **86**, 858 (1979).
[3] B.L. Zhang et al., Appl. Phys. Lett. **93**, 072110 (2008).
[4] L. Storasta et al., J. Appl. Phys. **96**, 4909 (2004).
[5] M. Oshima, N. Nagamura *et al.*, e-J Surf. Sci. Nanotech. **16**, 257 (2018).

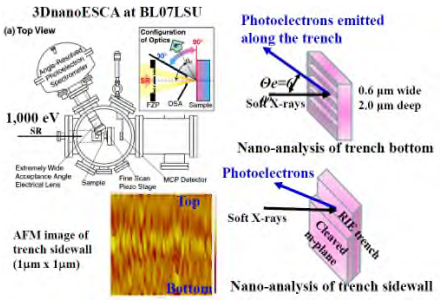

Fig. 1. Schematic of SPEM measurements, and AFM image of SiC trench sidewall.

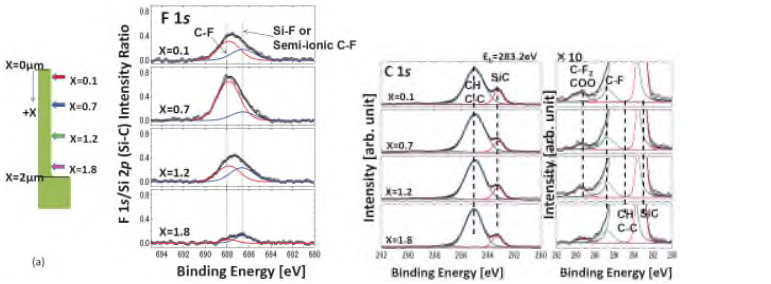

Fig. 2. F 1*s* and C 1*s* photoelectron spectra with the deconvoluted components from four different positions of the SiC trench sidewall.

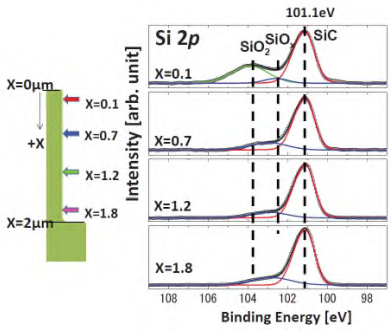

Fig. 3. Si 2*p* photoelectron spectra with the deconvoluted components from four different positions of the SiC trench sidewall.

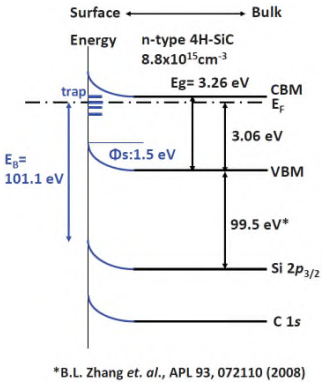

Fig. 4. Schematic of a band diagram for the m-plane SiC sidewall caused by RIE.

TRANSIENT PHOTOEXCITED STATES OF ORGANIC MOLECULES IN ORGANIC PHOTOVOLTAICS

Kenichi Ozawa[a], Susumu Yamamoto[b], Marie D'angelo[c], Ro-Ya Liu[d], Yuto Natsui[e], Naoya Terashima[e], Hiroo Kato[e], and Iwao Matsuda[b]

[a]*Department of Chemistry, Tokyo Institute of Technology,* [b]*The Institute for Solid State Physics, The University of Tokyo,* [c]*Institut des NanoSciences de Paris,* [d]*Institute of Physics, Academia Sinica,* [e]*Department of Advanced Physics, Hirosaki University*

Introduction

Organic solar cells are composed of p- and n-type organic molecules, which absorb an incoming light to form electron-hole pairs (excitons). The electron-hole charge separation, then, proceeds at the boundary between the p- and n-type molecular domains, and separated charge migrates to the electrodes to generate electricity. Quenching of the excitons and electron-hole recombination are causes to lower the efficiency of the light-to-electricity conversion. Thus, it is important to understand details of the photoexcited carrier behavior especially at the p/n organic heterojunctions as well as at the organic/electrode heterojunctions for pursuing solar cells with higher conversion efficiency. However, very little is known about the behavior of the photoexcited carriers at these heterojunctions [1,2].

In the present study, time-resolved soft X-ray photoelectron spectroscopy (TRXPS) has been used to examine carrier dynamics of a phthalocyanine (Pc)/C_{60}/TiO_2(110) hetero-junctions, which mimic a p-type-layer/n-type-layer/buffer-layer structure of a typical organic solar cell (Fig. 1).

Experimental

The TRXPS measurements were carried out at BL07LSU of SPring-8. The measurement system was composed of the laser system, which provides high-power and high-repetition-rate laser pulses for a pump light, and the photoelectron spectroscopy system, by which time-resolved measurements of the synchrotron-radiation (SR) excited spectra were possible [3]. Visible and ultraviolet laser pulses with wavelengths of 800 nm and 400 nm, respectively, were irradiated on the Pc/C_{60}/TiO_2(110) sample, and C 1s spectra were measured at various delay times between 0.1 ns and 4 μs. The Pc/C_{60}/TiO_2(110) heterojunctions were fabricated in situ by depositing a monolayer-thick Pc (CuPc or TiOPc) on to also a monolayer-thick C_{60} film on the TiO_2(110) substrate surface.

Results and Discussion

The C 1s spectrum consists of two components; one from C_{60}, which form a sharp narrow peak at 284.6 eV, and the other from Pc, which has a rather broad lineshape (a left panel in Fig. 2). Upon irradiation of the UV light at 400 nm, both peaks temporarily shift to the higher-binding-energy side. A magnitude of the shift is as large as 20 meV at the delay time of 0.1 ns. For the C 1s peak of C_{60}, the peak shift is diminished gradually to around 10 meV as the delay time is lengthened up to 4 μs. On the other hand, no clear time

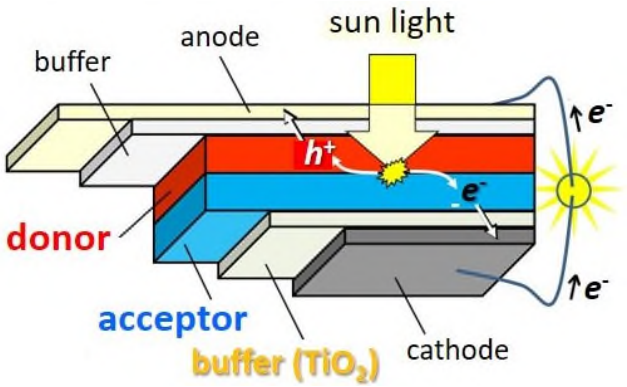

Fig. 1 A schematic of a typical structure of a solar cell. Donor and acceptor layers are fabricated by p-type and n-type organic molecules, respectively, in an organic solar cell.

dependence was observed for the Pc peak, possibly because of a large uncertainty of the peak position. The same peak shifts were also induced when the visible light at 800 nm was used. More interestingly, a difference of the center atom(s) of Pc (either Cu or TiO) do not affect the UV-induced shift of the C 1s spectrum. Such an insensitivity implies that the same excited states should be generated.

The mechanism of the peak shift of both components is shown in Fig. 2. The cause of the C 1s peak shift towards the higher-binding-energy side is understood by the formation of a cationic state of both C_{60} and Pc as a result of the transfer of the excited electrons in the LUMO levels of the molecules to the conduction band of TiO_2. This electron transfer should be spontaneous because the LUMO level of Pc is higher than that of C_{60} and both LUMO levels are higher than the conduction band minimum of TiO_2 (a middle panel of Fig. 2). This energy level alignment is the same even if the center atom of Pc is replaced from TiO to Cu, though the absolute energy difference between the LUMO level of Pc and that of C_{60} is different. It is noted that, although the absorbance of the light by the molecules depends on the photon energy (800 nm versus 400 nm), the reason for insensitivity to the photon energy is unknown so far.

An interesting finding of the present study is that the long lifetime of the UV-induced excited states (more than 4 μs) is realized once the charge separation is completed. This indicates that the electron-hole recombination is efficiently suppressed at the interface between TiO_2 and C_{60} as well as between C_{60} and Pc, although the energy level alignment prefers the electron-hole recombination. A minimal orbital overlap between the heterojunctions is suggested. This is a great advantage for high-efficient solar cells.

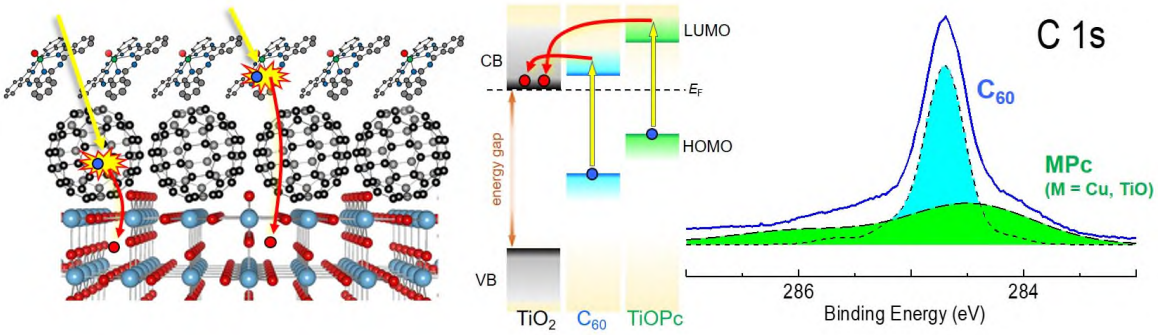

Fig. 2 Schematics of photoexcitation and charge separation processes in the Pc/C_{60}/TiO_2(110) system in a real space (left) and in an energy space (middle). The C 1s spectrum, whose lineshape is reproduced by the C_{60} and Pc components (right).

References

[1] T. Arion *et al.*, Appl. Phys. Lett. **106**, 121602 (2015); **107**, 019903 (2015).
[2] K. Ozawa *et al.*, Org. Electron. **31**, 98 (2016).
[3] S. Yamamoto *et al.*, J. Synchrotron Rad. **21**, 352 (2014).

AMBIENT-PRESSURE X-RAY PHOTOELECTRON SPECTROSCOPY STUDY OF HYDROGEN ADSORPTION AND ABSORPTION ON PALLADIUM-SILVER ALLOY

Jiayi Tang[1], Susumu Yamamoto[2], Takanori Koitaya[3], Yuki Yoshikura[2], Kozo Mukai[2], Shinya Yoshimoto[2], Iwao Mastuda[2], Jun Yoshinobu[2]

[1]Departnment of Engineering, University of Hyogo, [2]The Institute for Solid State Physics, The University of Tokyo, [3]Institute for Molecular Science

Introduction

Pd-based alloys have been the attractive materials for the hydrogen permeation process, because they possess higher hydrogen permeability and suppress the hydrogen embrittlement compared to pure Pd bulk, especially the $Pd_{77}Ag_{23}$ alloy [1-3]. Understanding of the detailed hydrogen permeation mechanism has now become interesting for further development, as it may be useful in making the potential applications more practical and efficient. Although it has been reported that the surface process (*i.e.*, H adsorption/absorption) is the rate-limiting process during hydrogen permeation [4,5], systematic studies of this process and the interactions between hydrogen and the surface and bulk of the PdAg alloy are still scarce. The hydrogen absorption reactions occurring during hydrogen permeation in the PdAg alloy and the influences of surface composition on surface reactivity are still required to be studied.

Experimental

The $PdAg_{23}$ alloy (ϕ12.4 mm, 0.1 mm thickness) was obtained from Tanaka Kikinzoku Kogyo K.K., and the bulk composition was 77 wt% Pd and 23 wt% Ag. The clean sample surface was prepared by several cycles of Ar^+ sputtering (1 keV) for 15 min and annealing at 670-675 K for 2 min. The AP-XPS measurements were performed at the soft X-ray undulator beamline BL07LSU at SPring-8. Pure H_2 (>99.99999%) gas was introduced into an ambient-pressure gas cell, where the base pressure was below 5×10^{-10} Torr. An electron analyzer (SPECS, Phoibos 150) was assembled with a three-stage differential pumping system. During H_2 exposure at 1.5 Torr, the sample temperature was increased from 300 K to 573 K. The Pd 3*d* core-level spectra were measured at a photon energy of 447.2 eV (647.3 eV) and the Ag 3*d* core-level spectra at 480 eV (680 eV), so as to obtain the same kinetic energy of about 112 eV (312 eV) that is needed to obtain the surface (bulk) sensitive information. The probing depths (3λ) are calculated to be ~ 1.2 nm, and ~ 2.0 nm when the photoelectron kinetic energy is 112 eV and 312 eV, respectively.

Results and Discussion

Figs. 1 (a)-(e) show the Pd $3d_{5/2}$ spectra measured on the clean surface and after H_2 exposure at 1.5 Torr at 300-573 K on the PdAg alloy. The bulk and surface Pd components were observed from Pd $3d_{5/2}$ spectrum on the clean surface as shown in Fig. 1(a). The surface Pd component decreased in intensity after H_2 exposure at 300 K, and followed by the appearance of the Pd hydride component (bulk Pd-H) at 473 K. The intensity of bulk Pd-H component was further increased when the temperature was increased from 473 K to 573 K. These results indicate that hydrogen absorption in the PdAg alloy is enhanced above 473 K. This observation agrees well with the result that the hydrogen permeability of the $Pd_{0.77}Ag_{0.23}$ alloy shows a maximum in the temperature range 423-523 K [6]. It is noted that 473 K corresponds to the α-β hydride phase transition temperature of the PdAg alloy. It is inferred that hydrogen adsorption may be triggered by the lattice expansion that occurs as a result of the phase transition.

In Fig. 1 (f), the surface and bulk Ag components were observed from the Ag $3d_{5/2}$ spectrum on the clean surface, which is similar with the Pd $3d_{5/2}$ spectrum. However, the Ag

hydride component was not found after H_2 exposure. It indicates that the Pd atoms are more reactive for hydrogen absorption than Ag atoms in the bulk at 473-573 K under H_2 atmosphere at the pressure of 1.5 Torr. It is consistent with the previous DFT calculations [7] in that the pathway of the H atom involving the Pd atoms shows a lower activation barrier compared to that involving the Ag atoms.

The temperature dependence of the intensities of the Pd $3d_{5/2}$ components, Ag $3d_{5/2}$ components, and the total intensities measured at different photon energies were summarized. The total Pd $3d_{5/2}$ intensity significantly decreased at 373 K followed by a gradual increase from 473 K to 573 K, while the intensity of Ag $3d_{5/2}$ monotonically decreased with temperature. The decreases in total intensities for both the elements at 373 K were due to the increase in carbon contamination that covered the surface and caused inelastic scattering of the photoelectrons. However, further decay of the photoelectron can be neglected over 473 K since the carbon contamination was almost saturated over 473 K. The increase of Pd $3d_{5/2}$ and the decrease of Ag $3d_{5/2}$ total intensities over 473 K are a result of the hydrogen adsorption/absorption-inducing enhancement of the Pd atomic fraction on the surface. The changes in the total intensities of Pd $3d_{5/2}$ and Ag $3d_{5/2}$ were more apparent for the probing depth of ~ 1.2 nm than that for ~ 2.0 nm. The probing depth dependence indicates that a larger number of Pd atoms segregate from the bulk to a depth of ~1.2 nm rather than the depth of ~2.0 nm.

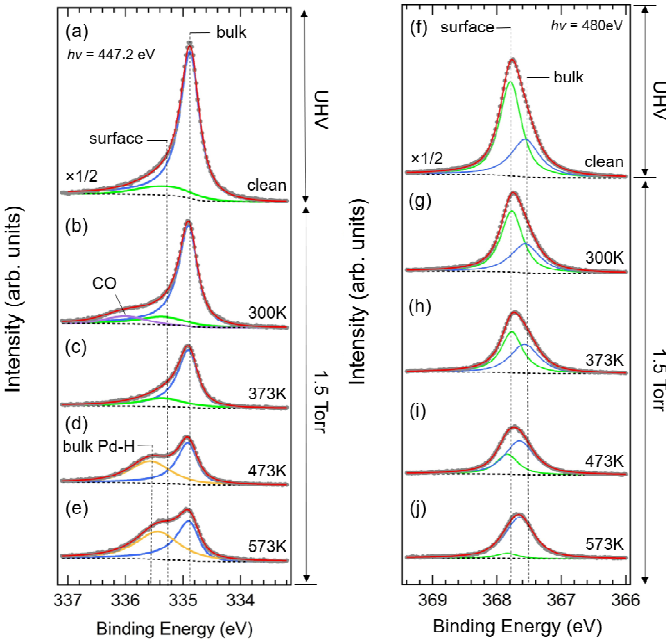

Fig. 1 Pd $3d_{5/2}$ spectra measured on (a) clean surface, and under hydrogen pressure at 1.5 Torr at (b)-(e) 300-573 K. Ag $3d_{5/2}$ spectra measured on (f) clean surface, and under hydrogen pressure at 1.5 Torr at (g)-(j) 300-573 K on PdAg alloy.

The bulk Pd-H component obtained in the depth of ~1.2 nm shows a gradual increase from 473 K to 573 K, while the bulk Pd-H component obtained in the depth of ~2.0 nm drastically increases at 473 K and saturates at 573 K. These indicate that a large amount of H atoms absorb in the bulk at 473 K, and more bulk Pd-H are formed at the depth of ~1.2 nm than at ~2.0 nm after the temperature is raised to 573 K. This may be due to the enhancement of Pd surface segregation, which provides more reactive sites for H absorption. In addition, the decrease of the bulk Pd component at 473 K is consistent with the drastic increase in the bulk Pd-H component in the PdAg alloy. On the other hand, the intensity of surface Ag decreased and the intensity of the bulk Ag and/or surface Ag-H component increased with temperature, probably due to the increase in the amount of hydrogen adsorbed on the Ag atoms.

REFERENCES

[1] A.G. Knapton, Platin. Met. Rev. 21 (1977) 44-50.
[2] C.G. Sonwane *et al.*, J. Chem. Phys. 125 (2006) 184714-1-184714-10.
[3] Z. Jovanovic *et al.*, Int. J. Hydrogen Energy 36 (2011) 15364-15371.
[4] T.L Ward *et al.*, J. Membr. Sci. 153 (1999) 211-231.
[5] J.W. Wang *et al.*, J. Membr. Sci. 503 (2016) 124-131.
[6] D. Wang *et al.*, J. Phys. Chem. B 112 (2008) 1135-1148.
[7] A.B. Padama *et al.*, Int. J. Hydrogen Energy 38 (2013) 14715-14724.

DETERMINATION OF THE ELEMENT-SPECIFIC COMPLEX PERMITTIVITY USING A SOFT X-RAY POLARIZATION MODULATOR

Y. Kubota,[1] Y. Hirata,[1] J. Miyawaki,[1] S. Yamamoto,[1] H. Akai,[1] R. Hobara,[2] Sh. Yamamoto,[1] K. Yamamoto,[1] T. Someya,[1] K. Takubo,[1] Y. Yokoyama,[1] M. Araki,[1] M. Taguchi,[3] Y. Harada,[1] H. Wadati,[1] M. Tsunoda,[4] R. Kinjo,[5] A. Kagamihata,[5] T. Seike,[5] M. Takeuchi,[5] T. Tanaka,[5] S. Shin,[1] and I. Matsuda[1]

[1]*Institute for Solid State Physics, The University of Tokyo*
[2]*Department of Physics, The University of Tokyo*
[3]*Nara Institute of Science and Technology (NAIST)*
[4]*Department of Electronic Engineering, Tohoku University*
[5]*RIKEN SPring-8 Center*

Introduction

Permittivity is a quantity that characterizes the material responses to an electric field [1]. The measurement and understanding of the permittivity of materials has been one of the highest priority tasks in science and technology. Permittivity is a complex tensor quantity with diagonal and off-diagonal components which carry the nonmagnetic and the magnetic information, respectively. Their determination has been widely made using a probe light with a polarization modulation and the measurement of the magneto-optical responses of the sample. Such an experiment is easily performed by transmitting the incident light through crystals for visible light and hard x rays [2, 3] but not for the EUV-SX region because of the absorbance of light in matter.

In this work, we developed a SX source enabling the polarization modulation of light to be performed continuously and carried out magneto-optical measurements of a buried Fe nanofilm at the Fe *L*-edge. We have succeeded in directly determining the complex permittivity tensor and we found that the first-principles calculation within the Korringa-Kohn-Rostoker (KKR) formalism gave perfect matching results.

Experiment

Continuous polarization modulation in the SX region was achieved from the segmented cross undulator, developed at SPring-8 BL07LSU [4]. The light polarization can be varied continuously from linear to right- or left-handed circular with frequency p. When using this modulated beam in magneto-optical Kerr effect (MOKE) experiments, the ellipticity (η_K) appears in signals as the p component, whereas the $2p$ component depends on the Kerr rotation angle (θ_K). By extracting the p and $2p$ components, η_K and θ_K are measurable simultaneously with high-sensitivity. A Ta (2 nm thick)/Cu (2 nm thick)/Fe (30 nm thick)/MgO heterostructure sample was used in the longitudinal MOKE (L-MOKE) experiment at room temperature. Moreover, the off-diagonal components of permittivity were calculated by the KKR-Green's function method using Machikaneyama (AkaiKKR), a KKR-CPA-LDA package [5]. Further details of the experiment and calculation can be found in our article [6].

Results and discussion

Figure 1 shows the results of the L-MOKE measurement for the Fe nanofilm taken in *s* wave and *p*-wave configuration with polarization modulation p = 12.987 Hz. Fine spectral features can be observed in the two signals. Moreover, the θ_K and η_K spectra appear to have the Kramers-Kronig relations [1]. It is notable that these η_K spectra were first directly observed in the SX energy region. Figure 2(a) shows the spectra of the off-diagonal component of permittivity

tensor (ε_{xz}) for the Fe nanofilm obtained from the L-MOKE results. We also studied the permittivity of bulk Fe (bcc) by using the first-principles calculation within the KKR formalism, as shown in Fig. 2(b). One finds good agreement between the experimental and theoretical spectra. For the first time, these results indicate that the present method and the theoretical approach are reliable in determining the off-diagonal component of permittivity in the SX energy region.

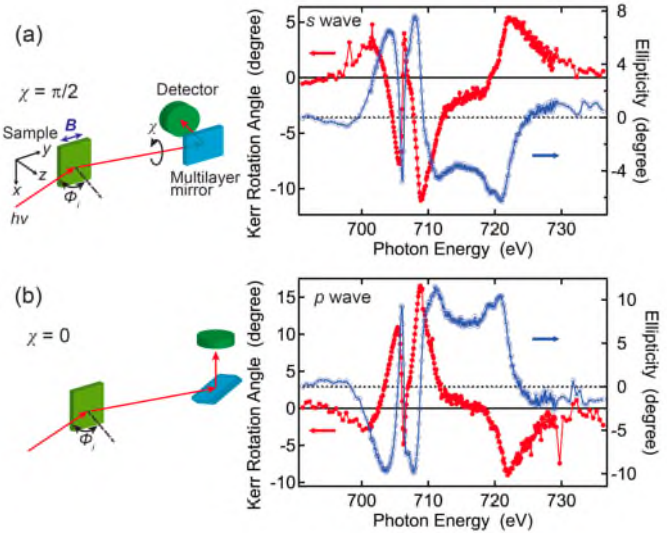

FIG. 1. Experimental setups and results of L-MOKE measurements with the polarization-modulated light for (a) the *s* wave and (b) the *p* wave. Taken from [6].

Summary

We have described the development of a SX magneto-optical spectroscope that uses a new SX source from the segmented cross undulator at SPring-8 BL07LSU. A complete data set of real and imaginary parts of the complex permittivity tensor can be determined simultaneously with high-sensitivity. Thus, faint magnetic signals are able to be detected; furthermore, the data sets are self-consistent with the Kramers–Kronig relations. This provides benefits when investigating new magnetic materials. By tuning the probe photon energy at the absorption edge, the data have element-selectivity, which is suitable for studying multi-element samples. Because the permittivity is essential for optical elements, the present procedure is significant in that it advances both EUV lithography technology and high-resolution SX spectroscopy.

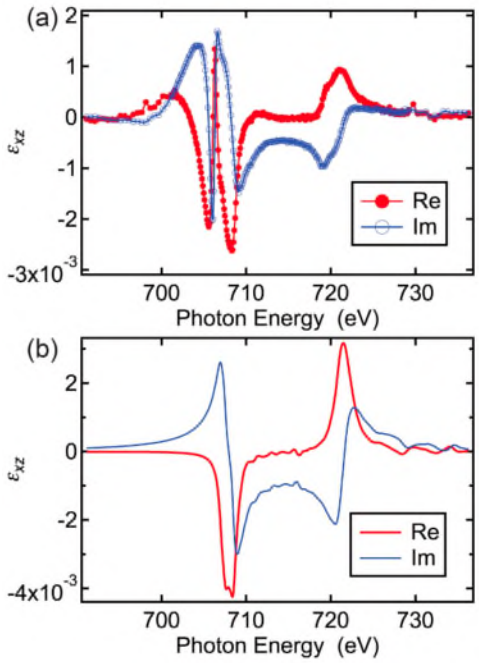

FIG. 2. ε_{xz} spectra (a) of the Fe nanofilm obtained from L-MOKE measurements and (b) of bulk Fe (bcc) obtained using the first-principles calculation within the KKR formalism. Taken from [6].

Acknowledgement

The experiment was performed using facilities of the Synchrotron Radiation Research Organization, The University of Tokyo (Proposal No. 2014A7401, 2014B7401, 2014B7473, 2015A7401, 2015B7401, 2016A7403, 2016A7504, 2016B7403).

References

[1] P. M. Oppeneer, in *Handbook of Magnetic Materials*, edited by K. H. J. Buschow (Elsevier, Amsterdam, 2001), Vol. 13.
[2] K. Sato, Jpn. J. Appl. Phys. **20**, 2403 (1981).
[3] M. Suzuki *et al.*, Jpn. J. Appl. Phys. **37**, L1488 (1998).
[4] S. Yamamoto *et al.*, J. Synchrotron Radiat. **21**, 352 (2014).
[5] H. Akai, http://kkr.issp.u-tokyo.ac.jp.
[6] Y. Kubota *et al.*, Phys. Rev. B **96**, 214417 (2017).

SOFT X-RAY SPECTROSCOPY OF SOLUTIONS ASSOCIATED WITH PLASMA-TREATEMENT IN LIQUID

Kazuo Terashima[1,2], Kenichi Inoue[1], Noritaka Skakibara[1,2], Shion Takahashi[1], Tsuyohito Ito[1], Keishi Akada[2,3], Jun Miyawaki[1,3], Yoshihisa Harada[1,2,3]

[1]*Department of Advanced Materials Science, Graduate School of Frontier Sciences, The University of Tokyo*

[2]*AIST-UTokyo Advanced Operando-Measurement Technology Open Innovation Laboratory (OPERANDO-OIL), National Institute of Advanced Industrial Science and Technology (AIST)*

[3]*Synchrotron Radiation Laboratory, The Institute for Solid State Physics, The University of Tokyo*

Flexible and wearable electronic devices have attracted much attentions. Substrates for such devices are often required to have both flexibility and functional properties. Composite materials, in which inorganic fine particles to provide functionalities are mixed with a polymer materials providing flexibility, are promising candidates for the substrate. However in general, the flexibility are greatly lowered as the mixing ratio of inorganic fine particles increases to reach desired functionalities.

In our group, to overcome such trade-off, inorganic fine particles were treated by plasma in solution. The resulted composite materials, such as plasma-treated BN particles with slide-ring materials, showed improved toughness and high thermal conductivity comparing with the composite with non-treated BN particles [1]. While the resulted composites show the excellent properties, the effect of plasma-treatment in solution has not been fully understood. Therefore, in this study, we are investigating such process with plasma in solution, for further improvement of such composite materials synthesis.

Soft X-ray emission spectroscopy (XES) of the solutions were performed at SPring-8 synchrotron radiation facility using the BL07LSU HORNET station. In the station, the original system for performing XES of liquid with a very thin (150 nm) window is equipped. Thus we have applied this spectroscopic system for investigating our solution process with plasma. The probe was O 1s, which should represent the structure of H_2O molecules. The first purpose of this study is to detect changes of water structure associated with plasma treatment.

There have been two approaches tested in the period. The first one is (a) the investigation of plasma-treated solution, and the other is (b) the investigation of solution in which plasma-treated nano-structured materials are dispersed. The nano-structured materials applied in this study were carbon nanotubes (CNTs) hydrophilized by plasma treatment in solution.

(a) Plasma-treated solutions

In the plasma treatment in liquid, various radicals, such as OH, H, and O, are generated and react with materials in the liquid, for example, BN particles in our study. Our recent analysis has shown that OH functional groups are attached on BN particles. Furthermore, charging of nanostructured materials might be useful for avoiding agglomeration of nano-structured materials. The existence of radicals and/or charges in solutions might influence the hydrogen bond network of surrounding water.

For revealing the hydrogen bond network influenced by plasma generation in solution,

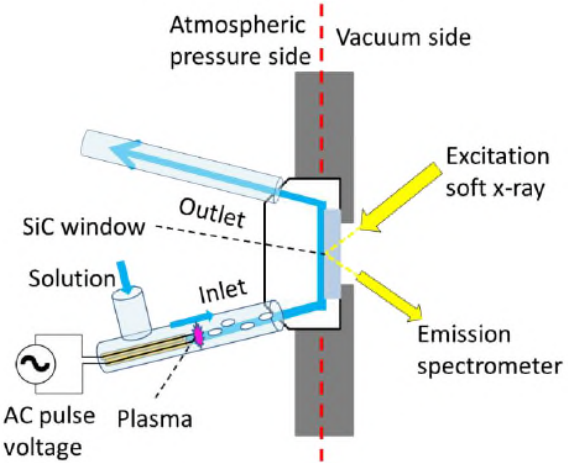

Fig. 1 Schematic diagram of XES for plasma-treated media

we have developed an in-line plasma generation system as shown in Fig. 1. In the insulator tube connecting to the XES observation cell, the plasma generator was installed. The distance between the plasma and the observation area is adjustable, and chosen at 6 cm. The flow rate of solution was 1 ml/min, resulting in the observation at 8 s after the plasma treatment. We have also investigated the solutions around 3 min and 15 min after the treatment, which were treated outside of the line for the XES spectrometer. For generating plasma, bipolar pulsed power was applied in 0.1 wt% NaCl solution. An example picture of the in-line plasma generation is shown in Fig. 2.

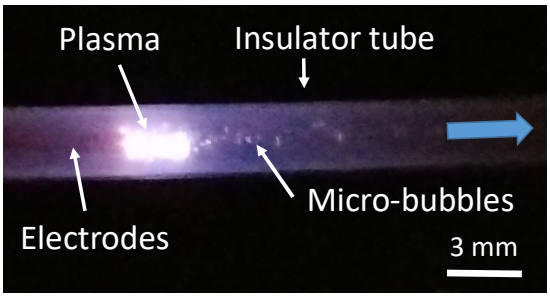

Fig. 2 Photograph of plasma in NaCl solution.

The XES spectra of raw solution and plasma-treated solutions at 8 sec, 3 min, and 15 min after plasma treatments were recorded and compared. The results indicated slight changes around 525-527 eV. Since solution temperature should be slightly elevated by plasma generation especially for the 8 sec case, the effects of temperature need to be clearly separated from the effects of charges/radicals; which will be investigated in the near future.

(b) Plasma-treated CNTs

The soft X-ray emission spectrum of the hydrophilized CNTs aqueous solution was compared with the untreated CNTs dispersion. The hydrophilization was performed with plasma in solution containing 4 wt% hydroquinone and 0.5 wt% multi-walled CNTs (average diameter and length were 20-30 nm and 0.5-2 μm) in 70 ml deionized water. The treatment time was 30 min. After the treatment, the remaining hydroquinone were rinsed away with ethanol and dried CNTs were re-dispersed in deionized water to form the solution investigated.

We see that the peak intensity associated with more distorted hydrogen bond structure ($1b_1$'') at 526.6 eV was slightly reduced with hydrophilized CNTs after normalization via the total signal intensity, while the tetrahedrally coordinated hydrogen bond peak ($1b_1$') at 525.8 eV was almost identical. We currently believe that water molecules were somewhat structured by strong hydrogen bonding around hydrophilized CNTs, reducing signals from distorted hydrogen bond configurations. Further investigations with various plasma-treatment conditions, post-treatment time, and/or CNT densities will be performed to clearly show the effect of plasma hydrophilizations.

In summary, we have successfully initiated the soft X-ray spectroscopic analysis of plasma-treated solutions, via developing an in-line plasma generation system. Furthermore, the footprint of plasma treatment in liquid was detected with CNTs, developing a unique method for further improvement of materials processing with plasma in liquid in the near future.

REFERENCES

[1] T. Goto, M. Iida, H. Tan, C. Liu, K. Mayumi, R. Maeda, K. Kitahara, K. Hatakeyama, T. Ito, Y. Shimizu, H. Yokoyama, K. Kimura, K. Ito, Y. Hakuta, K. Terashima, *Appl. Phys. Lett.* **112**, 101901 (2018).

MAGNETIZATION DYNAMICS OF Co/Pt THIN FILMS OBSERVED BY TIME-RESOLVED X-RAY MAGNETIC CIRCULAR DICHROISM MEASUREMENT

Kohei Yamamoto[1], Kou Takubo[1], Yasuyuki Hirata[1], Yuichi Yokoyama[1], Susumu Yamamoto[1], Iwao Matsuda[1], Shik Shin[1], Takeshi Seki[2], Koki Takanashi[2], Hiroki Wadati[1]

[1]*Institute for Solid State Physics, University of Tokyo,*

[2]*Institute for Materials Research, Tohoku University*

Magnetization control and magnetization reversal with light have attracted much attention because of both unresolved physical origin and potential of application to ultrafast recording media. Time-resolved x-ray magnetic circular dichroism (trXMCD) was carried out for ferrimagnetic GdFeCo alloy thin film, which shows magnetization reversal by light, and a transient ferromagnetic state was reported [1]. We measured trXMCD of Co/Pt thin films and Co and Pt atoms are coupled ferromagnetically and this material shows magnetization reversal by accumulative effect of laser pulses [2].

We used a time-resolved soft x-ray scattering and spectroscopy measuring system in Spring-8 BL07LSU [3] and measured trXMCD of perpendicularly magnetized Pt/[Co(0.4 nm)/Pt(0.7 nm)]$_2$/Sapphire multilayer thin films with a pump-probe method. The trXMCD experiment setup is shown in Fig. 1. Pump laser was circularly polarized and its wavelength and fluence were 800 nm and 1 mJ/cm^2. Probe x-ray photon energy was tuned to Co L edge and XMCD was measured by total electron yield with detecting photoelectron generated by probe x-ray. Magnetic field of ~ 0.6 T was applied with a permanent magnet. TrXMCD was observed with light and left circular polarized pump laser and probe x-ray; experiments of all 4 combinations of polarization of pump laser and probe x-ray ware conducted.

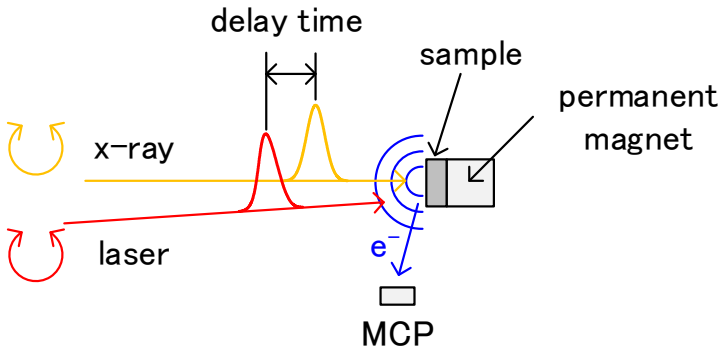

Fig.1 Experimental set up of trXMCD.

Figure 2 shows the result of trXMCD at Co L3 edge which gives the largest XMCD intensity. Fitting function is linear combination of exponential functions convoluted by the Gaussian function. There is large pump laser polarization dependence just after laser irradiation in the demagnetized transient state, which will correspond to the magnetic helicity dependence by light. In addition, the intensity of demagnetization seems to depend on pump x-ray polarizations. This may be related to the different response of orbital and spin momentum and XMCD spectra of transient state and sum rule analysis can elucidate orbital and spin momentum dynamics. TrXMCD study with higher time resolution which can be conducted in x-ray free electron laser will give us information of the mechanism of helicity dependent magnetization reversal.

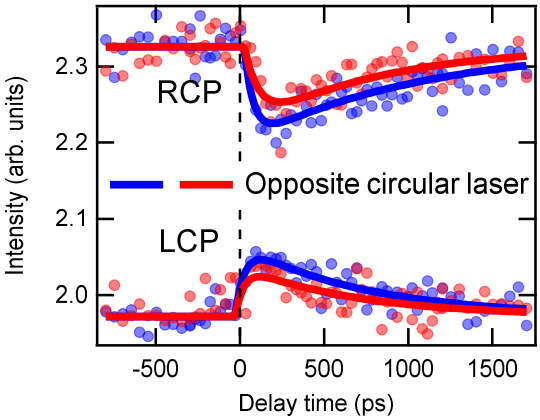

Fig.2 Result of time-resolved XMCD of circular polarized laser-induced magnetization dynamics. Solid lines are fitting curves.

REFERENCES

[1] I. Radu et al., Nature **472**, 205 (2011).
[2] C-H. Lambert et al., Science **345**, 1337 (2014).
[3] K. Takubo, K. Yamamoto et al., Appl. Phys. Lett. **110**, 162401 (2017).

RESONANT INELASTIC SOFT X-RAY SCATTERING IN MAGNETIC FIELD OF SINGLE CRYSTAL MN_2VAL AND CO_2MNSI HEUSLER ALLOYS WITH HALF-METAL-TYPE ELECTRONIC STRUCTURE

Rie Y. Umetsu[1], Hidenori Fujiwara[2], Jun Miyawaki[3,4], Yasuhiro Nakatani[2], Moeki Kawada[2], Toshiyuki Kashiuchi[2], Akinori Irizawa[5] and Shigemasa Suga[5]

[1] *Institute for Materials Research (IMR), Tohoku University*

[2] *Graduate School of Engineering Science, Osaka University, Osaka, Japan*

[3] *The Institute for Solid State Physics (ISSP), The University of Tokyo, Japan*

[4] *Synchrotron Radiation Research Organization, The University of Tokyo, Japan*

[5] *Institute of Scientific & Industrial Research, Osaka University, Osaka, Japan*

Introduction

It has been predicted that some of Mn- and Co-based Heusler-type alloys are half-metallic ferro- or ferri-magnets with the spin polarization of ~100 % around the Fermi energy (E_F) [1-3]. It is very efficient as a ferromagnetic electrode in various spin dependent devices in the field of *spintronics*, if the electrons are completely polarized around E_F. In the aspect of the fundamental investigations for the half-metallic materials, it has been considered how to show a real evidence of the characteristic electronic structure. In this work, we have first studied the detailed electronic structure and magnetic properties of a single crystal of Mn_2VAl by resonant inelastic x-ray scattering (RIXS) measurements in magnetic field. The RIXS is a bulk sensitive photon-in and photon-out spectroscopy, and very powerful to investigate such as *d-d* excitations for open shell 3*d* orbitals and magnetic excitations for spin systems as well as 2*p*-3*d* transitions in element- and symmetry-specific ways.

Experiments

a) Sample preparation

Mother ingot of Mn_2VAl was prepared by induction melting in argon gas atmosphere, and single crystal was prepared by Bridgeman method. The obtained ingot was properly annealed for homogenization and control of the degree of order. Composition of the specimen was checked by electron probe microanalyzer and magnetic properties were investigated with SQUID magnetometer. Crystal orientation was checked by the Laue method and the specimens were cut out in the stripe form with the length of 6 mm along the <100> with about 1×1 mm^2 cross section.

b) RIXS

RIXS experiments were performed at the high-resolution soft x-ray "*HORNET*" station at BL07LSU in SPring-8. In order to avoid the exposure to the atmosphere, the specimen was fractured in advance in a separate glove box in Ar gas, and then transferred into the chamber. The RIXS spectra for V and Mn 2*p* core excitation were measured with use of right and left helicity circularly polarized light at 300 K. A permanent magnet with the field of 0.25 T was installed for MCD measurement [4].

Results

Figures indicate RIXS spectra recorded for parallel and antiparallel configurations of the photon helicity at incoming photon energy, $h\nu_{in}$ of 512.5 eV (a) and 638.6 eV (b) at the V and Mn L_3 edges, respectively. Here, the parallel and antiparallel means the relation between the helicity of the circularly polarized incident light and the magnetic field direction. In order to eliminate any experimental artifacts arising from system errors, each RIXS spectrum was measured for opposite orientations of the applied magnetic field and the resulting spectra were averaged. Strong intensity peaks without any energy loss are the elastic component, and the other peaks in the larger energy loss region are the so-called fluorescence peaks.

From the comparison of these spectra between the V and the Mn L_3-edges, several significant features are recognized. The most characteristic feature is that the fluorescence peak associated with the V L_3-edge does not branch off from the elastic peak. On the other hand, there is almost no gap in the energy loss between the elastic peak and the appearance of the fluorescence peak for the Mn L_3-edge. The relative height of the fluorescence peak is noticeably smaller than that of the elastic peak in the case of V L_3-edge excitation. In addition, one notices that a broad peak is observed in the V L_3-edge excitation, while double peak features split by 1.0 ~ 1.2 eV are observed in Fig. (b) beside the elastic peak in the case of the Mn L_3-edge excitation. The RIXS-MCD, defined as the difference of the parallel and antiparallel RIXS spectra, is observed in both V and Mn L_3-edge excitations. The sign of the RIXS-MCD is opposite between the V and Mn in agreement with the ferrimagnetic character of this material.

For interpreting the observed RIXS and MCD spectra, theoretical calculations were performed by means of the density functional theory (DFT). In the case of the V 3*d* states, the partial density of states (PDOS) are found to be very small around E_F in both up and down spin states. As shown in the figure (a), the fluorescence component of RIXS in V L_3-edge does not branch off from the elastic peak. The absence of any additional fluorescence peak between the elastic peak and the peak around ~2 eV is consistent with the negligible PDOSs of the V 3*d* states. In the case of the Mn 3*d* states, however, rather complex electronic structures strongly dependent on the spin are predicted. That is, down spin states have high PDOS and up spin states have negligible PDOS around E_F. RIXS feature for the Mn L_3-edge excitation branches off really from the elastic peak, suggesting the finite PDOS at E_F of the Mn 3*d* states.

The Mn RIXS-fluorescence spectra were simulated based on the Kramers-Heisenberg formula. The sign, the shape of the Mn RIXS-MCD and the incident photon energy dependence of the intensities of the spectra are qualitatively reproduced in consistence with the half-metallic electronic states predicted by the present calculations and confirmed the absence of the up spin Mn 3*d* PDOS at the E_F.

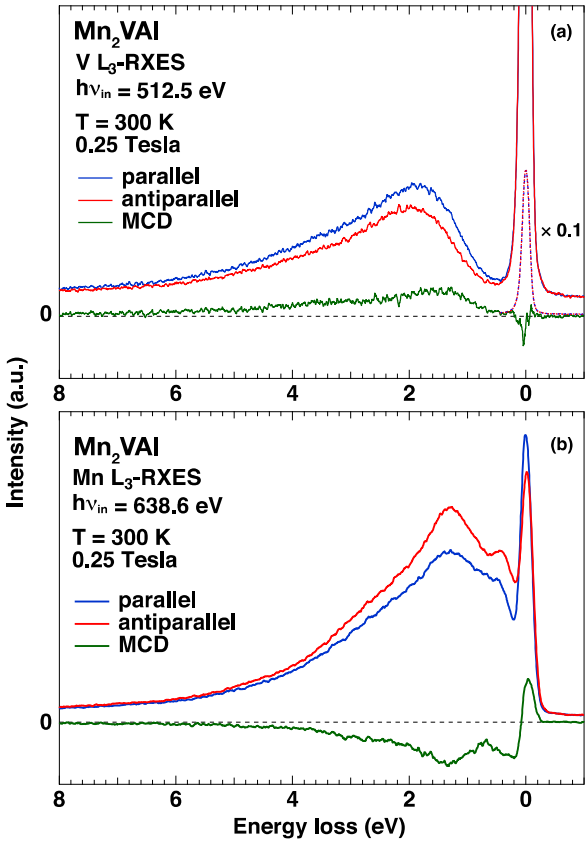

Figs. RIXS spectra recorded for parallel and antiparallel configurations of the photon helicity at incoming photon energy, $h\nu_{in}$ of 512.5 eV (a) and 638.6 eV (b) at the V and Mn L_3 edges, respectively, together with the MCD.

Acknowledgements

Theoretical calculations were performed by Oguchi group in Osaka Univ.

References

[1] R.A. de Groot, F.M. Mueller, P.G.van Engen, K.H.J. Buschow, Phys. Rev. Lett. 50 (1983) 2024-2027.

[2] J.J. Kübler, A.R. Williams, C.B. Sommers, Phys. Rev. B 28 (1983) 1745-1755.

[3] S. Ishida, S. Akazawa, Y. Kubo, J. Ishida, J. Phys. F 12 (1982) 1111-1122.

[4] J. Miyawaki, S. Suga, H. Fujiwara, H. Niwa, H. Kiuchi, Y. Harada, J. Synchro. Rad. 24 (2017) 449-455.

EXPLORATION OF CHARGE ORDER IN OVER-DOPED CUPRATE SUPERCONDUCTOR

Kenji Ishii[1], Shun Asano[2], Masumi Ashida[3], Masaki Fujita[2], Shuichi Wakimoto[4], Jun-ichiro Mizuki[3], Tadashi Adachi[5], Yoji Koike[6], Jun Miyawaki[7], Yoshihisa Harada[7]

[1]*Synchrotron Radiation Research Center, National Institutes for Quantum and Radiological Science and Technology*

[2]*Intsitute for Materials Research, Tohoku University*

[3]*Graduate School of Science and Technology, Kwansei Gakuin University*

[4]*Materials Science Research Center, Japan Atomic Energy Agency*

[5]*Department of Engineering and Applied Sciences, Sophia University*

[6]*Department of Applied Physics, Graduate School of Engineering, Tohoku University*

[7]*Synchrotron Radiation Laboratory, The Institute for Solid State Physics, The University of Tokyo*

Charge order in hole-doped cuprate superconductors had been considered as a specific phenomenon in the La-based system (La214) until several years ago. Recently, resonant x-ray scattering experiments clarified that the charge order exists in other systems and it is universally observed in cuprate superconductors including electron-doped systems [1]. Since order parameter and correlation length of the charge order is found to decrease in the superconducting phase, the charge order is regarded as a competing phase of superconductivity. While the charge order in the hole-doped system has been reported in limited hole concentration from the underdoped to optimum-doped regime so far, we observed in our O K-edge RIXS experiment performed last year that intensity of elastic or quasi-elastic scattering is enhanced in a spectrum of overdoped $La_{1.75}Sr_{0.25}CuO_4$ (LSCO250) at $\mathbf{q}$ = (0.12, 0), which might be an indication of the charge order [2]. It is important to verify whether the charge order exists in the overdoped regime to understand the relation to the superconductivity. Therefore, we have performed an extended O K-edge RIXS experiment of $La_{1.75}Sr_{0.25}CuO_4$ focusing on the momentum around $\mathbf{q}$ = (0.12, 0). We also measured another overdoped sample, $La_{1.796}Sr_{0.204}CuO_4$ (LSCO204). Superconducting transition temperature is slightly suppressed near the hole concentration of LSCO204 [3] and it may be due to the competition between the superconductivity and the charge order.

The experiment was performed using the HORNET spectrometer at BL07LSU of SPring-8. Total energy resolution was 150 meV. The crystals were cleaved in the air just before the measurement and σ-polarized x-rays were irradiated on the *ab*-plane of the crystal which was kept at the base temperature of the spectrometer (~ 15 K). The *ac*-plane was parallel to the horizontal scattering plane and momentum transfer in the CuO_2 plane (q) was scanned by rotating the crystal along the vertical *b*-axis. We tuned the incident photon energy to a peak at the pre-edge of x-ray absorption spectrum. This peak corresponds to the O 2*p* state of doped holes and RIXS at the incident photon energy should be sensitive to the spatial modulation of the doped holes. Energy-resolved RIXS has the advantage for observing charge order over energy-integrated resonant x-ray scattering, which is commonly referred to as resonant elastic x-ray scattering (REXS) because RIXS enables one to discriminate true signal of the charge order from other huge spectral weight, such as *d-d* excitations and fluorescence. Given that doped holes predominantly occupy the O 2*p* orbitals in the cuprates, very high sensitivity to the charge order is expected in O K-edge RIXS.

Figures (a) and (b) show O K-edge RIXS spectra of LSCO250 and LSCO204, respectively. The intensity of the spectra is normalized to the high-energy spectral weight (1.5-11.5 eV) which shows fluorescence behavior. Signal of the charge order should appear as elastic or quasi-elastic scattering near the origin of energy, if it exists. At a higher energy region, momentum-dependent spectral weight is observed and it is ascribed to intra-band charge excitations [4]. In order to focus on the momentum dependence of near the origin of energy, we integrate the intensity of the RIXS spectra between -0.2 and 0.2 eV and plot it as a

function of momentum in Figure (c). We also plot the result of LSCO250 taken last year (open circles) [2], where intensity is enhanced at q = (0.12,0). Unfortunately, the enhancement in LSCO250 is not reproduced in the finer momentum scan in this experiment for both positive and negative *h* (filled circles). The enhancement is not observed in LSCO204 either. Note that larger intensity near *h* = 0 comes from specular reflection, which is not related with the charge order. Since beam position on the sample changes with momentum in our experimental condition, we speculate that the enhanced intensity observed in the experiment last year is due to an accidental surface condition and it is probably an experimental artifact. B. We conclude that the charge order in overdoped LSCO is unlikely in our experimental resolution.

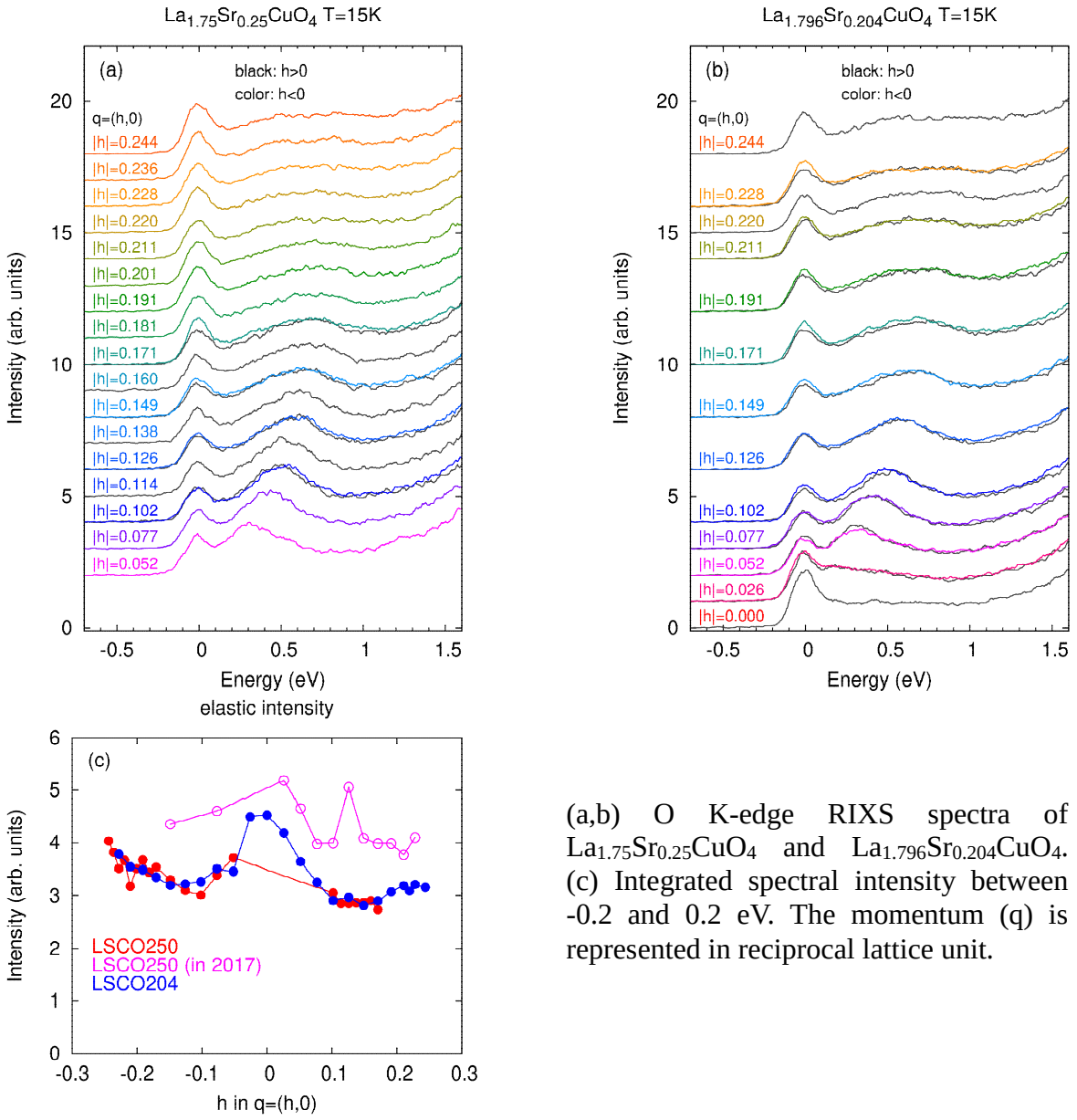

(a,b) O K-edge RIXS spectra of $La_{1.75}Sr_{0.25}CuO_4$ and $La_{1.796}Sr_{0.204}CuO_4$. (c) Integrated spectral intensity between -0.2 and 0.2 eV. The momentum (q) is represented in reciprocal lattice unit.

REFERENCES

[1] R. Comin et al., Annu. Rev. Condens. Matter Phys. **7**, 369 (2016).
[2] K. Ishii et al., ACTIVITY REPORT OF SYMCHROTRON RADIATION LABORATORY 2016.
[3] T. Kawamata et al., Phys. Rev. B 62, R11981 (2000).
[4] K. Ishii et al., Phys. Rev. B 96, 115148 (2017).

TEMPERATURE-DEPENDENT CHARGE EXCITATION IN HOLE-DOPED CUPRATES AND ITS POSSIBLE COUPLING TO SPIN CORRELATION

Kenji Ishii[1], Shun Asano[2], Masumi Ashida[3], Masaki Fujita[2], Shuichi Wakimoto[4], Jun-ichiro Mizuki[3], Tadashi Adachi[5], Yoji Koike[6], Jun Miyawaki[7], Yoshihisa Harada[7]

[1]*Synchrotron Radiation Research Center, National Institutes for Quantum and Radiological Science and Technology*

[2]*Intsitute for Materials Research, Tohoku University*

[3]*Graduate School of Science and Technology, Kwansei Gakuin University*

[4]*Materials Science Research Center, Japan Atomic Energy Agency*

[5]*Department of Engineering and Applied Sciences, Sophia University*

[6]*Department of Applied Physics, Graduate School of Engineering, Tohoku University*

[7]*Synchrotron Radiation Laboratory, The Institute for Solid State Physics, The University of Tokyo*

Charge and spin are the key ingredients of electron. The former governs electric properties while the latter is responsible for magnetism of materials. In correlated electron systems, such as doped Mott insulators and heavy Fermion systems, interplay of spin and charge plays a crucial role for their physical properties. Even though spin correlation is not long-ranged, the correlation can affect behavior of charge. For example, unconventional superconductivity in some of the correlated electron systems is induced by the spin correlation. Here we try to investigate the interplay of spin and charge in hole-doped cuprates from the charge excitation spectra using resonant inelastic x-ray scattering (RIXS). It is noted that the cuprates are suitable for the purpose because energy scale of charge and spin dynamics is high. Even though the energy resolution of RIXS has been improved significantly in recent years, the high energy scale is still a prerequisite for observing a main portion of momentum dependence of charge and spin excitations with RIXS.

The experiment was performed using the HORNET spectrometer at BL07LSU of SPring-8. We chose O K-edge rather than Cu L_3-dge because we recently found that the former is sensitive to the charge excitation of the hole-dope cuprates [1]. Total energy resolution was 150 meV. The crystals were cleaved in the air just before the measurement and σ-polarized x-rays were irradiated on the *ab*-plane of the crystal. The *ac*-plane was parallel to the horizontal scattering plane and momentum transfer in the CuO_2 plane (q) was scanned by rotating the crystal along the vertical *b*-axis. We tuned the incident photon energy to a peak at the pre-edge of x-ray absorption spectrum. This peak corresponds to the O 2*p* state of doped holes and RIXS at the incident photon energy should be sensitive to the spatial modulation of the doped holes. We measured four Sr (hole) concentrations of the hole-doped cuprate $La_{2-x}Sr_xCuO_4$ (x = 0.120, 0.180, 0.204, and 0.250).

Figure shows the temperature (T) dependence of O K-edge RIXS spectra of $La_{2-x}Sr_xCuO_4$ at low momentum transfer [q = (0.052,0)] and high momentum transfer [q = (0.149,0) or (0.160,0)]. The spectra is normalized to the intensity of fluorescence spectral weight at higher energy. Peak feature of the charge excitation at the momentum transfer is observed 0.2-0.3 eV and 0.6-0.7 eV, respectively. Temperature dependence is qualitatively similar in the sample with x = 0.180, 0.204, and 0.250; the peak feature weakens with increasing temperature at low q. In contrast, the spectrum at high q is almost independent of temperature. Because the peak energy of the charge excitation discussed in this work is much higher than the energy scale of temperature, k_BT, where k_B is the Boltzmann constant, it is unlikely that the temperature variation of the charge excitation is thermal effect. We speculate that it comes from a characteristic of strong electron correlation, more precisely, charge dynamics coupled with spin correlation. In the superconducting cuprates, exchange interaction (J) between the spin in the CuO_2 plane is about 0.1 eV and spin excitation extends up to ~ 3J [2,3] which matches the energy of temperature-dependent charge excitation. Given that J is larger than k_BT, the spin

correlation should be robust at 400 K. However it is limited to the case for the undoped cuprate; the spin correlation is destroyed by the motion of the doped holes and it can vary at lower temperature than J/k_B. In the sample with x = 0.180, 0.204, and 0.250, spin correlation weakens with increasing temperature. Concomitantly, lifetime time of the charge excitation becomes short and the peak feature disappers. Looking at the spectra at 400 K carefully, weak peak feature remains in x = 0.18 and 0.204 while it broadens out into flat spectral shape in x = 0.25. It indicates that the spin correlation weakens further at higher hole doping as expected. We note that similar temperature dependence of the charge excitation is also reported in the Cu L_3-edge RIXS of electron-doped $Nd_{2-x}Ce_xCuO_4$ [4] and it may be the same origin.

Finally, we discuss the result of x = 0.12 in Fig. (a). Though the spectral weight at 0.2-0.3 eV decreases with increasing temperate in the low q data, it is only slightly. It does not form a peak feature in contrast to the case of other samples. Since the spectral weight at high q is comparable in the four samples, the weak signal at low q in x = 0.12 cannot be ascribed to the low hole concentration. It might be related to charge density wave and/or pseudogap which are inherent around the hole concentration. Further finer doping dependence would be necessary to understand the difference between x = 0.12 and other samples with higher doping.

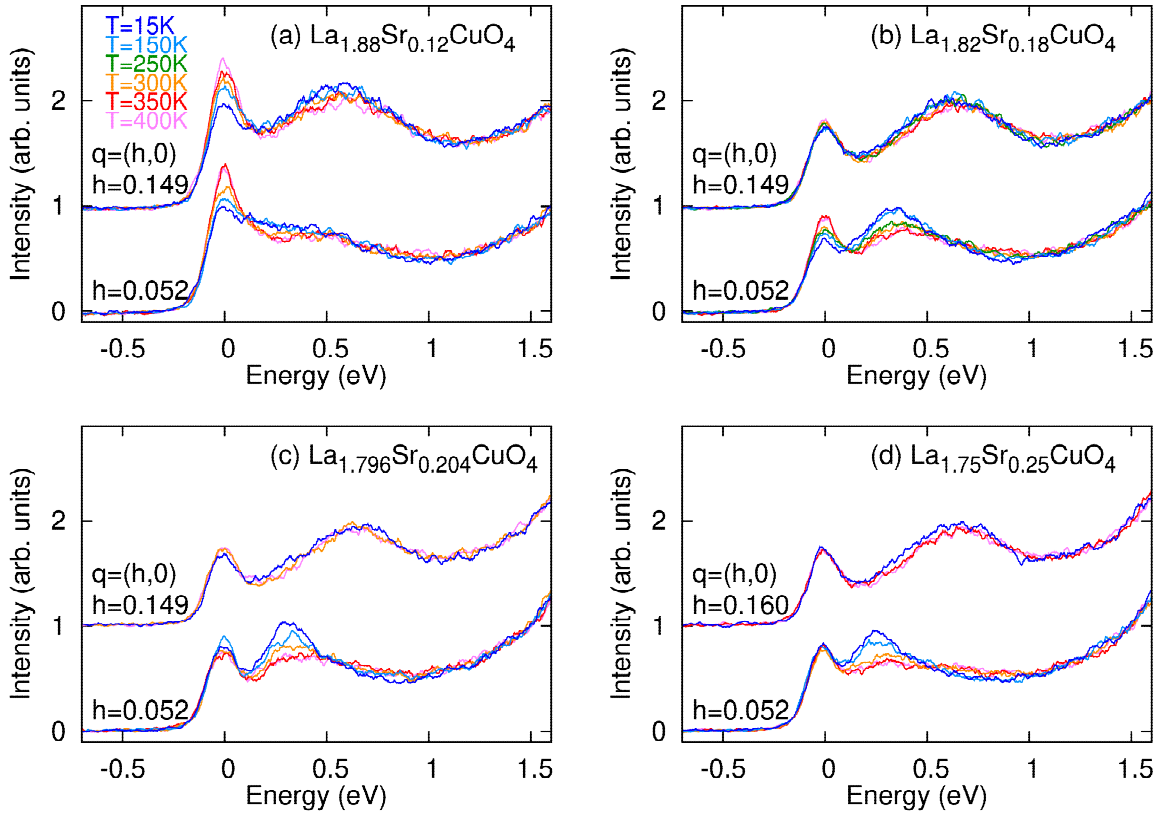

Temperature dependence of O K-edge RIXS spectra of $La_{2-x}Sr_xCuO_4$. The momentum transfer within the CuO_2 plane (q) is represented in reciprocal lattice unit.

REFERENCES

[1] K. Ishii et al., Phys. Rev. B 96, 115148 (2017).
[2] M. Le Tacon et al., Nat. Phys. 7, 725 (2011).
[3] M. P. M. Dean et al., Nat. Mater. 12, 1019 (2013).
[4] W. S. Lee et al., Nat. Phys. 10, 883 (2014).

Room-temperature magnetoelectric effects on C_2O_3 studied by SX-RIXS under electric and magnetic fields

H. Fujiwara[1], T. Kashiuchi[1], M. Kawada[1], A. Irizawa[2], J. Miyawaki[3,4], S. Suga[2]
[1] *Graduate School of Engineering Science, Osaka University, Osaka, Japan*
[2] *Institute of Scientific & Industrial Research, Osaka University, Osaka, Japan*
[3] *Institute for Solid State Physics (ISSP), The University of Tokyo, Japan*
[4] *Synchrotron Radiation Research Organization, The University of Tokyo, Japan*

Introduction

Cr_2O_3 is an antiferromagnetic insulator below the Néel temperature of 307 K and crystalizes corundum structure [1]. Since this magnetic order breaks the time and space inversion symmetry, it is well known to show the linear magnetoelectric (ME) effect, in which magnetic moment (electric polarization) is induced in proportion to an applied electric field (magnetic field). Most important is that the ME effect is realized at room temperature. Therefore, it attracts considerable attention for the spintronic application. Nevertheless, the mechanism of the linear ME effects is still under debate. In order to reveal the origin of the ME effect, we have performed resonant inelastic x-ray scattering (RIXS) at the Cr 2*p* edge to study the electronic structures and magnetic properties under magnetic and electric fields.

Experimental

RIXS measurements were performed at the SPring-8 BL07LSU HORNET end-station, where a high resolution soft x-ray spectrometer and a compact magnetic circuit are installed [2,3]. Total energy resolution was set to about 200 meV at Cr 2*p* edge, and the experimental temperature was set to 300 K. To apply both electric and magnetic fields, we have developed a compact manipulator, which allows us to apply the bias voltages of 300 V in the gap of 11 mm between the truncated cone of the magnetic circuit. To apply the magnetic field along the crystal *c*-axis. The Pt electrode is evaporated on the single crystalline Cr_2O_3 with 5-nm thick.

Results and discussions

Figure 1 shows the linear polarization dependence of Cr 2*p* RIXS spectra obtained at incoming photon energy ($h\nu_{in}$) of 581.4 eV without any external fields. The electric field (E) of the incoming photon was set to the parallel and perpendicular to the crystal *c*-axis. The *dd*-excitations are observed in the wide energy range of 1.6 eV to 7 eV, which are well captured by the configuration-interaction cluster model calculation based on the multiplet ligand-field theory [4]. In the spectral simulation, the polarization for both incoming and outgoing photons is averaged. The strong linear polarization dependence is observed in the *dd*-excitation peaks around 1.8 eV and 2.6 eV, which indicates the anisotropy of the electronic structure.

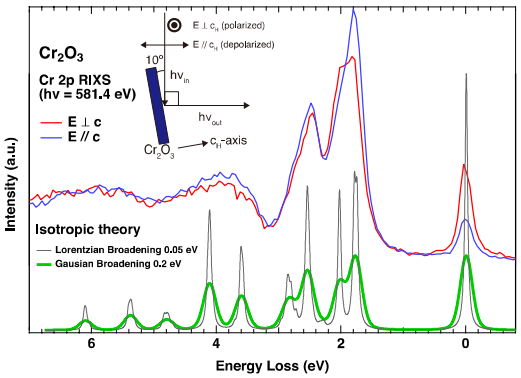

Fig. 1
Linear polarization dependence of Cr 2*p* RIXS spectra recorded without external fields. The configuration interaction calculation with realistic ligand field is displayed in the bottom.

To capture the ferromagnetic signal induced by the external electric field, we have measured circularly polarization dependence of RIXS under both fields. Figure 2 shows the RIXS spectra obtained at $h\nu_{in}$ = 585.7 eV with right and left circularly polarized photons, denoted as RCP and LCP. Under applying voltages of 1 MV/m, the RIXS spectra show the noticeable difference between RCP and LCP spectra for the *dd*-excitation around 2 eV, which is possibly due to the induced magnetic moment.

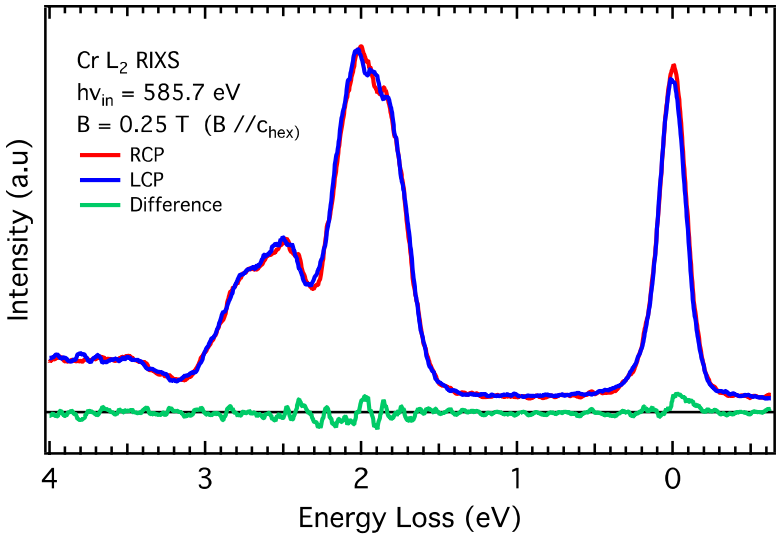

Fig. 2 Magnetic circular dichroism in Cr 2*p* RIXS under the bias voltage of 1 MV/m.

Summary

We have performed the Cr 2*p* RIXS of Cr_2O_3 with and without external fields. The linear polarization dependence in the RIXS spectra shows the clear difference in the *dd*-excitation peaks around 2 eV, indicating the anisotropic electronic structure. This *dd*-excitation shows small dichroic signals for the circularly polarized photons under the bias voltage of 1 MV/m, which is possibly due to the ferromagnetic moment induced by the ME effect.

REFERENCES

[1] A. Iyama and T. Kimura, Phys. Rev. B **87**, 180408(R) (2013).
[2] J. Miyawaki, *et al.*, J. Synchrotron Rad. **24**, 449 (2017).
[3] J. Miyawaki, *et al.*, Phys. Rev. B **96**, 214420 (2017).
[4] M. W. Haverkort, *et al.*, Phys. Rev. B **85**, 165113 (2012).

Development of Automatic θ-2θ Scan for REXS and RIXS

J. Miyawaki, Y. Kosegawa, K. Yamazoe, Y.-T. Cui, and Y. Harada

[1]*Institute for Solid State Physics, The University of Tokyo*

The RIXS spectrometer at HORNET end-station in SPring-8 BL07LSU has been updated for angle-resolved RIXS experiment since the end of 2015. In the shutdown from January to March 2016, the end-station was rebuilt, and all the components for the rotation of the spectrometer was installed. After the commissioning in the 2016A term, the RIXS spectrometer successfully acquired the new function: rotation for RIXS scan in the momentum space. This system features ultra-high precision rotation of the spectrometer and the in-vacuum continuous variation of the scattering angle by an originally-designed chamber with three rotary stages [patent pending: PCT/JP2017/003553]. In the 2016A and 2016B terms, the precision of the rotation was measured, and it was confirmed that no optimization of the spectrometer was necessary after rotating the RIXS spectrometer, thereby enabling automatic 2θ rotation. However, the rotation of the sample (θ rotation) was not precise enough for the automatic scan. Since the x-ray irradiated position changes after rotating the sample, the optimization of the sample position was required after every θ rotation, hindering the automatic θ-2θ scan. Thus, in the 2017A term, a new software with the function of the sample position correction was developed and commissioned for the automatic θ-2θ scan. As a demonstration, Fe *L*-edge magnetic scattering of $La_{1/3}Sr_{2/3}FeO_3$ was measured.

Figure 1 shows the angle dependence of Fe *L*-edge RIXS spectra of $La_{1/3}Sr_{2/3}FeO_3$ measured by the developed automatic θ-2θ scan system. The sample position was corrected by moving the sample to the optimized sample position obtained before the θ-2θ scan. The spectra were measured at 100 K, which is well below the transition temperature of the magnetic ordering. Since the magnetic scattering was expected to be observed around 2θ=82°, 2θ was scanned from 70° to 95° with 1° step. At each 2θ angle, ~100 seconds were required to obtain one spectra, including 60-second exposure and ~40-second read-out. The rotation of θ and 2θ was completed during reading an image from a CCD detector. Thus, it took only ~45 minutes to obtain all the data set.

Figure 2 shows the integrated intensity of the elastic peak plotted against $\boldsymbol{q}$ along [111]. At 100 K, which is below the transition temperature, the magnetic scattering is clearly observed at $\boldsymbol{q}_{111}\approx 0.47$ Å^{-1}, whereas at 210 K, which is above the transition temperature, no magnetic scattering is observed. The results are in good agreement with the previous report [1], and the scan system was well verified.

The automatic θ-2θ scan enables us the quick and precise operation, providing a chance to use the RIXS spectrometer for diffraction experiments or resonant elastic x-ray scattering (REXS). By using this system, it is expected that weak scattering peaks that have been difficult to be observed by the conventional x-ray diffraction using an energy integrated detector are distinguished, as was charge density wave in cuprate superconductors probed by the RIXS spectrometer.

References

[1] J. Okamoto *et al.*, Phys. Rev. B **82**, 132402 (2010).

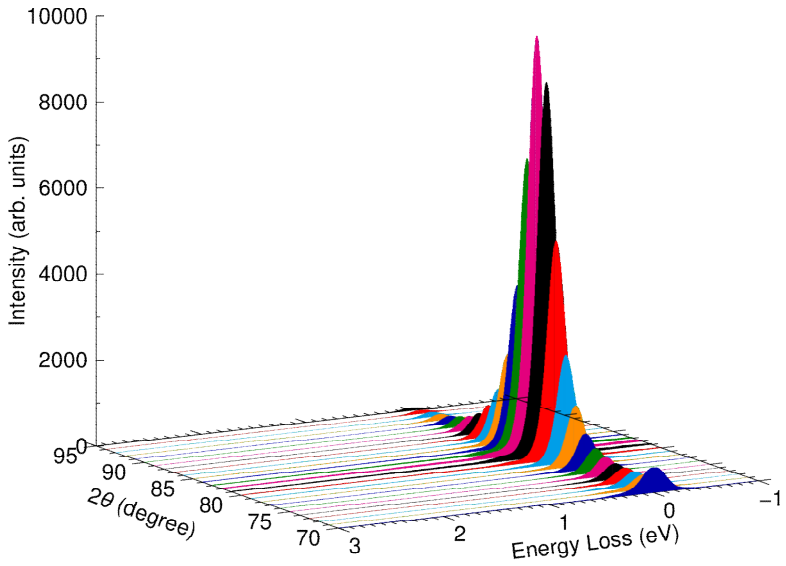

FIG. 1 Fe *L*-edge RIXS spectra of $La_{1/3}Sr_{2/3}FeO_3$ at 100K plotted against 2θ.

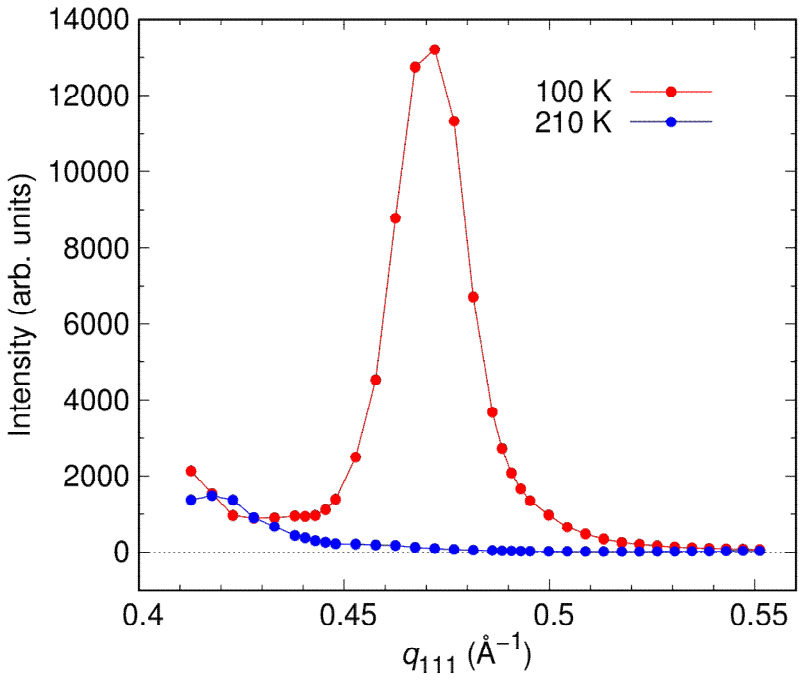

FIG. 2 Integrated intensity of elastic peak in Fe *L*-edge RIXS spectra of $La_{1/3}Sr_{2/3}FeO_3$ plotted against $\boldsymbol{q}$ along [111].

O *K*-edge XAS and RIXS study on $Bi_2Sr_2Ca_2Cu_3O_{10+\delta}$

H. Wang[1], J. Miyawaki[1,2], K Ishii[3], T. Tohyama[4], S. Adachi[2], T. Watanabe[5], S. Shin[1,2], and Y. Harada[1,2]

[1]*Graduate School of Frontier Sciences, The University of Tokyo*
[2]*Institute for Solid State Physics, The University of Tokyo*
[3]*National Institutes for Quantum and Radiological Science and Technology*
[4]*Department of Applied Physics, Tokyo University of Science*
[5]*Graduate School of Science and Technology, Hirosaki University*

Introduction

Cuprate superconductors have widely been studied from various viewpoints, such as high-temperature superconductivity, pseudo-gap, charge density wave. In non-doped cuprates, only the spin degree of freedom determines the dynamics of the low-energy electron. In carrier-doped cuprates, both charge and spin degrees of freedom contributes to the electron dynamics, and it is essential to investigate the properties of both charge and spin. Recently, the spin degree of freedom was visualized as energy dispersion of spin excitation by Cu *L*-edge RIXS, and the importance of RIXS has been strongly recognized [1]. For charge excitations, dispersive excitations at sub-eV region were observed by Cu *L*-edge RIXS in electron-doped $Nd_{2-x}Ce_xCuO_4$, and interpreted as charge excitations of electrons doped to the upper Hubbard band of Cu sites [2]. However, in hole-doped $La_{2-x}(Br,Sr)_xCuO_4$, excitations at sub-eV region have not been reported, and the interpretation has been debated. In contrast to the Cu *L*-edge, Ishii *et al.* found clear charge excitations in O *K*-edge RIXS of the hole-doped $La_{2-x}(Br,Sr)_xCuO_4$ [3], and demonstrated the capability of O *K*-edge RIXS to probe the charge excitation of a hole doped to the oxygen site. Thus, in order to further prove that the charge excitation is a ubiquitous elementary excitation like charge density wave in both hole- and electron-doped cuprates, we carried out a comprehensive study of this collective mode on optimally hole-doped $Bi_2Sr_2Ca_2Cu_3O_{10+\delta}$ by using O *K*-edge RIXS. $Bi_2Sr_2Ca_2Cu_3O_{10+\delta}$, which has three superconducting CuO_2 layers, shows the highest T_c=110 K. Therefore, $Bi_2Sr_2Ca_2Cu_3O_{10+\delta}$ also gives an opportunity to discuss the relationship between charge excitation and higher Tc.

Experimental

O *K*-edge RIXS was measured at the HORNET end-station of BL07LSU in SPring-8. The total energy resolution was set to be ~130 meV, and the scattering angle was fixed at 135°. Excitation energy was set at 528.1 eV, where a mobile carrier peak is observed [4]. σ polarization was used. Measurement temperatures were 50 K, which was well below the superconducting transition temperature T_c, 95 K, and 150 K.

Results and discussion

Figure 1 shows O *K*-edge RIXS spectra and *E*-*k* maps of optimally hole-doped $Bi_2Sr_2Ca_2Cu_3O_{10+\delta}$. The broad peaks at sub-eV region shifts to higher energy with larger momentum transfer, showing positive dispersion. The peak positions were extracted by the peak fitting analysis. Figure 2 shows the extracted peak positions of the dispersive excitations. Linear dispersions were clearly obtained at the range from 0.5 to 1.0 eV. Because the spin-flip excitation is forbidden at the O *K*-edge, the low-energy paramagnons are unlikely to be the origin of the dispersive excitation. Since the energy loss at large $\boldsymbol{q}$ exceeds over 0.8 eV, the possibility of magnetic excitations can also be excluded. Then, these dispersive excitations should most likely be ascribed to the intra-band charge excitations.

Summary
The angle dependence of O *K*-edge RIXS spectra of optimally hole-doped $Bi_2Sr_2Ca_2Cu_3O_{10+\delta}$ was measured at 50, 95, and 150 K. Dispersive collective modes were observed and assigned to the charge excitation. For this compound, similar dispersive excitation has also been observed in Cu *L*-edge RIXS but having clearly different energy dispersion [5]. Although it is difficult to connect the orbital-dependent charge excitation with superconductivity, the charge excitation may offer an idea of recognizing the dynamic property of the charge in $Bi_2Sr_2Ca_2Cu_3O_{10+\delta}$. Theoretical calculation, by explaining those highly itinerant electrons, will be conducted to understand the charge excitations observed by O *K*-edge.

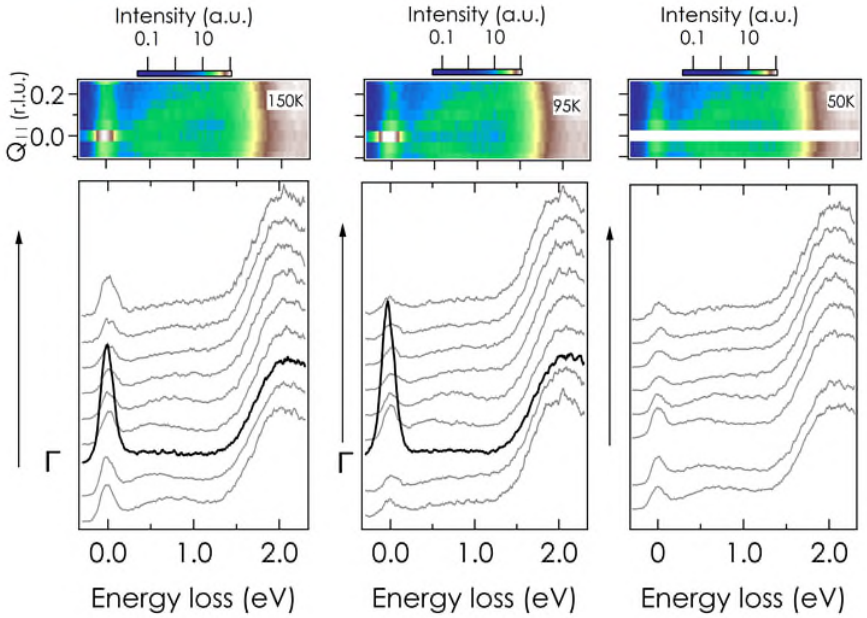

FIG. 1 O *K*-edge RIXS spectra and *E*-*k* maps of $Bi_2Sr_2Ca_2Cu_3O_{10+\delta}$ measured at 150, 95, and 50 K. Thick lines indicate the spectra at Γ point, and spectra at large ***q*** are offset vertically for clarity

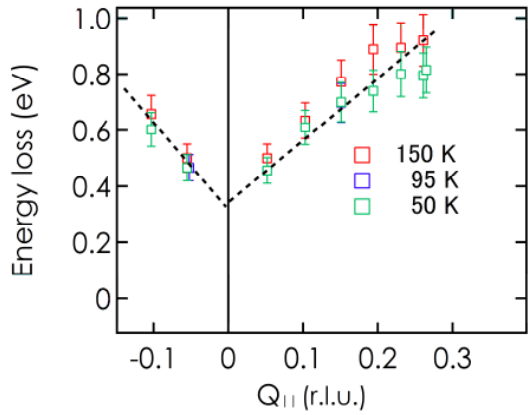

FIG. 2 Peak positions of dispersive excitations at sub eV region.

References
[1] M. P. M. Dean, J. Magn. Mag. Mater. **376**, 3 (2015).
[2] W. S. Lee *et al.*, Nat. Phys. **10**, 883 (2014).
[3] K. Ishii *et al.*, Phys. Rev B **96**, 115148 (2017).
[4] C. Chen *et al.*, Phys. Rev. Lett. **66**, 104 (1991).
[5] J. Miyawaki *et al.*, in preparation.

Demonstration of Resonant Inelastic Diffraction by $La_{1/3}Sr_{2/3}FeO_3$

J. Miyawaki and Y. Harada

Institute for Solid State Physics, The University of Tokyo

Dispersions of electronic-band and elementary excitations, such as orbiton, magnon, and phonon can be measured by resonant inelastic x-ray scattering (RIXS) [1]. This indicates that the process of RIXS (absorption and emission) can be described as a single scattering event, and the momentum is conserved during the process. In other words, when a core electron with a momentum of $\boldsymbol{k}$ is excited to a conduction band, and an electron in a valence band radiatively decays to the core hole, the interference of x-ray emission from different atoms results in Bragg-like diffraction, and then x-ray emission of the same momentum $\boldsymbol{k}$ is observed at a specific scattering angle. These phenomena are described by the law of energy conservation for inelastic scattering, $h\nu_{\mathrm{in}} = h\nu_{\mathrm{out}} + E_{\mathrm{h}} - E_{\mathrm{e}}$, and more general Bragg's law, $\boldsymbol{q}_{\mathrm{in}} = \boldsymbol{q}_{\mathrm{out}} + \boldsymbol{k}_{\mathrm{h}} - \boldsymbol{k}_{\mathrm{e}} + \boldsymbol{G}$, where $h\nu_{\mathrm{in}}(\boldsymbol{q}_{\mathrm{in}})$ and $h\nu_{\mathrm{out}}(\boldsymbol{q}_{\mathrm{out}})$ are energy (momentum) of incident and scattered x ray, E_{h} ($\boldsymbol{k}_{\mathrm{h}}$) and E_{e} ($\boldsymbol{k}_{\mathrm{e}}$) are energy (momentum) of hole in valence band and electron in conduction band, and $\boldsymbol{G}$ is a reciprocal lattice vector. In the case of elastic scattering ($E_{\mathrm{h}} = E_{\mathrm{e}}$、$\boldsymbol{k}_{\mathrm{h}} = \boldsymbol{k}_{\mathrm{e}}$), the latter formula becomes $\boldsymbol{q}_{\mathrm{in}} = \boldsymbol{q}_{\mathrm{out}} + \boldsymbol{G}$ and is recognized as standard Bragg's law.

The explanation above is for the dispersion of elementary excitations measured by RIXS and based on Bragg-like diffraction for inelastic scattering. If Bragg-like and Bragg's diffraction interferes each other, Bragg's diffraction defined by structural order is expected to assist inelastic scattering due to the elementary excitation. This interference was first suggested by resonant soft x-ray diffraction experiment of a La/B_4C multilayer [2], where the authors gave a plausible interpretation that the inelastic scattering by the 5*p* level of lanthanum was assisted by Bragg diffraction from the lattice of the multilayer. However, the scattered x ray was detected by a diode, and it was not clear whether the inelastic scattering was really enhanced. It should now become possible to verify the enhancement of the inelastic scattering channel by using momentum-resolved RIXS. Therefore, we performed momentum-resolved Fe *L*-edge RIXS of $La_{1/3}Sr_{2/3}FeO_3$, which shows magnetic scattering by resonant soft x-ray diffraction [3], at HORNET end-station in SPring-8 BL07LSU.

Figure 1 shows RIXS spectra of $La_{1/3}Sr_{2/3}FeO_3$ measured at 100 K, which is below the transition temperature (190K) of the magnetic order, with $2\theta = 82°$. The intensity of the elastic peak is clearly enhanced due to resonant magnetic scattering. Figure 2 shows the integrated intensity of elastic (+0.11 – −0.11 eV) and inelastic (+10.0 – +0.8 eV) peaks of RIXS spectra measured at 100 K and 210 K, which are below and above the transition temperature of the magnetic order. A peak at $\boldsymbol{q}\approx 0.47$ Å^{-1} for elastic peak at 100 K corresponds to the resonant magnetic scattering and is in good agreement with the previous report [3]. By contrast, the intensity plot for the inelastic peaks at 100 K shows a peak at $\boldsymbol{q}\approx 0.445$ Å^{-1}. The peak at $\boldsymbol{q}\approx 0.445$ Å^{-1} disappeared at 210 K as the magnetic scattering disappeared. Although the origin of the momentum shift, 0.025 Å^{-1} is not yet determined, steep dispersion (small $\Delta\boldsymbol{q}$ and large energy loss) excludes the possibility of *dd* excitations or charge transfer excitations. The results strongly indicate that the peak at $\boldsymbol{q}\approx 0.445$ Å^{-1} derives from the enhancement of the inelastic scattering by the Bragg's diffraction from the magnetic order, and thus resonant inelastic diffraction was well demonstrated.

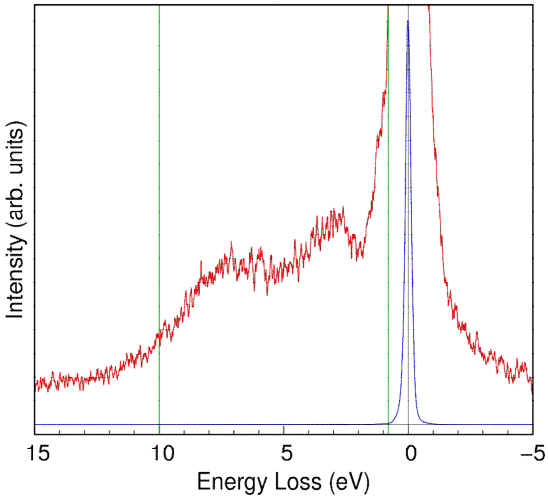

FIG. 1 RIXS spectra of $La_{1/3}Sr_{2/3}FeO_3$ measured at 100 K and 210 K. Green vertical lines indicate the integration area for the inelastic peaks.

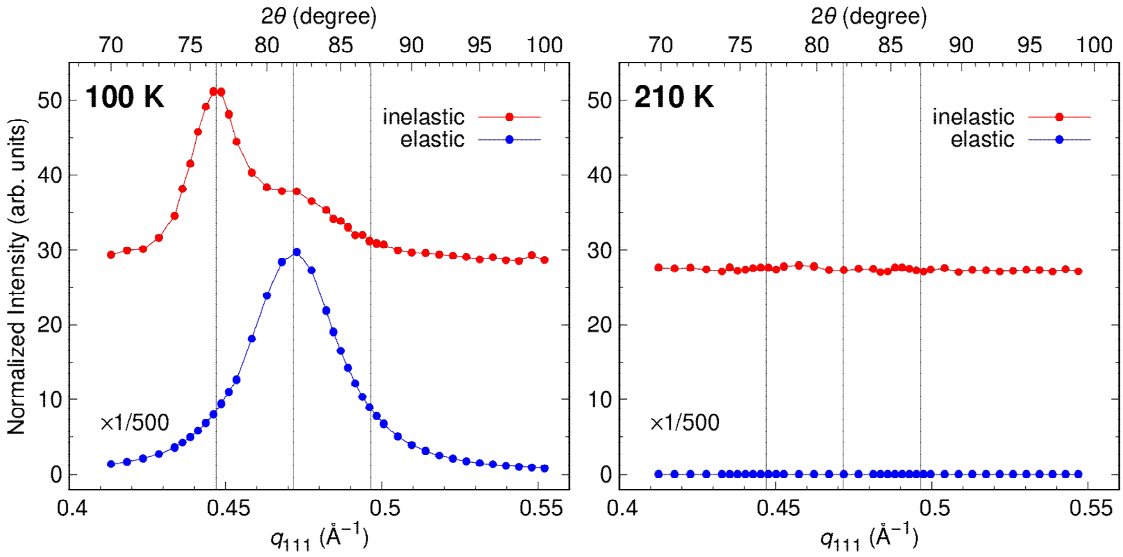

FIG. 1 Integrated intensity of elastic and inelastic peaks in RIXS spectra of $La_{1/3}Sr_{2/3}FeO_3$ measured at 100 K and 210 K plotted against q_{111}. Spectra are offset vertically for clarity.

References

[1] L. J. P. Ament *et al.*, Rev. Mod. Phys. **83**, 706 (2011).
[2] J.-M. Andre *et al.*, Optics Comm. **255**, 267 (2005).
[3] J. Okamoto *et al.*, Phys. Rev. B **82**, 132402 (2010).

TIME-RESOLVED PHOTOELECTRON HOLOGRAPHY STUDY OF SILICENE

Kouichi Hayashi[1,2], Artoni Kevin R. Ang[1], Koji Kimura[1], Yuichiro Fukatsu[1], Akito Asano[1], Takahiro Tsukada[1], Yohei Okuda[3], Takahiro Yonezawa[4], Antoine Fleurence[4], Yukiko Yamada-Takamura[4]

[1]*Structural Physics Laboratory, Nagoya Institute of Technology, Nagoya, Japan*
[2]*Frontier Research Institute for Materials Science, Nagoya Institute of Technology, Nagoya, Japan*
[3]*Okayama University, Okayama, Japan*
[4]*School of Materials Science, Japan Advanced Institute of Science and Technology, Ishikawa, Japan*

[Introduction]

Silicene, the two-dimensional Si-based counterpart of graphene, is expected to possess similar remarkable electronic properties. It was recently demonstrated that 2D epitaxial silicene forms through surface segregation on ZrB_2/Si(111) surfaces [1]. Because silicene easily buckles, it can form different structures with varying sp^2/sp^3 hydridization ratios and can be used to tailor its unique electronic properties [1,2]. Photoemission studies have shown that the Si atoms of epitaxial silicene grown on ZrB_2/Si(111) occupies at least 3 chemically different sites [1,3]. In this study, we investigate the different local structures around these Si atoms using photoelectron holography (PEH). Furthermore, we also attempt to do time-resolved PEH experiments to investigate the dynamics of this material system.

[Experiment]

To do this, the silicene samples were grown in-situ in the preparation chamber of the ARTOF end station in BL-07LSU of SPring-8[4]. A ZrB_2/Si(111) substrate was first degassed in UHV, followed by annealing at 800°C. The silicene layer spontaneously forms through the segregation of the Si atoms from the substrate [1]. The silicene surface was evaluated using LEED and XPS.

For the photoemission experiments, synchrotron radiation with photon energy of 300 eV is irradiated on the sample. The angular distribution and the energy (E) of the photoelectrons are recorded by the ARTOF detector [4]. In this experiment, the angular acceptance was ±13°. To obtain a larger section of the hologram, the several holograms were recorded at varying sample orientations.

Preliminary time-resolved PEH experiments were also performed in the pump-probe scheme, using a 1.5 eV, 208 kHz pump laser, and a 300 eV synchrotron probe. First, we evaluated the effects of laser power. Then, tr-PEH at normal incidence was performed with 0.1 and 0.5 ns delay times.

[Results]

In the angle integrated Si 2p spectra shown in Fig. 1(a), 3 peak fitting components were found. These corresponded to the 3 Si positions in the model proposed for silicene/ZrB_2/Si(111) (Fig.1 (b)) [1-3]. Using the three-dimensional (x, y, E) ARTOF data, peak fitting was performed pixel-by-pixel to extract the Si 2p holograms from each peak component. The results of a preliminary data processing are shown for the B- (Fig. 1c) and A- (Fig. 1e) components of the Si 2p fitting of each pixel. Simulations of the holograms from the corresponding Si atoms are shown in Fig. 1 (d) and (f).

After applying 6-fold symmetrisation on the recorded holograms, some holographic features become visible. From the experimental holograms, clear differences can be observed between the B-peak and A-peak Si 2p PEH patterns. Furthermore, these experimental PEH patterns show good agreement with the simulated patterns.

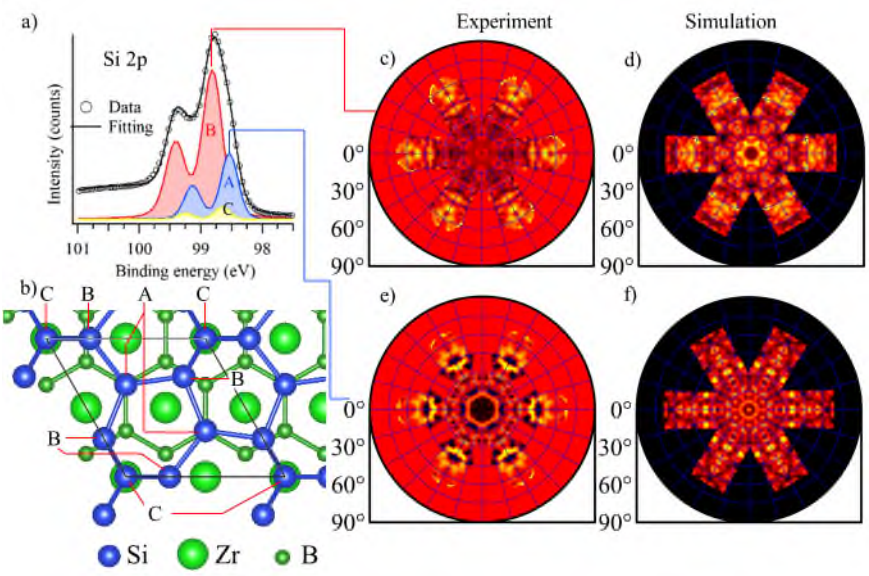

Figure 1. a) Si 2p spectra the resulting peak fitting taken at $h\nu = 300\ eV$ from the Silicene/ZrB2/Si(111) sample, b) structural model proposed in ref. [3] showing the 3 chemically unique Si positions. The Si 2p PEH taken from the B- and A- peak components are shown in c) and e), while their corresponding simulated are shown in d) and f).

We also performed preliminary time-resolved PEH experiments on the silicene sample. Fig. 2 a) show the integrated Si 2p spectra before, at 0.1 and 0.5 ns delay times after the pump laser. Fig. 2 b), c) and d) show small ±13° sections of the photoelectron hologram in the normal incidence directions at different delay times.

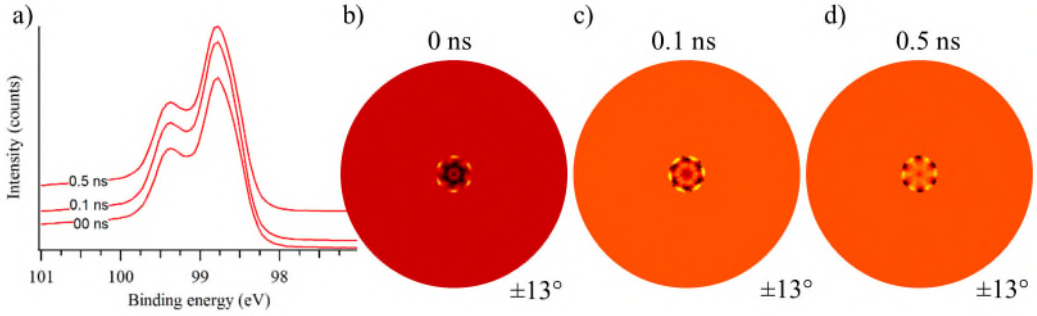

Fig. 2 a) Integrated Si 2p spectra before and after the pump laser, small sections of the Si 2p photoelectron holograms b) before the pump laser and with delay times of c) 0.1 ns and d) 0.5 ns.

Better data processing to extract the holographic signal is necessary before further detailed discussions can be made.

[Conclusions]

In this study, we performed site-selective photoelectron holography on silicene to determine the structure of the Si atoms at chemically different sites. We also attempted time-resolved PEH experiments. Further data processing is needed to quantitatively discuss the structure of silicene.

REFERENCES

[1] A. Fleurence, et al., Phys. Rev Lett. **108**, 245501 (2012).
[2] R. Friedlein and Y. Yamada-Takamura, J. Phys. Condens. Matter **27**, 203201 (2015).
[3] R. Friedlein, et al., J. Chem. Phys. **140**, 184704 (2014).
[4] M. Ogawa, et al., Rev. Sci. Instrum **83**, 023109 (2012).

High-energy-resolution transition-metal *L*-edge soft x-ray spectroscopy studies of cathode materials for rechargeable batteries using a transfer vessel without air exposure

Masashi Okubo[1,2], Takaaki Sudayama[3], Kazuki Uehara[1], Daisuke Asakura[3], Yoshihisa Harada[4], Atsuo Yamada[1,2]

[1]*Department of Chemical System Engineering, School of Engineering, The University of Tokyo,*

[2]*Elements Strategy Initiative for Catalysts & Batteries (ESICB), Kyoto University,*

[3]*Research Institute for Energy Conservation, National Institute of Advanced Industrial Science and Technology,*

[4]*Institute for Solid State Physics, The University of Tokyo*

Enhancement of the charge-discharge capacity in cathode materials for Li-ion batteries is one of the important topics to further promote electric vehicles. Li-excess layered oxides such as $Li_{1.2}Ni_{0.13}Co_{0.13}Mn_{0.54}O_2$ have capacity as high as 200-250 mAh/g, which is higher than the capacity of typical transition-metal (TM) oxide-based cathode materials like $LiCoO_2$ (~150 mAh/g). The difference is thought to be oxygen redox in addition to the TM's redox reaction in the Li-rich systems. Those redox reactions have been investigated by soft X-ray spectroscopy including X-ray absorption spectroscopy (XAS) and X-ray emission spectroscopy (XES) at the O *K* edge [1-3].

From a viewpoint of theory based on first-principle calculation, Seo *et al*. pointed out a role of isolated oxygen 2*p* orbitals in the Li-rich systems [5]. Indeed, some XAS and XES studies revealed new structures in the O *K*-edge spectra after the charge reaction. However, their attributions of the peaks in the spectra are still unclear, and the TM *L*-edge studies have been insufficient, so far. In this study, in order to clarify those subjects, we further performed soft X-ray spectroscopic studies for $Li_{1.2}Ni_{0.13}Co_{0.13}Mn_{0.54}O_2$.

$Li_{1.2}Ni_{0.13}Co_{0.13}Mn_{0.54}O_2$ powdered sample was fabricated by a solid-solution method. In addition to the pristine sample, three samples were prepared: charged to 4.4 V, fully-charged (4.8 V), and fully-discharged (2.0 V) on the first cycle. After the electrochemical expetiments, the electrode samples were taken out from coin-type cells and mounted on a sample holder in a grove box. The sample holder was transferred to the vacuum chamber by a transfer vessel to avoid air exposure. The partial-fluorescence-yield XAS experiments were carried out at BL07LSU of SPring-8 [4].

Figure 1 shows the experimental results of (a) Mn *L*-edge, (b) Co *L*-edge, and (c) Ni *L*-edge *ex situ* XAS of $Li_{1.2}Ni_{0.13}Co_{0.13}Mn_{0.54}O_2$ on the charge/discharge process. For the pristine sample (before charge), the Mn, Co, and Ni are ascribed to be tetravalent, trivalent, and divalent, respectively. From Fig.1 (a), the Mn *L*-edge XAS spectra hardly changed during the redox reaction. The Co *L*-edge XAS results indicate partial oxidation of Co from Co^{3+} to Co^{4+} during the charge at 4.4 V, because the shoulder structure on the high energy side of the Co L_3 main peak became slightly broad (Fig. 1 (b)). The Co *L*-edge XAS at 4.8 V in which the oxygen should be oxidized is the same as that at 4.4 V. Figure 1 (c) shows that the valence of Ni changes from Ni^{2+} to higher oxidation state at 4.4 V. The Ni *L*-edge spectrum at 4.8 V indicates the Ni atoms are partly reduced despite of the fully charged state. The valences of these metal ions are currently being analysed by using theoretical calculations.

Figure 1(d) shows oxygen *K*-edge XAS in the pre-edge region. The arrows in the figure indicate the spectral changes by charge-discharge processes. Spectral weight at 528 eV

increases upon the charge to 4.4 V. This change corresponds to increase of holes on the oxygen 2*p* orbitals hybridized with TM 3*d* orbitals due to TMs' oxidation of $Ni^{2+/4+}$ and $Co^{3+/4+}$. On the other hand, for the charge process from 4.4 V to 4.8 V, the intensity at 531 eV increases. This holes by oxygen oxidation is formed at higher photon energy, and independent of the TMs' redox. For the discharged state, the profile is almost the same as that for before charge.

In summary, we performed *ex situ* XAS for $Li_{1.2}Ni_{0.13}Co_{0.13}Mn_{0.54}O_2$. The XAS results exhibited significant spectral changes due to the oxygen redox. In the near future, the electronic-structure analysis by using high-resolution XES will be performed.

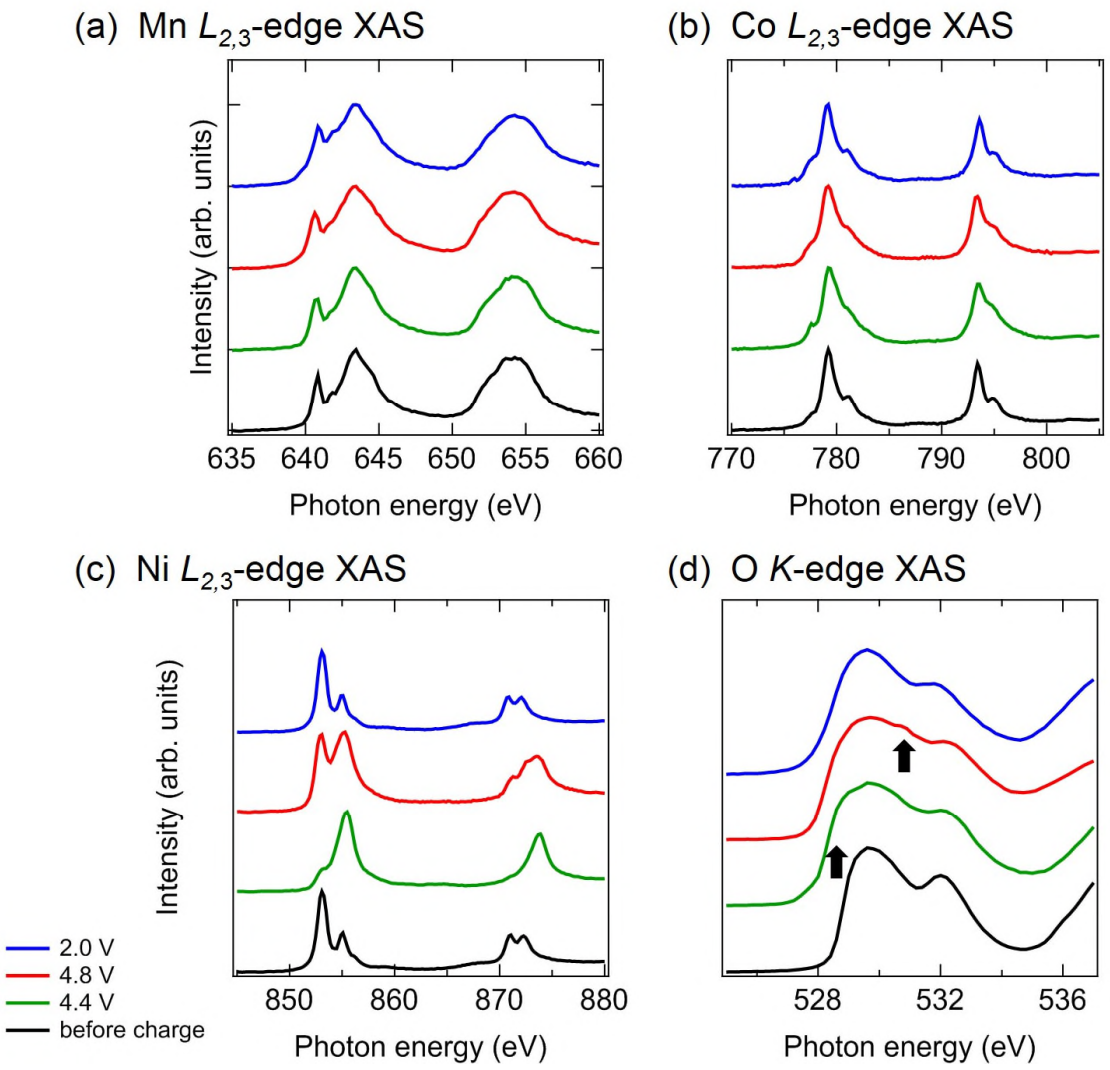

Fig. 1. (a) Mn *L*-edge, (b) Co *L*-edge, and (c) Ni *L*-edge, and (d) O *K*-edge XAS spectra for $Li_{1.2}Ni_{0.13}Co_{0.13}Mn_{0.54}O_2$ by the charge/discharge treatments.

References

[1] K. Luo *et al*., Nat. Chem. **8**, 684-691 (2016).
[2] K. Luo *et al*., J. Am. Chem. Soc. **138**, 11211-11218 (2016).
[3] D.-H. Seo *et al*., Nat. Chem. **8** 692-697 (2016)
[4] Y. Harada *et al*., Rev. Sci. Instrum. **83**, 013116 (2012).

Ion Water Interaction on the Molecular Level

Zhong Yin

Deutsches Elektronen-Synchrotron

Ion-water interaction is a fundamental process and its mechanisms are relevant for a broad range from solvation chemistry, environment to biology. Despite the obvious importance and intense research in this area there are still many fundamental open questions regarding the ions effect on the structure and dynamics of water and in turn, how water affects the structure and dynamics of the ions.

The aim of the experiment with the proposal no 2017B7551 was to investigate the ion-water interaction on the molecular level using the liquid jet approach and high resolution resonant inelastic X-ray scattering (RIXS).

For the first time, the liquid jet technology was installed at the RIXS endstation of BL07LSU. Beamline BL07LSU hast one of the few high resolution soft X-ray spectrometer, which has sufficient energy resolution to resolve vibrational modes. Coupled with the liquid jet method, it is an ideal tool to investigate biochemical systems. This method allows to probe liquid samples in vacuum environment and possible interaction of the liquid sample with membrane (as in liquid cell) are avoided. Furthermore, a higher flux is expected compared to the liquid cell method.
As shown in Figure 1, after 15 minutes a high energy resolution spectrum of liquid water on the oxygen K-edge can be recorded, which is 2-3 times faster compared to liquid cell.

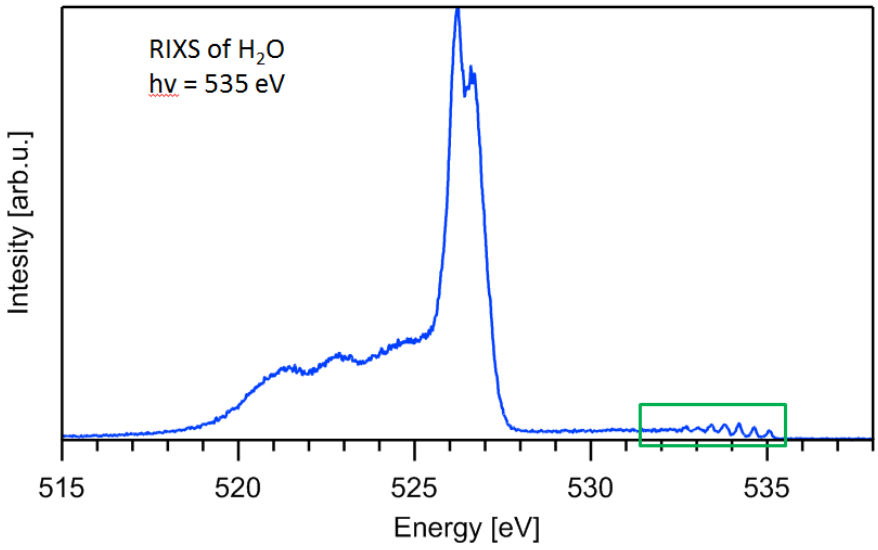

Fig 1. High resolution RIXS spectrum of liquid water using the liquid method. After 15 min a qualitative spectrum is recorded.

The experimental conditions were very nice, the synchrotron beam was stable and much data were recorded. Since it was the first time using the liquid jet, there is potential for improvement

for changing samples etc. Preliminary results show promising feature of ion induced changes on the spectrum of liquid water.
Figure 2 shows the impact of NaCl on the electronic and geometrical structure of liquid water (a) at different polarization.

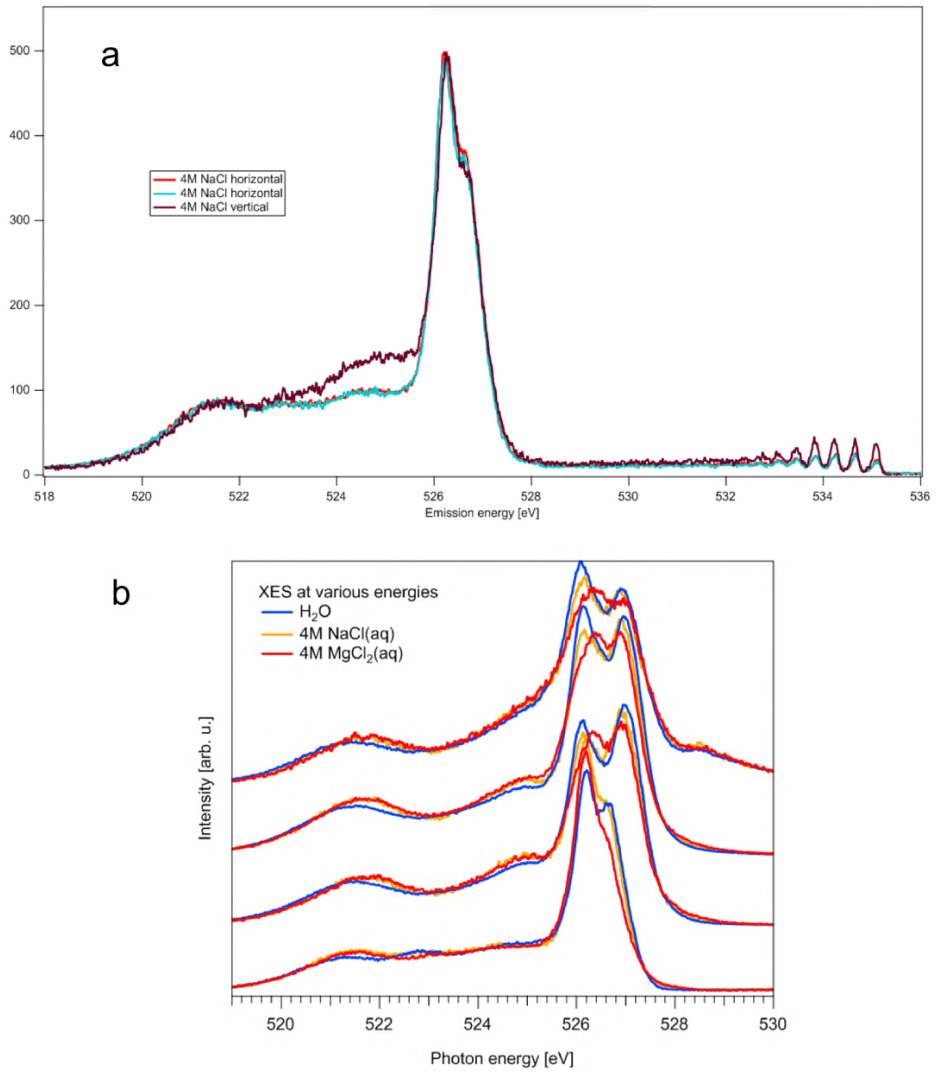

Fig 2. Fig 2a shows a polarization dependent spectrum of 4M NaCl. Figure 2b show ion specific impact on the electronic structure of liquid water.

And Fig 2b shows the oxygen K edge spectrum for several aqueous solutions. Ion specific influence can be observed. Overall, the experiment was a success in installing the liquid jet at the RIXS endstation and fulfill the vacuum conditions of the beamline. Ion specific changes on the electronic structure and the geometrical configuration can be observed in the spectra.
We plan to publish the static pioneering results with adequate theoretical calculations. Collaboration partners from the beamline will be included in possible publications.

Operando O *K*-edge soft X-ray emission spectroscopy studies of cathode materials for Li-ion battery

Daisuke Asakura[1], Takaaki Sudayama[1], Jun Miyawaki[2,3], Kosuke Yamazoe[2,3], Yoshihisa Harada[2,3], Hirofumi Matsuda[1], and Eiji Hosono[1]

[1]*Research Institute for Energy Conservation, National Institute of Advanced Industrial Science and Technology*

[2]*Institute for Solid State Physics, The University of Tokyo*

[3]*Synchrotron Radiation Research Organization, The University of Tokyo*

In order to improve the performances of electrode materials for Li-ion batteries (LIBs), electronic-structure analysis using synchrotron soft X-ray spectroscopy is of particular importance. For the cathode materials of LIBs such as $LiCoO_2$, 3*d* transition-metal (TM) $L_{2,3}$-edge X-ray absorption spectroscopy (XAS) has been used in order to reveal the redox reaction by charge-discharge process. Recently, the role of oxygen 2*p* orbital on the redox reaction has attracted attention particularly for the Li-excess layered oxide like $Li_{1.2}(Ni,Co,Mn)O_2$ which has a high capacity. Several O *K*-edge studies pointed out that the high capacity should be originated from redox reaction on isolated oxygen 2*p* orbitals [1].

On the other hand, we have focused on the orbital hybridization between the TM 3*d* and oxygen 2*p* orbitals for the cathode materials by using TM *L*-edge XAS and soft X-ray emission spectroscopy (XES) [2-4]. For $LiMn_2O_4$, we have found importance of the charge-transfer (CT) excitation for interpreting the Mn L_3 resonant XES (RXES) spectra by using our *operando* XES system [2]. The CT excitation connected with the Mn 3*d*-O 2*p* orbital hybridization in the Mn^{3+} and Mn^{4+} states largely changed during the redox reaction, which could affect the electrode performance. Nevertheless, *operando* O *K*-edge RXES measurement has not been performed because the electrolyte solution and thin-film current collector include lots of oxygen moieties which are obstructive for the O *K*-edge measurements of the cathode materials.

In this study, we developed an oxygen-free current collector and used an electrolyte solution including much less oxygen. $LiMn_{0.5}Fe_{0.5}PO_4$ (LMFP) thin-film layer was directly fabricated by sputtering on the oxygen-free current collector layer on Si_3N_4 window (150 nm) which separate the vacuum from the electrolyte solution (Fig. 1). LMFP is one of the cathode materials, in which the O 2*p* orbital is thought to be strongly hybridized with the Mn 3*d* orbital [5]. The *operando* O *K*-edge resonant XES measurements for LMFP were carried out at BL07LSU of SPring-8 [6].

Figure 2 shows the *operando* O *K*-edge RXES spectra for LMFP measured with three excitation energies (E_{ex} = 530.0, 531.4 and 533.0 eV) for the pre-edge region of O *K*-edge XAS. In the case of E_{ex} = 531.4 eV, the spectrum for the open-circuit voltage (OCV; before charge) is almost the same as that for the as prepared LMFP thin film and completely different from that for electrolyte. Thus, the information of the oxygen 2*p* orbital of LMFP is successfully observed in this *operando* setup. The structures for 520-527.5 eV in the emission energy

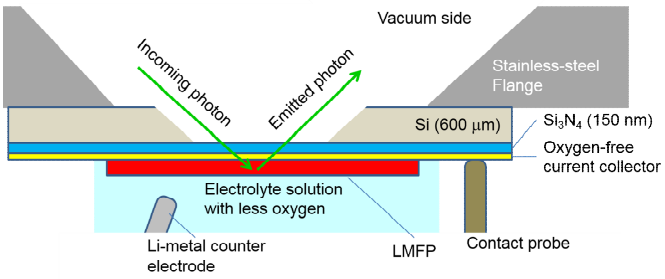

Fig. 1. Schematic image of the *operando* cell.

scale should be mostly attributed to the fluorescence and CT excitation of LMFP. With charging to 4.0 V in which the irons could be oxidized as $Fe^{2+} \rightarrow Fe^{3+}$, the intensity around 526 eV (indicated by black arrows in Fig. 2) is slightly enhanced. This energy region would be related to the Fe 3*d*-O 2*p* hybridization. Similar enhancement is also observed for E_{ex} = 531.4 eV.

In contrast, for E_{ex} = 533.0 eV, the signal from the electrolyte solution is significant in the cases of OCV and 4.0-V charge. Moreover, vibrational structures were observed near the elastic scattering (indicated by red arrow). The XES profiles for the OCV and 4.0-V charge are almost the same.

In summary, the *operando* cell with oxygen-free current collector and electrolyte solution with less oxygen was found to be useful for *operando* O *K*-edge RXES of LMFP for O *K*-edge XAS at pre-edge resonance. This system can be applied to O 2*p* electronic-structure analyses for other cathode materials. In the near future, *operando* O *K*-edge RXES of LMFP for a more charged state (~4.5 V, in which the manganese should be oxidized) and discharged state will be performed.

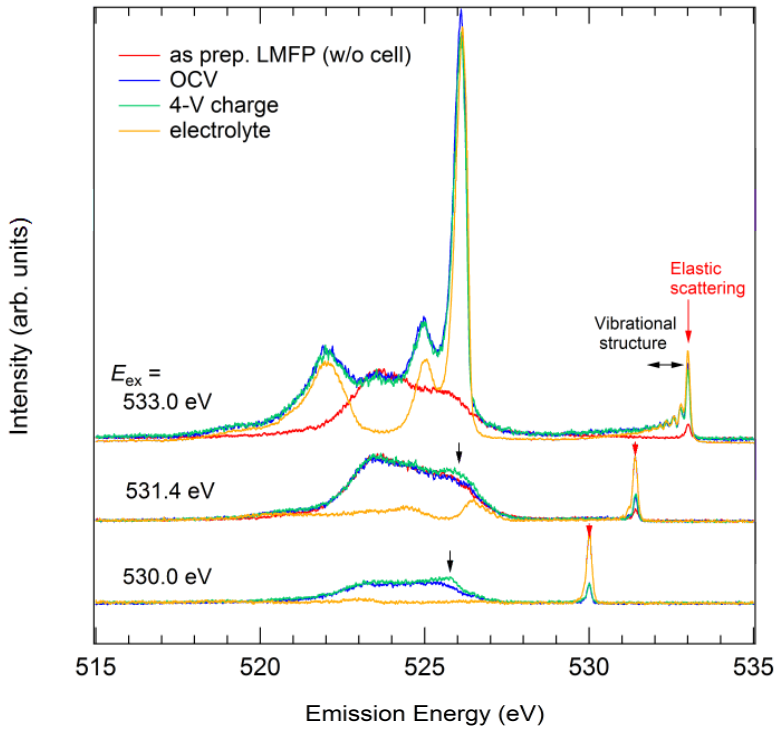

Fig. 2. *Operando* O *K*-edge RXES spectra of LMFP measured with three excitation energies. The spectra for as-prepared LMFP thin film are also shown.

Reference

[1] For example, W. E. Gent *et al.*, Nat. Commun. **8**, 2091 (2017).
[2] D. Asakura *et al.*, Electrochem. Commun. **50**, 93 (2015).
[3] D. Asakura *et al.*, Phys. Chem. Chem. Phys. **19**, 16507 (2017).
[4] D. Asakura *et al.*, ChemPhysChem **19**, 988 (2018).
[5] D. Asakura *et al.*, ChemPhysChem **17**, 4110 (2016).
[6] Y. Harada *et al.*, Rev. Sci. Instrum. **83**, 013116 (2012).

Interaction of H_2O with Li in Hydrate Melt Electrolytes Studied by O *K*-edge X-ray Emission

Y.-T. Cui[1], J. Miyawaki[1], K. Yamazoe[1], Y. Kosegawa[1], K. Akada[1], T. Shimada[2], M. Okubo[2] and Y. Harada[1]

[1]*Synchrotron Radiation Laboratory, Institute for Solid State Physics, The University of Tokyo*
[2]*Department of Chemical System Engineering, The University of Tokyo*

Aqueous Li-ion batteries have attracted great attention as a battery technology [1, 2, 3] owing to its low production cost, non-flammable, low-toxic aqueous electrolytes. However, narrow potential window (1.23 V for pure water) and lack of suitable negative electrodes limit their applications as a higher energy-density battery with reported fabrication method. Recently, Yamada *et al.* reported Li salt hydrate melt (LSHM) working as an electrolyte at room-temperature for high energy-density batteries (80 - 300 Wh/kg), which bridges the traditional energy-density gap between aqueous (< 100 Wh/kg) and non-aqueous (> 150 Wh/kg) Li-ion batteries [4]. In order to understand the working mechanism of LSHM and to find new type aqueous electrolytes, investigation of LSHM structures and interaction of Li and H_2O as well as careful selection of Li salt anions are all important.

In this work, the electronic structure of LSHM were investigated by O *K*-edge X-ray absorption/emission spectroscopy (XAS/XES) which have high sensitivity to interaction of H_2O molecules with their local environments [5, 6] and thus can detect Li-H_2O, Li-anion, H_2O-anion interactions. The O *K*-edge XAS/XES experiments were carried out at HORNET end-station at BL07LSU of SPring-8 (shown in Fig. 1 (a)) using a liquid flow-through cell (Fig. 1 (b)). A 100 nm SiC membrane coated with 3 nm Cr and 11nm Au (Fig. 1 (c)) was used to isolate vacuum from atmosphere or liquid samples as described in the schematic drawing of the liquid flow-through cell in Fig. 1 (d). a hydrate melt sample ($(Li(TFSI)_{0.7}(BETI)_{0.3}\cdot 2H_2O$, where TFSI = $N(SO_2CF_3)_2^-$ and BETI = $N(SO_2CF_5)_2^-$) [4] was flowed by a tubing pump during the measurement. Defocusing mode and sample scanning mode were used for XAS and XES, respectively, to avoid beam damage to the sample and membrane. Reference Li salt powders (TFSI, BETI) were also measured by fixing them on a copper plate using a carbon tape. Non-resonant 550 eV excitation was used for XES.

O *K*-edge XAS/XES spectra of the hydrate melt and the reference TFSI, BETI powders as well as liquid water are presented in Fig. 2. The hydrate melt has different XAS/XES profile from TFSI and BETI powders, possibly due to contribution of oxygen atoms from H_2O interacting with Li and/or TFSI/BETI in the hydrate melt. To understand the detailed interactions, H_2O contribution to the XAS/XES spectrum was extracted by considering the molar ratio for each oxygen component in the hydrate melt. The generated XES spectrum of H_2O in the hydrate melt denoted as Generated at the bottom of Fig. 2 shows clear 3-main-peak structures ($1b_1$, $3a_1$, $1b_2$) like gas phase H_2O but having slightly different peak energy, which implies a well isolated H_2O molecule but bonded to Li and/or TFSI/BETI, consistent with the reported Raman spectra [4]. The Generated spectrum has additional shoulder structure at 523 eV and a small peak around 518 eV, which will indicate the presence of more complex H_2O configurations interacting with surrounding Li and/or TFSI/BETI. For XAS the profile of the Generated spectrum is completely different from that of gas phase H_2O but rather closer to the liquid phase. This is not unexpected since the unoccupied states are

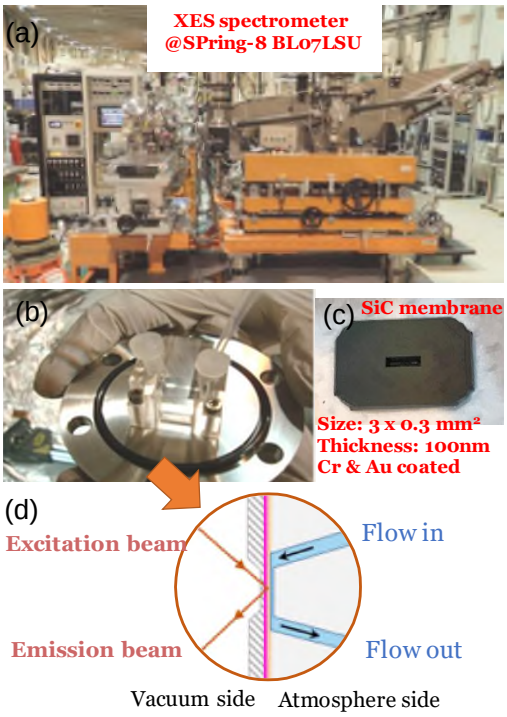

Fig.1 (a) XES spectrometer of BL07LSU at SPring-8, (b) liquid flow-through cell, (c) 150nm thick SiC membrane, and (d) sectional view of the liquid flow-through cell.

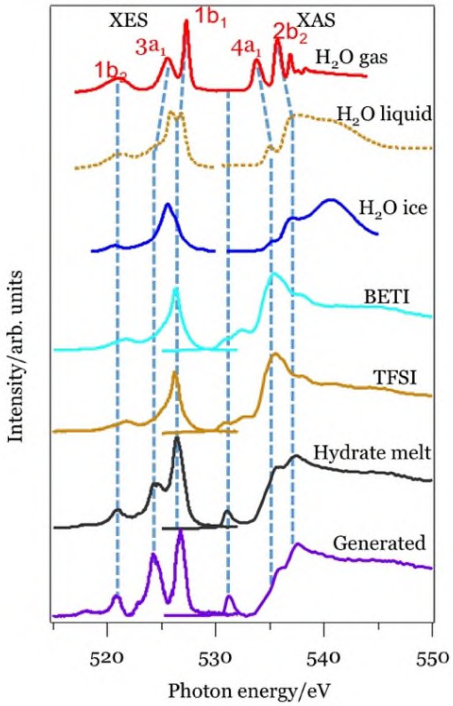

Fig.2 O ***K***-edge XAS and XES spectra of hydrate melt, TFSI, BETI powder, as well as H_2O gas, liquid and ice phases. Contribution from H_2O was made as Generated one.

extended in space and more sensitive to the interaction with surrounding molecules. The two structures around 536 eV and 538 eV can be assigned to $2b_2$- and $4a_1$-like states, respectively, considering an isolated H_2O molecule bonded to Li and/or TFSI/BETI. The peak around 531 eV is still unknown because it cannot be found in the gas phase H_2O and also much different to that of TFSI/BETI. At present, we simply consider it is most likely coming from O_2 gas, which could be introduced during measurement by the tubing pump system in atmosphere.

In conclusion, electronic structure of Li salt hydrate melt was successfully obtained by O *K*-edge XAS/XES. It is found that H_2O molecules confined in the hydrate melt are most likely isolated with each other and bonded to Li and/or TFSI/BETI. By combining the experimental result with theoretical simulations, we will obtain detailed information about H_2O configuration and fully understand the function of water in the hydrate melt to process high performance in Li ion batteries .

Acknowledgements: The XAS/XES experiments were carried out by the joint research in the Synchrotron Radiation Research Organization and the Institute for Solid State Physics, the University of Tokyo and with the approval of Japan Synchrotron Radiation Research Institute (Proposal Nos. 2017A7538, 2017B7548).

REFERENCES

[1] L. Suo *et al.*, Science **350**, 938 (2015).
[2] J.-Y. Luo *et al.*, Nat. Chem. **2**, 760 (2010).
[3] H. Kim *et al.*, Chem. Rev. **114**, 11788 (2014).
[4] Y. Yamada *et al.*, Nat. Energy **1**, 16129 (2016).
[5] K. Yamazoe *et al.*, Langmuir **33**, 3954 (2017).
[6] T. Tokushima *et al.*, Phys.Chem.Chem.Phys. **16**, 10753 (2014).

THREE-DIMENSIONAL ATOMIC ARRANGEMENT AROUND ACTIVE/INACTIVE DOPANT SITE IN BORON-DOPED DIAMOND

Yukako Kato[1], Daichi Tsujikawa[2], Yusuke Hashimoto[2], Taisuke Yoshida[2], Shun Fukami[2], Hiroyuki Matsuda[2], Munetaka Taguchi[2], Tomohiro Matsushita[3] and Hiroshi Daimon[2]

[1]Advanced Industrial Science and Technology (AIST), Tsukuba, Ibaraki 305-8568, Japan;
[2]Nara Institute of Science and Technology (NAIST), Ikoma, Nara 630-0192, Japan;
[3]Japan Synchrotron Radiation Research Institute (JASRI), Sayo, Hyogo 679-5198, Japan

Boron-doped diamond has received significant attention as an advanced material for power devices, owing to its high breakdown characteristics. For the control of diamond characteristics related to band conduction, it is essential to determine the atomic structure around dopant, and to develop the control method of the atomic arrangement around dopant. When the boron concentration is high, there is a possibility that the doped boron site in diamond is not only substitutional but also interstitial. If boron is located at these interstitial sites, it is considered that boron does not act as an acceptor of band conduction. Therefore, the study of dopant site in heavily boron-doped diamond is an important topic not only for fundamental research but also for device application to develop a method of resistivity control for p-type conductive diamond. However, it is difficult to measure the atomic structure around the dopant because the x-ray diffraction cannot measure the aperiodic structure such as the dopant in the crystal.

In this study[1], we used a newly developed display-type ellipsoidal mesh analyser (DELMA)[2,3] that can detect a two-dimensional angular distribution of photoelectron with ± 50 degrees with higher energy resolution. This is for the visualizing local atomic structures around a photoelectron emitter atom[4,5]. By using this measurement system, we elucidated the dopant site of boron in heavily boron-doped diamond by using XPD patterns through the analysis of emission angle dependence of the B 1*s* core-level-shifted peaks in the x-ray photoelectron spectra (XPS). The sample is an epitaxial boron-doped diamond, which was grown by a plasma-assisted CVD method. The epitaxial layer thickness was approximately 1 μm. A boron atomic concentration estimated from SIMS was 2×10^{20} / cm^3. The resistivity was 1.5×10^{-2} Ω·cm at 300 K. The as-grown sample was cleaned in a 3:1 mixture of sulphuric and nitric acid, and was hydrogen-terminated by microwave plasma with H_2 gas to form stable H-terminated surfaces for the surface-sensitive XPS measurement. XPD measurements were performed in a vacuum of 8×10^{-8} Pa at soft-x-ray beamline BL07LSU of SPring-8 using DELMA, which enables acquisition of a two-dimensional angular distribution snapshot of specific kinetic energy electrons. Photoelectron diffraction calculations were performed by using the Total-analysis Multiple Scattering Pattern (TMSP) program package[6].

First, we start with peak assignment of the left side in Fig. 1(a), which is the observed photoelectron intensity angler distribution (PIAD) pattern of C 1*s* core-level. The PIAD pattern is compared with the scattering simulation pattern shown in the right side of Fig. 1(a). The kinetic energy E_{kin} of the photoelectron was set to 600 eV. PIAD of C 1*s* in Fig. 1(a) shows clear four-fold symmetric pattern and exhibits good agreement with the calculation, suggesting that the heavily boron-doped diamond has grown homoepitaxially on the substrate diamond (001). This result is in good agreement with the previous report[7]. Since the lattice constant increases in proportion to the boron concentration in boron-doped diamond, the lattice is strained when the growth direction is (001). Thus, the average interatomic distances increase without changing the crystal symmetry. Figure 1(b) is a projection pattern of atomic distribution around the emitter atom. Since the diamond has two inequivalent sites in the unit cell, observed XPD pattern is a superimposed pattern from two kinds of emitter atoms, called emitter 1 and 2

in this paper. The directions of each scattererers around emitter 1 are indicated in Fig. 1(b) and Fig. 2(a) by corresponding colours. The hemispherical atomic cluster model for the XPD pattern simulation is also shown in the inset of Fig. 1(b) where the emitter was set at the centre of the bottom atomic layer. The radius of the hemisphere is 2*a*, where *a* is the lattice constant of diamond, 3.567 Å. Next, we look into the emission-angle dependence of the B 1*s* photoelectron spectra. Figure 2(b) shows the photoelectron spectra of the B 1*s* core level along the [001], [101], and [111] directions. Surprisingly, two B 1*s* peaks at 189.5 eV (peak A) and 187.5 eV (peak B) are observed at all emission angles, indicating the presence of two types of boron sites. Furthermore, a comparison of the core-level spectra for different emission directions clearly shows that the spectral weight in the low-binding-energy peak, peak B, decreases significantly in the [001] direction when we normalize the spectra at peak A. The intensity ratios of peaks A and B in the three directions, $B/A_{[001]}$, $B/A_{[101]}$, and $B/A_{[111]}$, are 0.7, 1.0, and 1.1, respectively. In order to discuss the origin of the observed two peaks, we calculated XPD patterns with two different models (*i*.e. the interstitial, site-X in Fig.2(a), and the substitutional doping model)[1]. We therefore can firmly conclude that peak A is caused by the boron at an interstitial dopant site and the peak B is from a substitutional boron dopant site. This is consistent with the idea that the binding energy of interstitial boron (the valency number is 0) should be higher than that of substitutional boron (the valency number is -1). This shows that the substitutional sited boron is an active “dopant” as an acceptor because it is negatively charged and produces holes. On the other hand, the interstitial boron is “an inactive impurity” for band conductance without producing carrier, but should be in charge of hopping conductance when the concentration becomes high enough to cause hopping conductance.

This work was supported by JSPS Grant-in-Aid for Scientific Research on Innovative Areas "3D Active-Site Science": Grant Number 15H01056 and 17H05226.

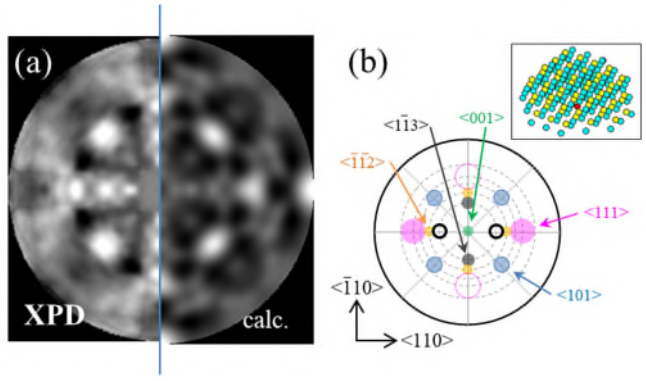

Fig. 1

(a) Left side: Observed XPD pattern of C 1*s* from heavily boron-doped diamond (001) at E_{kin} = 600 eV. This pattern has been drowned in orthographic projection method. Right side: Simulated XPD pattern of diamond (001) at E_{kin} = 600 eV. The projection method is the same as left-side figure.

(b) Arrangement of bright spots in (a). Filled circle and open circles mean bright spots of photoelectrons from the emitter 1 at (0, 0, 0) and the emitter 2 at (*a*/4, *a*/4, *a*/4), respectively, where *a* is the lattice constant, 3.567 Å. Inset of (b) is an atomic cluster of diamond (001) for the pattern calculation.

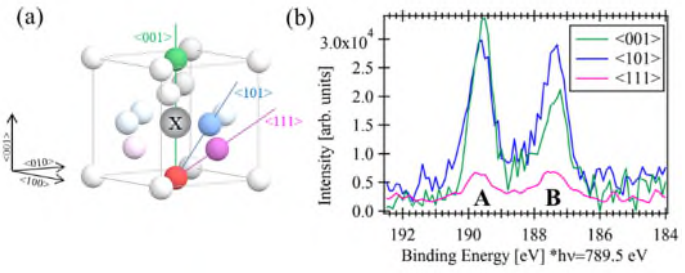

Fig. 2

(a) Emission directions of photoelectrons. The colours of atoms are the same as those in Fig. 1(b) and 2(b).

(b) Photoelectron spectra of B 1*s*. Two peaks are observed in all spectra: one peak at high binding energy, named “peak A”, and another peak at low binding energy, named “peak B”.

REFERENCES

[1] Y. Kato *et al.*, *APEX* **11**, 6 (2018), [2] H. Daimon *et al.*, *Surf Sci* **601**, 20 (2007), [3] K. Goto *et al.*, *eJSSNT* **9** (2011)., [4] T. Matsushita *et al.*, *J Phys Soc Jpn* **82**, 11 (2013)., [5] H. Daimon *et al.*, *e-JSSNT* **10** (2012)., [6] T. Matsushita *et al.*, *Electron Spectrosc Relat Phenom* **178–179**, 195-220 (2010)., [7] A. Kawano *et al.*, *Phys Rev B* **82**, 8 (2010).

PHOTOELECTRON DIFFRACTION STUDY OF CDW ON 1T-TAS_2

Xin Tan[1], Munetaka Taguchi[1], Yusuke Hashimoto[1], Hiroki Momono[1], Shun Fukami[1], Yudai Higa[1], Masafumi Ogi[1], Shinta Kobayashi[1], Dawei Peng[1], Hiroyuki Matsuda[1], Hitoshi Osawa[3], Tomohiro Matsushita[3], Hiroshi Daimon[1]

[1]*Graduate School of Materials Science, Nara Institute of Science and Technology*

[2]*Japan Synchrotron Radiation Research Institute*

The primary goal of our study was to investigate the dynamics of the recovery of charge density wave (CDW) order of 1T-TaS_2, after a rapid CDW melting, using X-ray photoelectron diffraction (XPD). The core level splittings observed in 1T-TaS_2 in its commensurate CDW phase correspond to different sites in the $\sqrt{13} \times \sqrt{13}$ "Star of David" structure. In our experiment at BL07LSU during the semester of 2017A, we seeked to exploit the CDW core level splittings of Ta 4f in 1T-TaS_2 as a case-of-study or benchmark for future high energy resolution site specific XPD. This study, in turns, established the future of time-resolved X-ray photoelectron diffraction (TRXPD) as a method to probe the dynamics of site-specific structural informations in soft X-ray energy regime. The availability of the soft X-ray beam chopper and the limited beamtime allotted were the main challenges to this study. And also, due to the limitation of the beamtime period, the other two samples in the proposal, $TbTe_3$ and 1T-$TiSe_2$ were not investigated.

For the study on 1T-TaS_2, 2D-PES measurements with an acceptance angle of 50°were performed at the free port of BL07LSU in SPring-8. The Display-type Ellipsoidal Mesh Analyser (DELMA) [1-6] combined with an energy analyser (VG SCIENTA R4000) was used to obtain 2D-PIAD patterns. The electrons we're swept across the entrance slit of R4000 in slices by employing a deflector. The post energy-filtered images in slices were reconstructed to obtain the high energy resolution XPD. Due to the photoelectron count owing to the high cross-section of the Ta 4f at the selected photon energy ($h\nu$ = 625 eV), the entrance slit was set to the highest energy resolution at 0.1mm.

The calculated XPD of intrinsic 1T-TaS_2 using EDAC code was directly compared to the experimental data obtained using DELMA and showed good agreement on the 1T structure. The sample was then oriented to position the nearest, strongest forward-focusing peak (Ta-Ta) in the center of the image. The R4000 deflector scans were done in approximately 28 slices by varying the potential of the deflectors in constant intervals, with each slice showing intrinsic angular resolution as shown in Figure 1.

Due to an unexpected technical difficulty with the electron deflector, the angular range scanned in the high energy resolution data was limited. The time taken for a single slice (angle-resolved spectrum) was a few minutes, and in about an hour and half's time XPD images spanning from 594eV to 602eV kinetic energy in 200meV step intervals was obtained. Figure 1, at similar color scaling, shows some differences in fine features between the XPDs of the two core-level sites.

From this study, we demonstrated the viability of using DELMA together with a high resolution energy filter, to perform XPD at an unprecedented angular range at such energy resolution. For a future time-resolved study, the entrance slit of the hemispherical analyzer could be set to lower energy resolution to offset the low photoelectron count. At 10 kHz beam chopping frequency of H-mode single bunches, we are expecting a drop in total photoelectron of two to three orders of magnitude. By setting a wider slit and only scanning the particular kinetic energies of interest, TRXPD could be realized. On the other hand, at a temperature of below 50 K, the CDW splittings of Ta 4f core levels are larger than 500 meV with significantly narrower peaks, permitting lower energy resolution settings (pass energy and slit size). In our

present experiment, sample temperature of about 110 K was achieved, improvements will have to be made to the sample stage for more conclusive results.

In consideration of future TRXPD experiments, a longer allotted time for instrument connection to the free port of BL07LSU is recommended. In this way, tests could be done for optimizations of the electron optics and the sample and chamber preparations. The length of the beamtime granted for this study was too limited for proper study of a new technique. A longer beamtime would not only be more productive but also enables proper optimizations to be done.

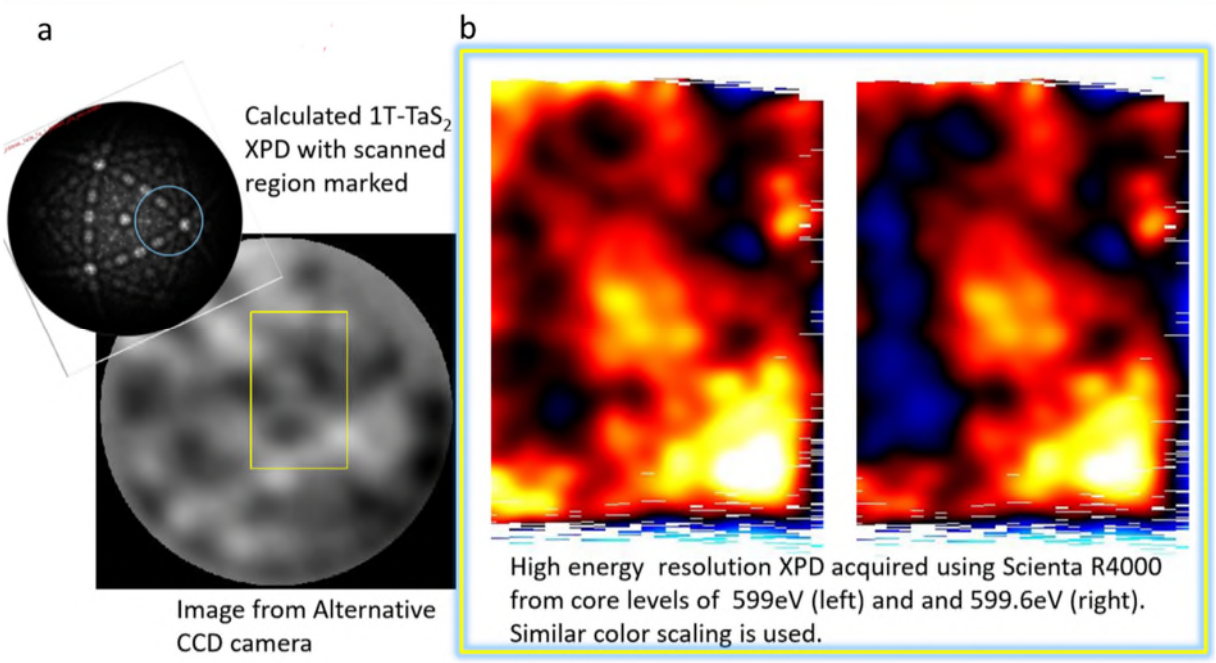

Fig. 1 (a) The experimental data obtained using DELMA without high resolution energy filtering, which is compared to the calculated 1T-TaS_2 (inset). It is noteworthy that the image was obtained within 15 seconds with good signal-to-noise ratio. (b) The stitched slices of the high energy resolution data obtained on the CCD of R4000 using the electron deflector of DELMA in front of the entrance slit of R4000. The region swept was highlighted by a rectangular box in (a).

REFERENCES

[1] L. Tóth, H. Matsuda, T. Shimizu, F. Matsui, and H. Daimon, J. Vac. Soc. Jpn. **51**, 135-137 (2008).

[2] K. Goto, H. Matsuda, M. Hashimoto, H. Nojiri, C. Sakai, F. Matsui , H. Daimon, L. Tóth, T. Matsushita, e-J. Surf. Sci. Nanotech. **9**, 311-314 (2011).

[3] L. Tóth, K. Goto, H. Matsuda, F. Matsui, H. Daimon, Nucl. Inst. Meth. Phys. Research Sec. A 648, S58-S59 (2011).

[4] L. Tóth, H. Matsuda, F. Matsui, K. Goto, H. Daimon, Nucl. Inst. Meth. Phys. Research Sec. A **661**, 98-105 (2012).

[5] Hiroyuki Matsuda, László Tóth, Fumihiko Matsuia, Hiroshi Daimon, Journal of Electron Spectroscopy and Related Phenomena 195, 78–84, (2014)

[6] H. Matsuda K. Goto L. Tóth M. Morita S. Kitagawa, F. Matsui M. Hashimoto C. Sakai T. Matsushita H. Daimon, Journal of Electron Spectroscopy and Related Phenomena 195, 382-398, (2014)

REAL-TIME OBSERVATION OF CARRIER DYNAMICS IN PLASMON RESONANT EXCITATION OF AU/TIO2

SusumuYamamoto[1], Kenichi Ozawa[2], Naoya Terashima[3], Yuto Natsui[3], Marie D'Angelo[4], Hiroo Kato[5], Iwao Matsuda[1]

[1] *The Institute for Solid State Physics, The University of Tokyo*

[2] *Department of Chemistry, Tokyo Institute of Technology*

[3] *Department of Advanced Physics, Hirosaki University*

[4] *Institut des Nanosciences de Paris, Université Pierre et Marie Curie-Paris 6*

Introduction

Localized surface plasmon resonance (LSPR) is an optical phenomena generated by light when it interacts with metal nanostructures. Chemical reactions utilizing the enhanced electric fields of LSPR are called “Plasmonic chemistry”, and attract great interest because they can improve catalytic activities and realize chemical reactions that were not possible with conventional thermal excitation. However, the experimental studies on the dynamics of photo-excited carriers generated in the relaxation process of plasmon resonant excitation have been quite limited.

X-ray photoelectron spectroscopy (XPS) has been quite successful in providing direct access to electronic structures of materials with element specificity and surface sensitivity. For example, the change in surface potentials at semiconductor surfaces due to photo-excited carriers, called as surface photovoltage (SPV) effect, can be monitored as an energy shift of XPS spectra. The extension of XPS to time-domain, or time-resolved XPS (tr-XPS), thus allows one to study the dynamics of photo-excited carriers at semiconductor surfaces.

In this study, we studied the dynamics of photo-excited carriers generated by plasmon resonant excitation of gold nanoparticles on titanium oxide (Au/TiO_2), which is a representative plasmonic nanomaterial, using tr-XPS.

Experimental

The Au/TiO_2 sample was prepared by dropping a solution containing Au nanoparticles (Cytodiagnostics Inc., 40 nm in diameter) onto the $TiO_2(110)$ surface in the air, which was cleaned in vacuum by sputtering and annealing in O_2.

The tr-XPS experiments were carried out at SPring-8 BL07LSU [1] by a laser-pump and synchrotron-radiation (SR)-probe method [2]. The pump laser had an energy of 2.3 eV, pulse duration of 60 fs, and a repetition rate of 208 kHz. The probe SR had an energy of 735 eV, pulse duration of 50 ps. Note that the wavelength of pump laser was tuned to the resonant wavelength of plasmons for 40 nm Au nanoparticles (532 nm, 2.3 eV) using an optical parametric amplifier. Since the band gap of rutile TiO_2 (3.0 eV) was larger than the energy of incident laser (2.3 eV), only the Au nanoparticles were selectively excited by pump laser. The carrier injection of photo-excited carriers from Au nanoparticles to TiO_2 substrate was monitored in real time by energy shift of Ti 2*p* core-level spectra. All the experiments were performed at 300 K.

Results and discussion

First, the static electronic structure of the Au/TiO_2 sample was evaluated by valence band and core-level XPS spectra. The valence band spectrum shows that Au/TiO_2 has an accumulation space charge layer with the downward band bending of 0.28 eV. No energy shift of Ti 2*p* core-level peak before and after Au deposition indicates the absence of charge transfer between Au nanoparticles and TiO_2 substrate. The presence of Au nanoparticles is confirmed by Au 4*f* core-level spectra.

Figure 1 shows Ti $2p_{3/2}$ XPS peak positions for (a) $Au/TiO_2(110)$ and (b) clean $TiO_2(110)$ with and without plasmon resonant excitation. On $Au/TiO_2(110)$, Ti $2p_{3/2}$ XPS peak shifts to higher binding energies by about 12 meV. In contrary, no peak shift is observed on the clean $TiO_2(110)$ surface. Note that the reproducibility of Ti $2p_{3/2}$ XPS peak positions was confirmed by repeating the measurements of laser ON/OFF spectra. This result clearly shows that the energy shift of Ti $2p_{3/2}$ XPS peak originates from the carrier injection from plasmon-excited Au nanoparticles to the TiO_2 substrate. In addition, the delay time dependence of Ti $2p_{3/2}$ XPS peak shows that the lifetime of injected photo-excited carriers is as short as 500 ps.

Furthermore, we have been developing the time-resolved ambient-pressure XPS system with the aims to monitor plasmonic chemical reactions and carrier dynamics simultaneously in the presence of near-ambient pressure gas. We succeeded in measuring the SPV effect on Si(111) in CO_2 gas with continuous laser excitation.

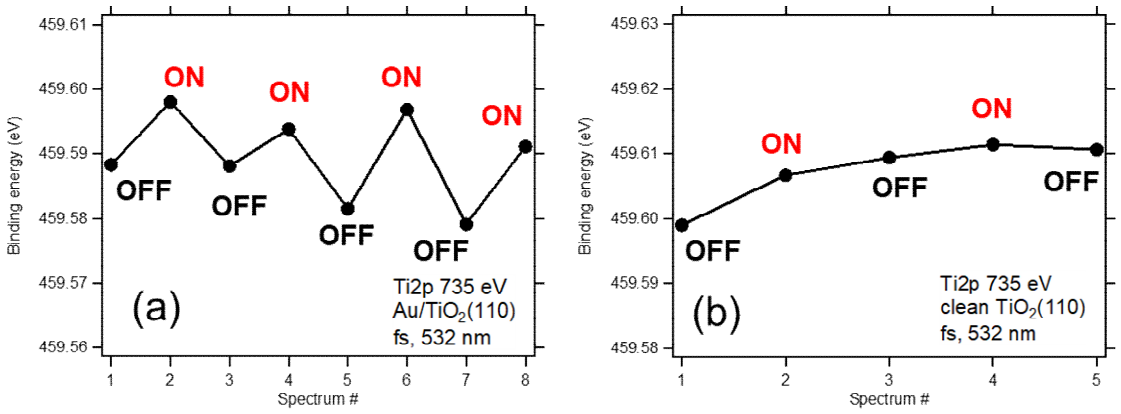

Figure 1 Ti $2p_{3/2}$ XPS peak positions for (a) $Au/TiO_2(110)$ and (b) clean $TiO_2(110)$ with Laser ON and OFF. Pump-laser: 532 nm, 60 fs, 41.3 μJ/cm^2, delay time 0.1 ns. Probe-SR: 735 eV, 50 ps.

Acknowledgement

This work was carried out by the joint research in the Synchrotron Radiation Research Organization and the Institute for Solid State Physics, the University of Tokyo (Proposal No. 2017A7532 and 2017B7549).

REFERENCES

[1] S. Yamamoto *et al.*, J. Synchrotron Rad. **21**, 352-365 (2014).
[2] S. Yamamoto, I. Matsuda, J. Phys. Soc. Jpn. **82**, 021003 (2013).

VALENCE ELECTRONIC STRUCTURE OF IRON PORPHYRIN COMPLEXES INVESTIGATED BY RIXS SPECTROSCOPY

Benjamin Van Kuiken
Serena DeBeer
Anselm Hahn
Department of Inorganic Spectroscopy, Max Planck Institute for Chemical Energy Conversion
Yoshihisa Harada
Jun Miyawaki
Institute for Solid State Physics, University of Tokyo

The increasing use of fossil fuels for energy has led to a dramatic increase in the atmospheric concentration of CO_2, which is major contributor to global warming. It would be ideal to find ways to utilize the CO_2 by reducing it to usable fuels like methanol. However, CO_2 possesses a large reduction potential of ~1.9 V vs. SHE requiring the use of catalysts to affect the chemical transformation. Some of the most efficient CO_2 reduction catalysts have been based on iron tetraphenylporphyrin (FeTPP) complexes.[1] In its super-reduced state, $[Fe(TPP)]^{2-}$, this complex acts as a highly efficient catalyst for CO_2 reduction. Nominally, $[Fe(TPP)]^{2-}$ possesses an Fe(0) oxidation state. However, recent studies have suggested that it actually contains Fe(II) and a reduced porphyrin ring (TPP^{2-}).[2] A better understanding of the electronic structure of the various oxidation states of Fe(TPP) would provide useful insight in to the mechanism of CO_2 reduction, but typical optical spectroscopy is dominated by porphyrin ring-based excitations. Consequently, selective spectroscopic probes of the metal are required, and we have utilized resonant inelastic X-ray scattering (RIXS) at the Fe L-edge to probe the valence electronic structure of a series of Fe(TPP) complexes.

RIXS spectroscopy is a powerful element-selective spectroscopic technique that probes the valence excitations in material systems. 2*p*3*d* RIXS spectra are collected when a sample is excited by soft X-rays at the Fe L-edge (~706 eV) and the X-ray emission resulting from $3d \rightarrow 2p$ is monitored. The energy differences between incident and emitted X-rays corresponds to energies of valence excitations including *d-d* transitions. In order to resolve how the electronic structure of the Fe atom, the CO_2 binding site, in this porphyrin is affected by changes in oxidation state the 2p3d RIXS spectra of a series of Fe(TPP) complexes were measured. The complexes include Fe(TPP)Cl, Fe(TPP), $Fe(TPP)(THF)_2$, $[Fe(TPP)]^-$, and $[Fe(TPP)]^{2-}$, which span four formal oxidation states of the Fe atom. The degree to which the Fe electronic structure is perturbed by redox events is encoded in the *d-d* spectrum of the complexes. The RIXS spectrum of each of the complexes was measured at BL07LSU at SPring-8.

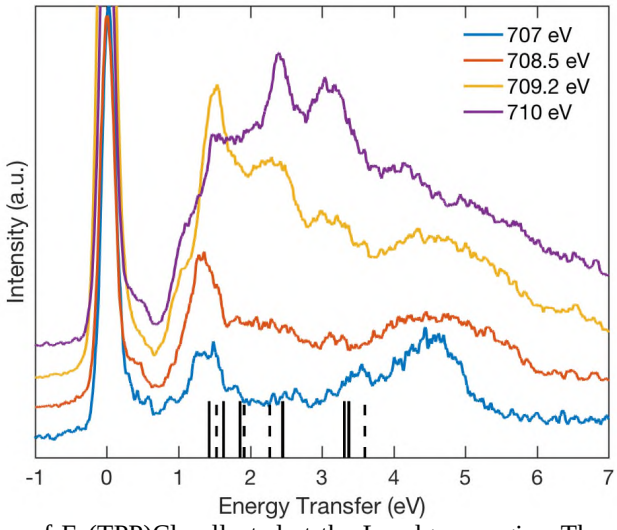

Figure 1. 2*p*3*d* RIXS spectra of Fe(TPP)Cl collected at the L_3-edge energies. The vertical sticks are transition energies computed with the CASSCF/NEVPT2 method for quartet (solid lines) and sextet (dashed lines) states.

Figure 1 shows the RIXS spectra of Fe(TPP)Cl collected at four energies across the L_3-edge. The spectra are characterized by several bands of inelastic features between ~1 and 6 eV. Features appear at ~0.4, ~1.0-1.5, ~2.4, ~3.1, and ~4.5 eV and they appear at approximately constant energy suggesting that they are *d-d* excitations. Fe(TPP)Cl possesses a $^6A_1$ ground state, so only spin-forbidden metal-centered transitions are possible suggesting that the *d-d* excitations are to quartet states as previously observed iron chlorides.[3] To gain further insight regarding the nature of the excited state, quantum chemical calculations were carried out at the CASSCF/NEVPT2 level of theory, and the excitation energies are shown for quartet (solid) and sextet (dashed). The sextet states from the calculated spectra are ring-based excitations are not expected to contribute significant intensity to the RIXS, but the quartet states (solid) lines are in good agreement with features observed in the experimental spectra. The most peculiar feature in the spectrum is the 0.4 eV feature, which is not predicted by the calculations. It is therefore possible that this feature is due to other effects such as vibrational excitation.

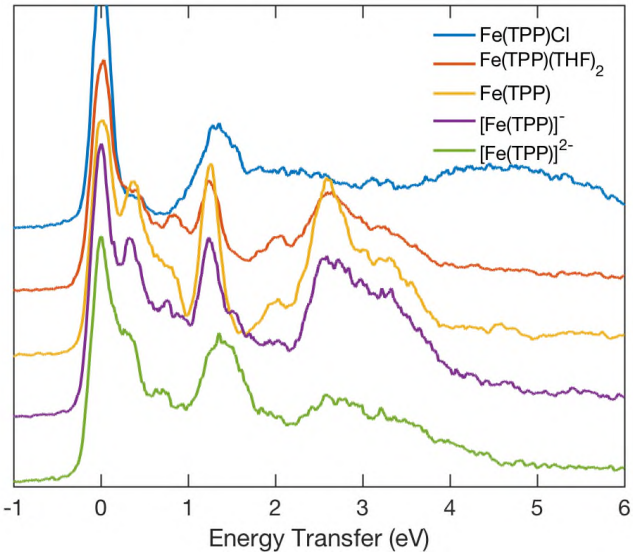

Figure 2. RIXS spectra of Fe(TPP) complexes excited at their L_3-edges.

Figure 2 shows the spectra of each of the iron porphyrin complexes excited at ~708.5 eV. Inspection of the spectra shows that there are some significant differences between the Fe(III) complex Fe(TPP)Cl and the remaining molecules. The spectrum of each complex contains features near contain features at or near 0.35, 0.7, 1.2, 2.0, 2.5 and 3.3 eV. It is the two intense low-energy features that distinguish these Fe(TPP) complexes from the Fe(III) sample. The presence of RIXS below 1 eV has previously been shown to be characteristic of the presence of Fe(II).[3] Thus, the spectra of the Fe(II) reference compounds Fe(TPP) and Fe(TPP)$(THF)_2$ are in good agreement with previously reported RIXS spectra. Moreover, the similarity between the RIXS spectra of $[Fe(TPP)]^-$ and $[Fe(TPP)]^{2-}$ provides additional evidence that the Fe atoms in these complexes are in the +2 oxidation state in agreement with recent XAS measurements.[2]

In summary, RIXS spectroscopy has been used to investigate the electronic structure of iron porphyrin complexes. It is shown that there are clear differences in the RIXS spectra when the Fe center is reduced from Fe(III) to Fe(II), and the spectra are consistent with the suggestion that the porphyrin ring is redox active in the anionic species. Ongoing theoretical studies are focused on extracting further insight from these spectra.

REFERENCES

[1] Costentin, C.; Robert, M.; Savéant, J.-M. *Chem. Soc. Rev.*, **2013**, 42, 2423-2436.
[2] Römelt, C.; Song, J.; Tarrago, M.; Rees, J. A.; van Gastel, M.; Weyhermüller, T.; DeBeer, S.; Bill, E.; Neese, F.; Ye, S. *Inorg. Chem.*, **2017**, 56, 4745-4750.
[3] Hahn, A. W.; Van Kuiken, B. E.; *et al.*, *Inorg. Chem.*, **2017**, 56, 8203-8211.

SPATIO-TEMPORAL DYNAMICS OF ELECTRONIC STATES OF SURFACES OF GAN-HEMT RELATED WITH CURRENT COLLAPSE PHENOMENA

Hirokazu Fukidome
Research Institute of Electrical Communication, Tohoku University

GaN-based transistors using the two-dimensional gas (GaN-HEMT) as a channel is promising for the next-generation wireless communication, owing to high-power and high-frequency capabilities, arising from large bandgap and saturation velocity larger than Si and GaAs. In fact, GaN-HEMT has been already commercialized, and becomes one of the key device. Currently, GaN-HEMT is going to be applied for the higher frequency, millimeterwave frequency. However, for millimeterwave frequency applications, current collapse phenomena, which are related with surface states charging/discharging, should be solved for highly reliable operation.

The current collapse phenomena is suitable for soft x-ray experiments, in terms of basic research and academia-industrial alliance. In fact, 3D nano-ESCA, which enables to nanoscopically investigate surface electronic states [1-3], quantitatively visualized surface states charging related with the current collapse phenomena [4].

The point to be noted is that surface states charging is dynamical phenomena. This indicates that time-resolved experiments, in addition to spatially-resolved experiments, are need for deeper understanding of the current collapse phenomena.

We performed time-resolved photoelectron experiments. A typical result is shown in Fig. 1.

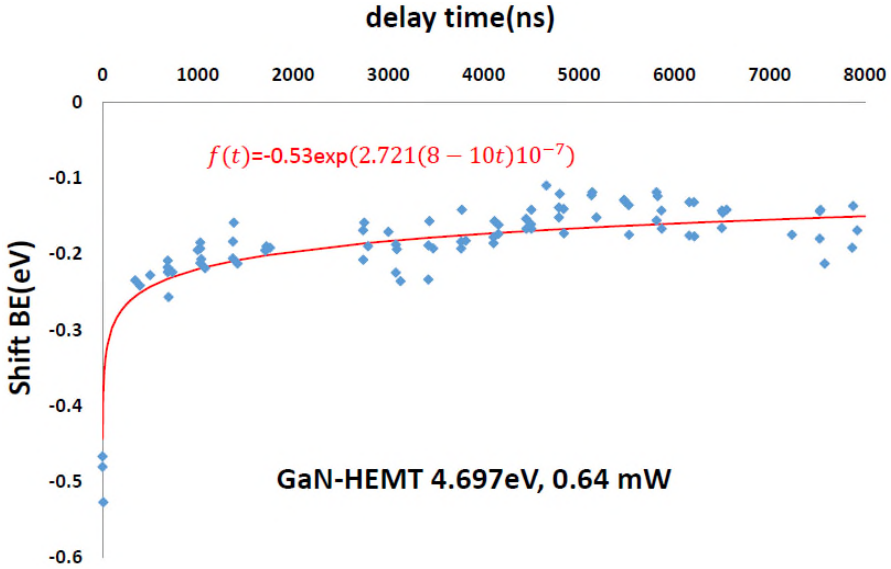

Fig. 1 time-resolved soft x-ray photoelectron spectroscopy of GaN-HEMT.

In the experiments, we foucused on the presence/absence of the two-dimensional electron gas (2DEG), i.e. the n-type GaN samples with and without 2DEG. Simultaneously, we investigated the effect of the pump photon energy, below (3.1 eV) and above (4.7 eV) of the bandgap of GaN. In the analysis using the equation,

$$V_{\mathrm{SPV}}(t) = -\eta kT \ln\left[1 - \left\{1 - \exp\left(-\frac{V_{\mathrm{SPV}}(0)}{\eta kT}\right)\right\} e^{-t/\tau_s}\right]$$

the time-resolved parameters varies with the presence and absence of 2DEG as well as the pump photon energy. Interestingly, the presence of 2DEG makes η larger. This should be

closely related with the high-frequency device operation of the GaN-HEMT. This relation is currently being analysed in deital. The photon energy varies the initial surface photovoltage. This can be explained by whether the photon absorption is direct or surface-states assisted.

This work was carried out in collaboration with Prof. Matsuda group and Sumitomo Electric Industries.

REFERENCES

[1] N. Nagamura, K. Horiba, S. Toyoda, T. Kurosumi, T. Shinohara, M. Oshima, H. Fukidome*, M. Suemitsu, K. Nagashio, and A. Toriumi, Applied Physics Letters, 102. (2013), pp. 246104.
[2] H. Fukidome*, K. Nagashio, N. Nagamura, K. Tashima, K. Funakubo, K. Horiba, M. Suemitsu, and M. Oshima, Applied Physics Express, 7. (2014), pp. 065101-1-065101-4.
[3] R. Suto †, G. Venugopal. K. Tashima, N. Nagamura, K. Horiba, M. Suemitsu, M. Oshima, and H. Fukidome*, Materials Research Express, 3 (2016), pp. 075004-1-075004-5.
[4] H. Fukidome et al. Scientific Reports, being revised.

MICROSCOPIC INVESTIGATIONS OF GRAPHENE/HEXAGONAL BN INTERAFACE ELECTRONIC STATES

Hirokazu Fukidome
Research Institute of Electrical Communication, Tohoku University

The interface of graphene with gate insulators deteriorates device performances. The use of hexagonal boron nitride (h-BN) is supposed to be one of the effective solutions because h-BN is atomically thin and flat, and does not contain charged impurities. In fact, it was shown that the use of h-BN suppresses the deterioration of graphene devices. The interface electronic states between h-BN and graphene is thus the key point in obtaining high-performance graphene devices.

To clarify the interface electronic, we have used 3D nano-ESCA. This instrument is suitable for clarifying the interface electronic states because it enables to nanoscopically probes electronic states by using nano-focused x-ray [1-3].

The sample used in this study was formed by epitaxial graphene growth on SiC, followed by h-BN deposition using the so-called Scotch-tape method, as shown in Fig. 1. The h-BN deposition on epitaxial graphene on SiC was confirmed by spatially-resolved Raman spectroscopy and cross-sectional transmission electron microscopy (Fig. 1). In the Rmaan spectra, the peaks due to BN (1360 cm^{-1}) and graphene (2700 cm^{-1}). The cross-sectional transmission electron microscopy clearly visualized that planar few-layer h-BN is deposited on monolayer graphene epitaxially grown on the SiC substrate.

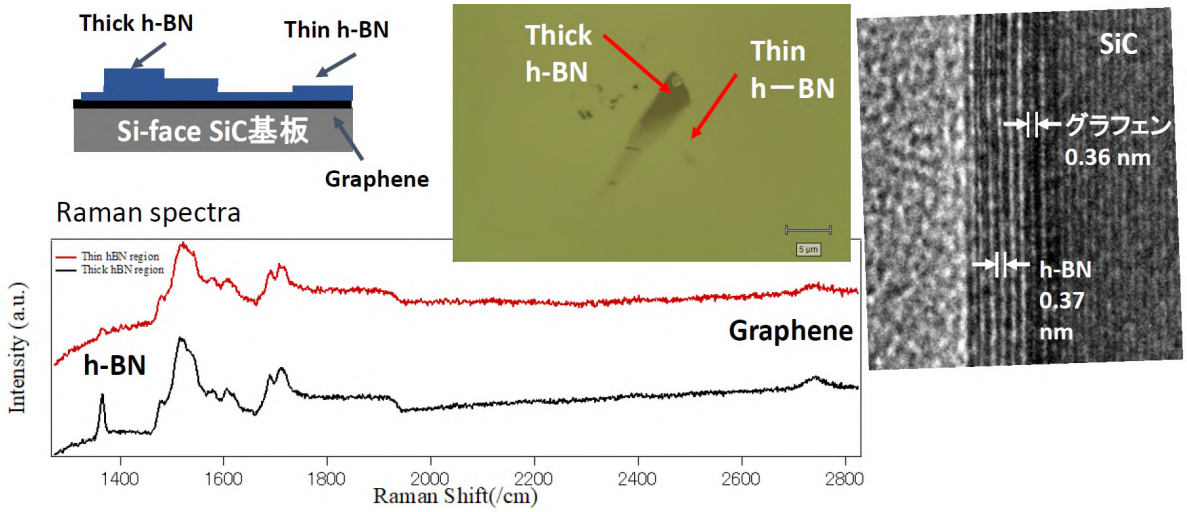

Fig. 1 Schematics of graphene/h-BN sample used in this study.

The interface electronic states of graphene and h-BN was investigated nanoscopically by using 3D nano-ESCA, as shown in Fig. 2. The binding energy of neutral graphite was measured to be 284.45 eV. Considering this value, graphene is n-doped regardless of the presence of h-BN. In the lateral direction, the amount of doping between the region of the graphene/SiC and that of BN/graphene/SiC varies at the interface between these regions. The results indicates the presence of h-BN increases the amount of electron doping of graphene. The charge transfer at the lateral interface is quantitatively analysed, as in the similar manner with our previous work [1].

This work coworked with Prof. Oshima, Dr. Nagamura, Dr. Akai, and Sumitomo electric industries.

REFERENCES

[1] N. Nagamura, K. Horiba, S. Toyoda, T. Kurosumi, T. Shinohara, M. Oshima, **H. Fukidome***, M. Suemitsu, K. Nagashio, and A. Toriumi, Applied Physics Letters, 102. (2013), pp. 246104.

[2] **H. Fukidome***, K. Nagashio, N. Nagamura, K. Tashima, K. Funakubo, K. Horiba, M. Suemitsu, and M. Oshima, Applied Physics Express, 7. (2014), pp. 065101-1-065101-4.

[3] R. Suto †, G. Venugopal. K. Tashima, N. Nagamura, K. Horiba, M. Suemitsu, M. Oshima, and **H. Fukidome***, Materials Research Express, 3 (2016), pp. 075004-1-075004-5.

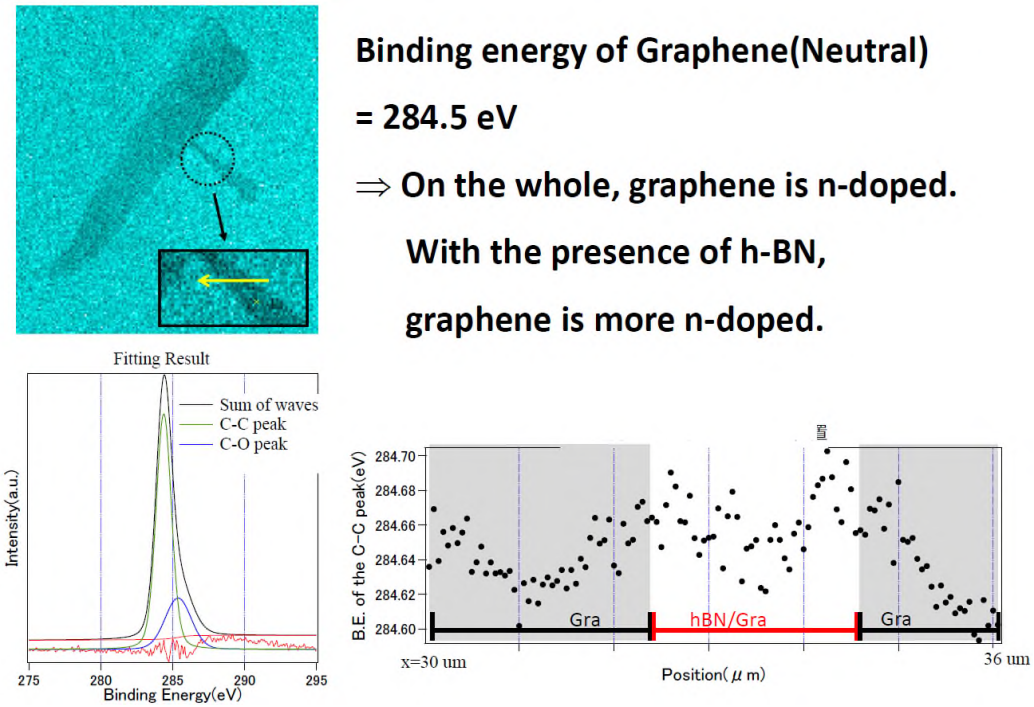

Fig. 2 3D nano-ESCA investigation of h-BN/graphene interfaces.

OBSERVATION OF TOPOLOGICAL SUPERCONDUCTIVITY ON THE SURFACE OF AN IRON-BASED SUPERCONDUCTOR

Peng Zhang,[1] Koichiro Yaji,[1] Takahiro Hashimoto,[1] Yuichi Ota,[1] Takeshi Kondo,[1] Kozo Okazaki,[1] Zhijun Wang,[2] Jinsheng Wen,[3] G. D. Gu,[4] Hong Ding,[5] Shik Shin[1]

[1]*Institute for Solid State Physics, University of Tokyo*
[2]*Department of Physics, Princeton University*
[3]*Department of Physics, Nanjing University*
[4]*Condensed Matter Physics and Materials Science Department, Brookhaven National Laboratory*
[5]*Institute of Physics, Chinese Academy of Sciences*

Topological superconductors are predicted to host exotic Majorana states that obey non-Abelian statistics and can be used to implement a topological quantum computer. By using high-resolution spin-resolved and angle-resolved photoelectron spectroscopy at ISSP, we find that the iron-based superconductor $FeTe_{1-x}Se_x$ (x = 0.45; T_c = 14.5 K) hosts topological surface states at the Fermi level; the surface states exhibit an s-wave superconducting gap below T_c. These results demonstrate that that the surface states of $FeTe_{0.55}Se_{0.45}$ are topologically superconducting, providing a simple and possibly high-temperature platform for realizing Majorana states.

Three evidences are necessary to experimentally prove that $FeTe_xSe_{1-x}$ ($x \sim 0.5$) is a topological superconductor: (i) Dirac-cone–type surface states; (ii) helical spin polarization of the surface states, which locks the spin direction perpendicular to the momentum direction; and (iii) an s-wave superconducting gap of the surface states when $T < T_c$. All these three evidences are observed in our ARPES experiments.

The observation of the Dirac-cone–type surface states. The overall band structure from the high resolution ARPES is summarized in Fig. 1A. We obtained clear parabola-like band together with Dirac-cone type band. Compare with the theory calculations [2], we conclude that the Dirac-cone–type band is the topological surface band, and the parabolic band is the bulk valence band.

The helical spin polarization of the Dirac-cone–type band. To further prove the topological nature of the Dirac-cone–type band, we measured their spin polarization. Two EDCs at the cuts indicated in Fig. 1B were measured. If the Dirac-cone–type band comes from the spin-polarized surface states, the EDCs at cuts 1 and 2 should show reversed spin polarizations. Indeed, the spin-resolved EDCs in Fig. 1CE, show that the spin polarizations are reversed for cuts 1 and 2, whereas the background shows no spin polarization (Fig. 1DF). These data are consistent with the spin-helical texture, which is the direct consequence of “spin-momentum locking” of topological surface states.

The s-wave gap for the topological surface band. Since iron-based superconductors generally have isotropic s-wave superconducting gaps, it is natural that the surface states also open an s-wave gap, due the proximity effect from bulk. Indeed, we observed clear s-wave gap on the surface band [3].

When the spin-polarized topological surface states open an s-wave gap, the corresponding superconducting states are topologically non-trivial. Thus, when an external magnetic field is applied, a pair of MBSs is expected to appear at the two ends of the vortices. Furthermore, if a magnetic domain is deposited on the surface, destroying superconductivity within that domain, there should be itinerant Majorana modes along the domain edge. It should be fairly easy to produce MBSs and Majorana edge modes. The relatively high T_c and facile growth of high-quality single crystals and thin films make Fe(Te,Se) a promising platform for studying MBSs and may further advance research on quantum computing.

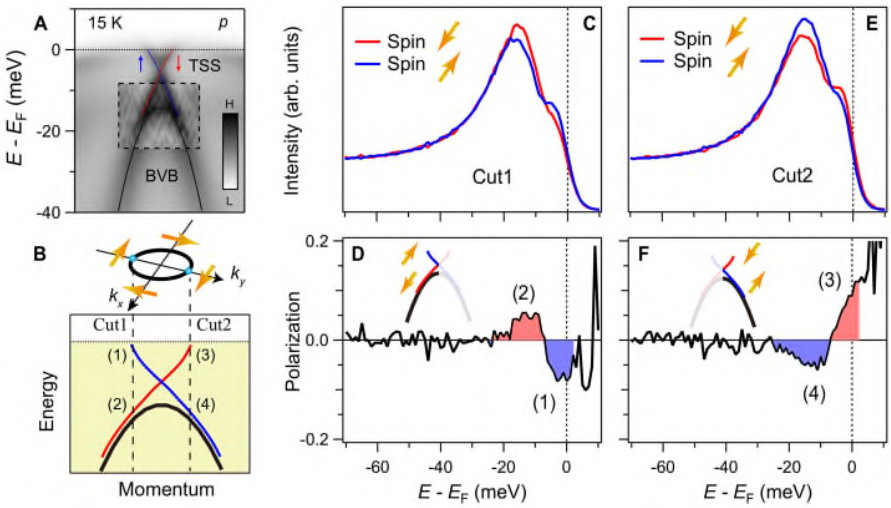

Figure 1 Dirac-cone–type surface band and its spin-helical texture. (A) Band structure measured from high-resolution ARPES. (B) Sketch of the spin-helical FS and the band structure along the sample GM direction. (C) Spin-resolved EDCs at cut 1. (D) Spin polarization curve at cut 1. (E and F) Same as (C) and (D), but for EDCs at cut 2. The measured spin polarizations are consistent with the spin-helical texture illustrated in (B).

References:

[1] P. Zhang et al., Appl. Phys. Lett. 105, 172601 (2014).

[2] Z. Wang et al., Phys. Rev. B 92, 115119 (2015).

[3] P. Zhang et al., Science 360, 182 (2018).

SPIN-POLARIZED ELECTRONIC STRUCTURE OF A SN TRIANGULAR LATTICE ATOMIC LAYER

Koichiro Yaji[1], Anton Visikovskiy[2], T. Iimori[1], K. Kuroda[1], S. Hayashi[2], T. Kajiwara[2], S. Tanaka[2], F. Komori[1], S. Shin[1]

[1]*Institute for Solid State Physics, The University of Tokyo*
[2]*Department of Applied Quantum Physics and Nuclear Engineering, Kyushu University,*

Spin-spit bands at solid surfaces have been extensively studied not only because of fundamental interests but also spintronic applications. Symmetry of the crystal surface plays an important rule in determining the nature of the spin splitting and the spin texture of a two-dimensional band [1]. Especially, a K point of the surface with three-fold symmetry is of interest due to the emergence of peculiar spin-polarized bands. For example, a Zeeman-type spin splitting with out-of-plane spin polarization appears at the K point of Tl/Si(111)-(1x1), where the surface structure belongs to the plane group of *p*3*m*1, and thus the symmetry of the K point is C_3 [2]. On the other hand, in the case of Bi/Si(111)-($\sqrt{3}\times\sqrt{3}$)R30° that belongs to the plane group of *p*31*m*, a Rashba-type spin-splitting was found at the K point having the symmetry of C_{3v} [3]. Here we point out that only the symmetry of the crystal lattice has been considered for interpreting the spin splitting of the bands so far. In the present study, we report presence of the both types of spin-spit bands at a K point of a triangular lattice atomic layer (TLAL) consisting of Sn atoms.

Recently, we synthesized the Sn TLAL by intercalation into the interface between graphene and SiC(0001) substrate. In this system, the intercalated Sn atoms are located at T_1 sites on the SiC(0001) surface and covered by monolayer graphene [4]. The Sn TLAL shows a (1×1) periodicity with respect to the SiC(0001) substrate. We investigated the spin-polarized electronic band structure of the Sn TLAL by (spin- and) angle-resolved photoelectron spectroscopy [(S)ARPES] at the Institute for Solid State Physics, the University of Tokyo [5].

From the (S)ARPES measurements, we found that two different types of spin splittings coexist at the K point of the Sn TLAL: one is a Zeeman-type spin splitting and another is a Rashba-type band crossing. Note that the K point has the C_3 symmetry with taking the crystal structure into account. Therefore, the Zeeman-type is consistent with the symmetry of the lattice while the Rashba-type band crossing is inconsistent. To understand the origin of the unconventional spin degeneracy at the K point, we examined the charge density distribution of the Sn-derived bands by density functional theory calculations. The calculations revealed that the charge density distribution of the Rashba-type band belongs to the plane group of *p*6*m*, meaning that the charge density distribution has the symmetry of C_{3v} symmetry at the K point. The symmetry of C_{3v} allows the Rashba-type band crossing at the K point. We conclude that the symmetry of the charge density distribution governs the nature of the spin-split bands beyond that of the lattice.

References:
[1] T. Oguchi *et al*.,, J. Phys.: Condens. Matter **21**, 092001 (2009).
[2] K. Sakamoto *et al*., Phys. Rev. Lett. **102**, 096805 (2009).
[3] K. Sakamoto et al., Phys. Rev. Lett. **103**, 156801 (2009).
[4] S. Hayashi *et al*., Appl. Phy. Exp. **11**, 015202 (2018).
[5] K. Yaji *et al*., Rev. Sci. Instrum. **87**, 053111 (2016).

SPIN INTERFERENCE OF PHOTOELECTRONS EMITTED FROM THE HIGH-TC SUPERCONDUCTOR BSCCO

Mauro Fanciulli[1,2], J. Hugo Dil[1,2]

[1] *Institute of Physics, École Polytechnique Fédérale de Lausanne, Switzerland*

[2] *Photon Science Division, Paul Scherrer Institut, Switzerland*

Copper oxide-based compounds (cuprates) are one of the most studied classes of materials among the unconventional high-T_C superconductors. They have an extremely rich phase diagram and are representative systems for the study of strong electron correlations. As such, they have been probed extensively by angle-resolved photoemission spectroscopy (ARPES), and the cuprate $Bi_2Sr_2CaCu_2O_{8+d}$ (BSCCO 2212) is a well-known example [1-3]. Despite this, there was only one photoemission study of BSCCO with spin resolution, where angle-integrated measurements exploited a resonant process (at Cu L_3 edge, hv = 931.5 eV) in order to determine the Zhang-Rice singlet character of the CuO_2-derived states [4], which are the ones near the Fermi level. We have recently performed a (non-resonant, hv = 50 eV) spin- and angle-resolved photoemission spectroscopy (SARPES) study at the Swiss Light Source [5], with the aim of determining the Eisenbud-Wigner-Smith (EWS) time delay of photoemission. Thanks to an analytical model [6], it is possible to obtain an indirect estimate of time delays from a band in the attosecond (10e-18 s) domain by measuring the variation of spin polarization with binding energy. Since our preliminary results on BSCCO [5] yields time delays sensibly larger than in the non-interacting system Cu(111) [7], the question about influence of electronic correlations on the time scale of photoemission was raised.

In January 2018 we have performed laser-based (hv = 7 eV) SARPES experiments at Kashiwa. We have measured five BSCCO 2212 samples (pure, doped with Ni 10%, and doped with Pr 5% - 7.5% - 10%) with the aim of systematically studying the EWS time delay as a function of doping. The good quality of the samples and of the measurements can be checked in the portion of Fermi surface shown in Fig. 1(a) for the pure BSCCO, where the nodal direction was aligned along the x direction. A comparison of spin polarization for two different samples is shown in Fig. 1(b) with high resolution in a small energy range. The main result is that no clear differences are observed, thus questioning the working hypothesis about influence of correlations on the time delay. However, an unexpected issue makes the interpretation about time delays difficult: the fact that no clear peak of spin polarization is observed in correspondence of the photoemission intensity peak. This is better shown in the energy distribution curve (EDC) in Fig. 2(a), where the y component of the spin polarization is plotted together with the two up and down spin channels. The spin polarization is non-zero, but flat over the whole energy range of 300 meV, even when far from the main photoemission peak at around 20 meV.

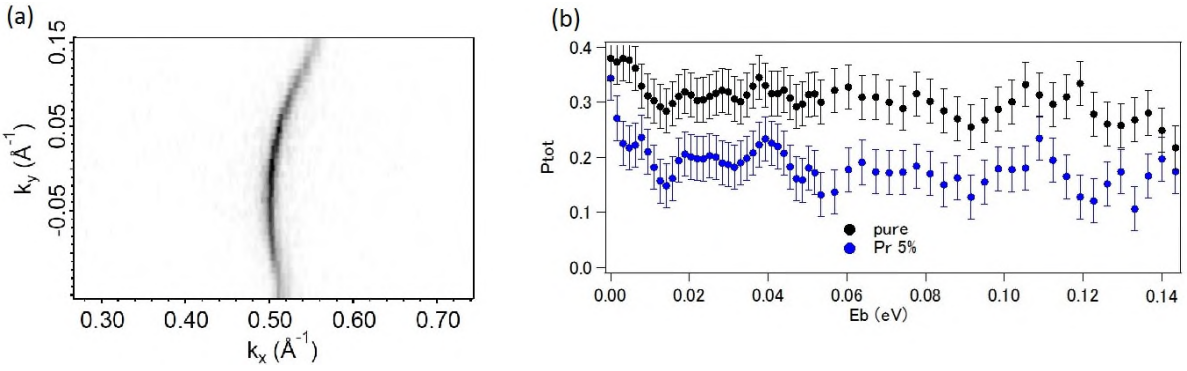

Fig. 1. (a) Portion of Fermi surface of BSCCO 2212. (b) Comparison of spin resolved EDC between pure BSCCO and doped with Pr 5%.

This peculiar flat spin polarization has currently no interpretation and might be related to the incoherent part of the photoemission spectrum. On the other hand, it is also difficult to completely exclude any possible experimental asymmetry that might influence the spin polarization signal.

At this point it is difficult to relate this spin polarization signal to the EWS time delay, and therefore to study the influence of correlations. A possible reason for the absence of a clear peak of spin polarization, as measured at the Swiss Light Source [5], is the use of a different photon energy. At the origin of the spin polarization that is related to EWS time delay lies an interference effect between different partial channels of the matrix element describing the photoemission process, where the two channels are due to different contributions in the initial or final state [6,7]. It could be that at the low photon energy of the laser, which reaches only the very low unoccupied states, only one single channel is allowed. In order to check the orbital composition of the final states and to test this possibility, spin-resolved one-step photoemission calculations are currently being performed by Prof. Jan Minár at the University of West Bohemia, Czech Republic. With the current implementation of the possibility to use 11 eV photon energy we hope to be able to see the interference channel in the near future.

An observation that supports the argument of a single transition channel is the measurement shown in Fig. 2(b), where the photoemission intensity is plotted as a function of linear light polarization angle (with 180 deg corresponding to p polarization). Fitting the data with a function that describes interference of two transitions [8], the obtained weight of one channel is larger than 95%. Since the degree of linear polarization of the used laser is of a similar value, this data is consistent with the single channel hypothesis.

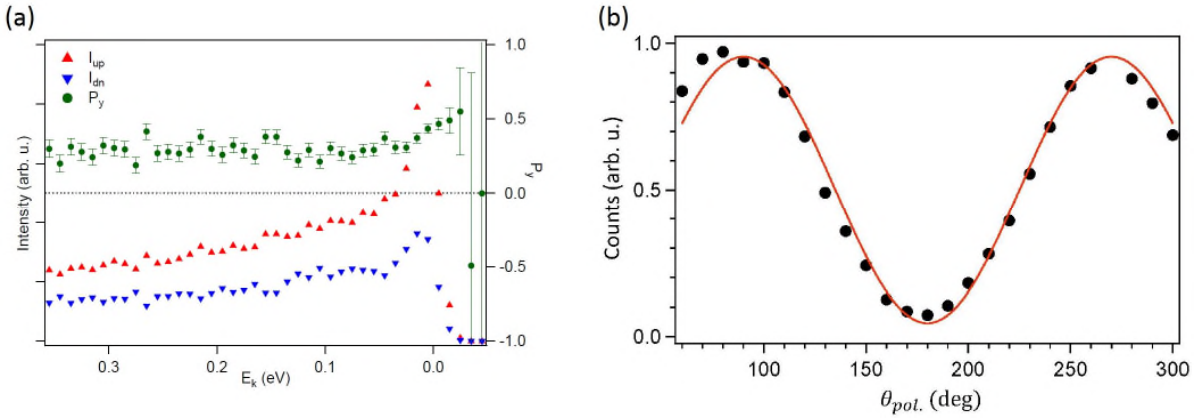

Fig. 2. (a) spin-resolved EDC on pure BSCCO 2212. The y component of spin polarization is flat also far from the photoemission peak. (b) Photoemission intensity as a function of light polarization angle.

Besides these measurements we performed SARPES experiments using different light polarizations on ferroelectric α -GeTe(111) films. High quality data was obtained which is now being prepared for publication together with 1-step photoemission theory.

REFERENCES

[1] A. DAMASCELLI ET AL., REV. MOD. PHYS., 75, 473 (2003)
[2] H. ANZAI ET AL., NAT. COMM. 4, 1815 (2013)
[3] M. HASHIMOTO ET AL., NAT. PHYS. 10, 483 (2014)
[4] N. B. BROOKES ET AL., PHYS. REV. LETT. 87, 23 (2001)
[5] M. FANCIULLI ET AL., PHYS. REV. B, 95, 245125, (2017)
[6] M. FANCIULLI AND J. H. DIL, ARXIV 1806.05895 (2018)
[7] M. FANCIULLI ET AL., PHYS. REV. LETT. 118, 067402 (2017)
[8] K. KURODA ET AL., PHYS. REV. B 94, 165162 (2016)
[9] M. FANCIULLI, PHD THESIS, EPFL LAUSANNE (2018)

STUDIES ON FINITE TEMPERATURE EFFECTS OF HALF-METALLIC FERROMANGETS BY BULK-SENSITIVE HIGH-RESOLUTION SPIN-RESOLVED PHOTOEMISSION SPECTROSCOPY

Hirokazu Fujiwara[1], K. Terashima[2], Y. Yano[1], W. Hosoda[1], T. Wakita[2], K. Yaji[3], A. Harasawa[3], K. Kuroda[3], S. Shin[3], Y. Muraoka[1,2], T. Yokoya[1,2]

[1]*Graduate School of Natural Science and Technology, Okayama University, Okayama 700-8530, Japan*

[2]*Research Institute for Interdisciplinary Science, Okayama University, Okayama 700-8530, Japan*

[3]*Institute for Solid State Physics, The University of Tokyo, Kashiwa, Chiba 277-8581, Japan*

Half-metallic ferromagnet (HMF) is a crucial material for spintronics devices because of its 100% spin polarization of the density of states (DOS) at the Fermi level (E_F).[1] CrO_2 was predicted to be a HMF by first-principle calculations.[2] As a notable advantage, at low temperatures, CrO_2 always shows almost 100% spin polarization which is the highest value in candidates for HMFs.[3] However, magnetoresistance studies using magnetic tunnelling junctions reported that the spin polarization decreased drastically with increasing temperature. Accordingly, CrO_2 behaves as 'normal' ferromagnetic metal above 50–100 K.[4] The magnitude of the spin depolarization seen in the magnetoresistance behavior is much greater than that of macroscopic magnetization measured by SQUID. As one of the reasons of the precipitous depolarization, it has been suggested that an electron–magnon interaction broadens bandwidth of conduction minority spin bands and the tail of the minority spin states comes across E_F, which can permit spin-flip scattering of the conducting majority spin electrons into the minority spin states.[1] The minority spin tail state is so-called non-quasiparticle (NQP). Although the indication of existence of the NQP states have been suggested in several tunnelling magnetoresistance studies,[5] there is no direct evidence for the NQP in HMFs at present. In this study, in order to demonstrate the existence of the NQP states, we performed high-resolution spin-resolved photoemission spectroscopy (SRPES) on CrO_2 films with a focus on the close vicinity of E_F with an energy scale of sub-meV.

All of the spin-resolved PES data of $CrO_2/TiO_2(100)$ epitaxial film were acquired by the laser-based spin- and angle-resolved photoemission spectroscopy (ARPES) apparatus at the Institute for Solid State Physics at the University of Tokyo.[6] The photon energy and energy resolution were 6.994 eV and 30 meV, respectively. We magnetized the samples along the magnetic easy axis ([001] direction) by bringing the samples close to a magnet at room temperature.

In Fig. 1(a), a clear Fermi edge was observed in the majority spin spectrum while no states at E_F with an energy gap of 100 meV below E_F were observed. These features are just those of half-metallic ferromagnet. However, in bulk-sensitive SRPES studies, the gap size of the minority spin state is estimated to be 500 meV below E_F at 40 K where the degree of spin polarization is 100 % independent on binding energy.[7] The present minority spin energy distribution curve (EDC) and spin polarization is inconsistent with those of the bulk-sensitive SRPES study. This inconsistency can be attributed to the difference of the surface sensitivity of these measurements. Therefore, in our measurements by the laser, we may observe non-negligible intensity from the surface contaminants in addition to that of CrO_2. Based on this picture, the background seen in the minority spin spectrum at 10 K in Fig. 1(a) can be identified to be the tail of the electronic states of the surface contaminants as Cr_2O_3 which has a peak at 2 eV with no Fermi edge.[8] Since we underestimate the spin polarization when non-negligible unpolarized background exists in a SRPES spectrum, we should remove the

background to obtain intrinsic values of spin polarization.[9] Therefore, we subtracted the smoothed spectrum of the minority spin one at 10 K from both majority and minority spin spectra at any temperatures.

Up to 70 K, the spin polarization decreases in the energy range above 80 meV, with the same binding-energy dependence. Above 80 K, we found that the spin polarization evidently dropped toward E_F. The spectral shape of the spin polarization clearly bends at E_B = 10 meV and the spin polarization drops toward E_F. Such a bending shape of the spin polarization is very evident at temperatures up to 120 K. Above 150 K, the bending point shifts toward the higher binding energy side and the bending structure gets broader. The tendency of the temperature dependence is consistent with the appearance of NQP state. In Fig. 1(b), with increasing temperature, from 20 K to 120 K, while the majority spin states do not change significantly, a finite state appears in the minority spin states at and above E_F. This minority state causes the depolarization near E_F. We observed the fine change of the minority spin state for the first time, by using high-resolution SRPES, which implies that the experimental technique is a powerful tool to investigate the spin-resolved electronic structure of spintronic materials.

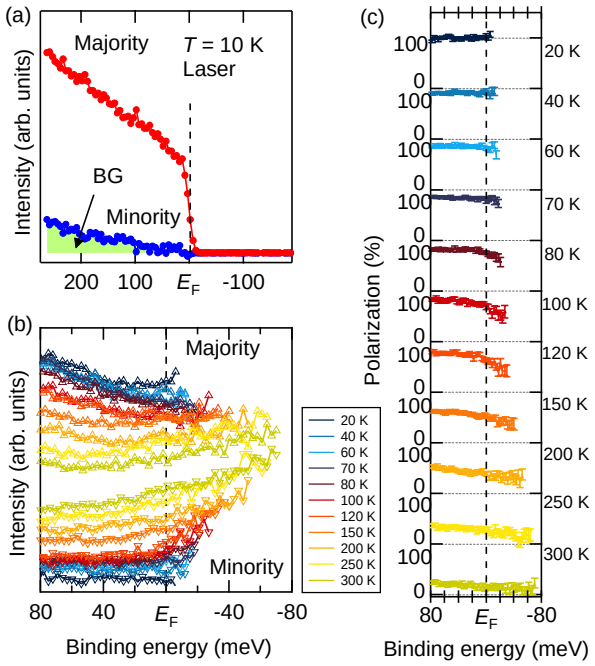

Fig. 1 (a) SRPES spectra before subtracting the background. Red and blue dots with solid lines show the majority and minority spin EDCs, respectively. **(b)** Temperature dependences of spin-resolved spectra divided by the Fermi-Dirac function at measured temperatures after background subtracted. **(c)** Temperature dependence of spin polarization.

REFERENCES

[1] M. I. Katsnelson *et al*., Rev. Mod. Phys. **80**, 315 (2008).
[2] K. Schwarz, J. Phys. F: M: Met. Phys. **16**, L211 (1986).
[3] R. J. Soulen Jr. *et al*., Science **282**, 85 (1998).
[4] J. M. D. Coey *et al*., Phys. Rev. Lett. **80**, 3815 (1998).
[5] L. Chioncel *et al*., Phys. Rev. Lett. **100**, 086402 (2008).
[6] K. Yaji *et al*., Rev. Sci. Instrum. **87**, 053111 (2016).
[7] H. Fujiwara *et al*., Appl. Phys. Lett. **106**, 202404 (2015).
[8] C. A. Ventrice Jr. et al. J. Phys.: Condens. Matter **19**, 315207 (2007).
[9] P. D. Johnson, Rep. Prog. Phys. **60**, 1217 (1997).

STUDIES ON ELECTRONIC STRUCTURES IN HALF-METALLIC FERROMAGNET CoS_2 BY HIGH-RESOLUTION SPIN- AND ANGLE-RESOLVED PHOTOEMISSION SPECTROSCOPY

Hirokazu Fujiwara[1], K. Terashima[2], T. Wakita[2], Y. Yano[1], W. Hosoda[1], K. Yaji[3], A. Harasawa[3], K. Kuroda[3], S. Shin[3], A. Teruya[4], M. Kakihana[4], M. Hedo[5], T. Nakama[5], Y. Ōnuki,[5] Y. Muraoka[1,2], and T. Yokoya[1,2]

[1]*Graduate School of Natural Science and Technology, Okayama University, Okayama 700-8530, Japan*
[2]*Research Institute for Interdisciplinary Science, Okayama University, Okayama 700-8530, Japan*
[3]*Institute for Solid State Physics, The University of Tokyo, Kashiwa, Chiba 277-8581, Japan*
[4]*Graduate School of Engineering and Science, University of the Ryukyus, Nishihara, Okinawa 903-0213, Japan*
[5]*Faculty of Science, University of the Ryukyus, Nishihara, Okinawa 903-0213, Japan*

Transition metal dichalcogenide compounds with pyrite-type structure show various magnetic and electronic properties.[1] CoS_2 is a ferromagnetic metal with a Curie temperature of 122 K.[2] CoS_2 was predicted to be a half-metallic ferromagnet by first-principle calculations.[3,4] This is supported by a fact that its magnetic moment is 0.92 μ_B/Co which is close to 1 μ_B/Co in a low-spin state of Co^{2+} (S = 1/2 and g = 2).[2] However, it is expected that Co 3*d* electrons are strongly correlated each other, which suggests that the electronic structure can be renormalized and deviated from that predicted from band calculations.[5] Therefore, the electronic structure must be determined experimentally to reveal its half-metallicity. In this report, we demonstrate the spin-resolved electronic structure of CoS_2 revealed by high-resolution spin- and angle-resolved photoemission spectroscopy (SARPES).

All of the SARPES data of a CoS_2 single crystal were acquired by the laser-based SARPES apparatus at the Institute for Solid State Physics at the University of Tokyo.[6] A clean surface for measurements was obtained by *in situ* cleaving of the sample. We magnetized the samples along the [010] direction by bringing the samples close to a magnet below the Curie temperature. *P*-polarized light with $h\nu$ = 6.994 eV was used to excite the photoelectrons. The energy resolutions of ARPES and SARPES measurements were set at 2 meV and 15 meV, respectively.

Figure 1(a)–(c) show the ARPES and SARPES intensity map along Γ–X line measured at 40 K. Highly intense bands are located around 1 eV. In Fig. 1(b) and (c), energy positions of the intense majority and minority spin bands are slightly different, namely, the energy of the majority spin band is lower than that of the minority spin band. The splitting energy is estimated to be 100 meV. These intense bands can be t_{2g} bands. Band structure calculated within LSDA have t_{2g} bands localized between –1.5 eV and –2 eV.[3,4] The energy is 0.5–1 eV smaller than that of our results. Furthermore, the exchange splitting of t_{2g} bands are approximately 1 eV which can be overestimated based on our results.

We also observed clearly spin-polarized bands located between –0.6 eV and E_F: α, β, and γ bands. These bands can be e_g bands because of correspondence to LSDA calculation. In Fig. 1(b), α band is a majority spin band. β and γ bands were observed as minority spin bands in the close vicinity of E_F as shown Fig. 1(e), while no clear majority spin bands are observed near E_F as shown in Fig. 1(d). LSDA calculations indicate that there is no minority spin band along Γ–X line in CoS_2,[3,4] which is inconsistent with our SARPES results shown in Fig. 1(e). This contradiction can be attributed to overestimation of the exchange splitting in LSDA calculations. In LSDA calculations, a band corresponding to α band is located at –0.75 eV at the Γ point, while α band is observed at –0.5 eV.[3,4] If the deviation is attributed to the overestimation, minority spin conduction bands should be move to the lower energy side with

the same energy scale. The studies of the LSDA calculation shows that the bottom of the minority spin conduction band along Γ–X line is located at 0.2 eV; this energy is comparable with the deviation of energy position between the theoretical majority spin band and the experimental one.[3,4] This suggests that the minority spin band may cross E_F, consistent with our results.

In summary, we performed high-resolution SARPES in order to reveal the electronic structure of ferromagnetic CoS_2. We observed a slightly spin-polarized t_{2g} bands and highly spin-polarized e_g bands. We found that a minority spin band crossing E_F exist at 40 K, demonstrating that CoS_2 is not a half-metallic ferromagnet. We also found that LSDA calculations overestimate the exchange splitting of CoS_2. This report implies that the high-resolution SARPES is a powerful tool to investigate strongly correlated ferromagnetic materials.

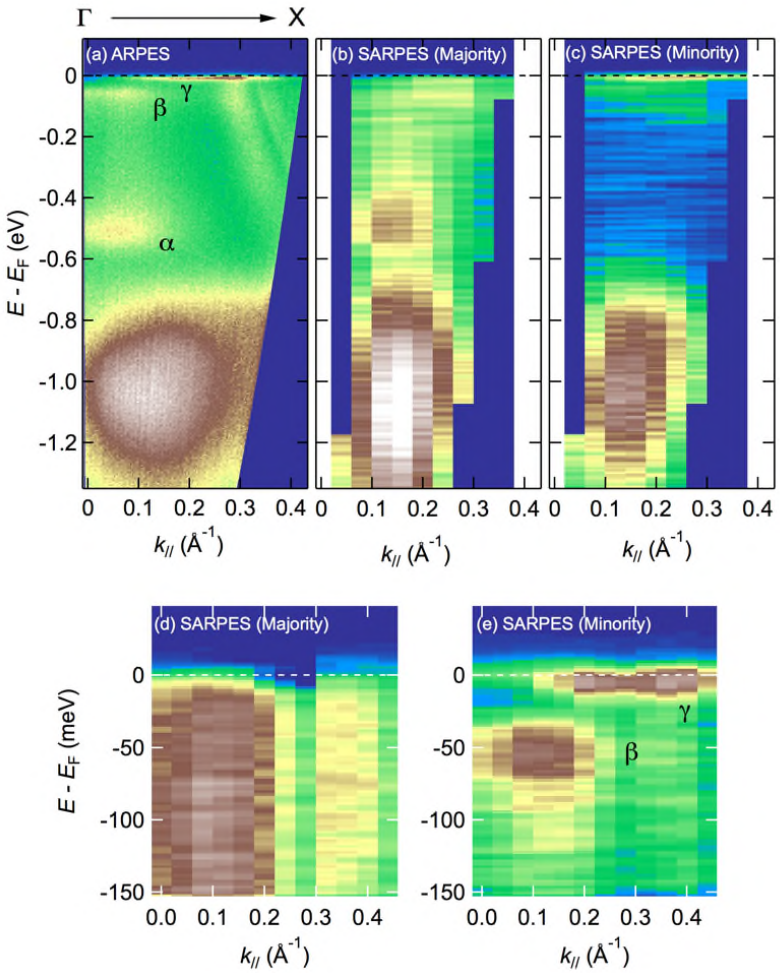

Fig. 1 (a) ARPES intensity map along Γ–X line, (b) SARPES intensity map for the majority spin bands, and (c) that for the minority spin bands of CoS2 (100) surface acquired at 40 K. (d) and (e) SARPES intensity map near E_F for majority and minority spin bands, respectively.

REFERENCES

[1] A. Wilson *et al*., Adv. Phys. **18**, 193 (1969).
[2] A. Teruya *et al*., IOP Conf. Series: Journal of Physics: Conf. Series **807**, 012001 (2017).
[3] T. Shishidou *et al*., Phys. Rev. B **64**, 180401(R) (2001).
[4] G. L. Zhao *et al*., Phys. Rev. B **48**, 781 (1993).
[5] H. Iwasawa *et al*., Sci. Rep. **3**, 1930 (2013).
[6] K. Yaji *et al*., Rev. Sci. Instrum. **87** 053111 (2016).

DISCOVERY OF SWITCHABLE WEAK TOPOLOGICAL INSULATOR STATE IN QUASI-ONE-DIMENSIONAL BISMUTH IODIDE

R. Noguchi,[1] T. Takahashi,[2] K. Kuroda,[1] K. Yaji,[1] A. Harasawa,[1] S. Shin,[1] T. Sasagawa,[2] T. Kondo[1]

[1]*ISSP, University of Tokyo*, [2]*MSL, Tokyo Institute of Technology*

The major breakthroughs in understanding topological materials over the past decade were all triggered by the discovery of the Z_2 topological insulator (TI). In three dimensions (3D), the TI is classified as either "strong" or "weak", and experimental conformations of the strong topological insulator (STI) rapidly followed the theoretical predictions [1-3]. In contrast, the weak topological insulator (WTI) has so far eluded experimental verification, since the topological surface states exist only on side surfaces which are typically undetectable in real crystals. In this work, we reveal the WTI state, for the first time, in β-Bi_4I_4 with naturally cleavable top and side planes, which is necessary for the experimental confirmation of the WTI state [4, 5].

The quasi-1D compounds β-Bi_4I_4 is formed by a stacking of Bi_4I_4 chains. From band calculations, the β-phase is in proximity of three different topological phases [4, 5]: a STI (1;110), a WTI (0;001), or even a trivial phase (0;000), sensitively depending on correction of the band gap. Experimental determination is therefore required through the direct observation

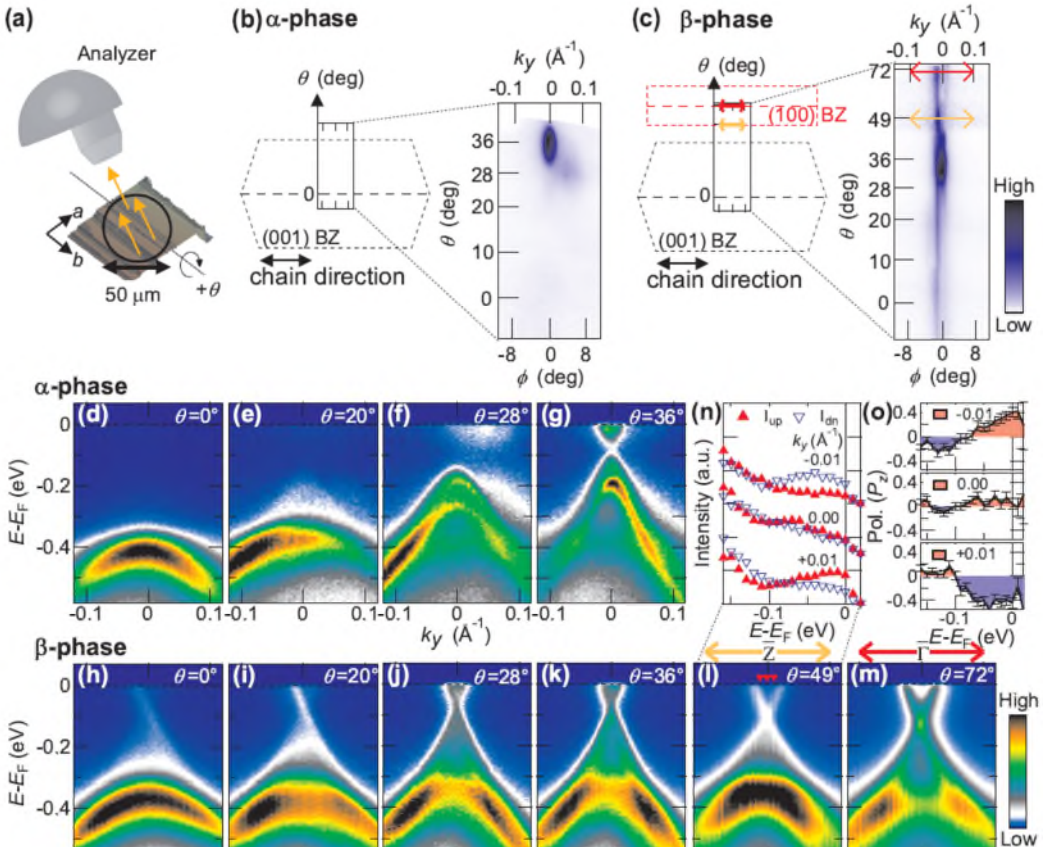

Fig. 1 (a) Experimental geometry of laser-(S)ARPES. We collect the photoelectrons at different emission angle θ with respect to the normal of the top-surface (001). (b, c) Photoelectron intensity distributions at E_F for the two materials. The intensities are integrated within 40 meV. The black and red dashed lines display the surface Brillouin zones of (001) and (100) surfaces, respectively. (d-g) and (h-m) APRES band maps taken at different θ-s in the α-phase and the β-phase, respectively. In (l) and (m), ARPES band mapping along the high-symmetry lines cut at the $\bar{Z}$ and $\bar{\Gamma}$ of the (100) surface BZ. (n, o) Spin-resolved photoelectron intensity and spin-polarizations along *z*-axis (in-plane) at θ=49°. The red triangles in (l) indicate the measurement positions.

of relevant topological surface states (TSS). There is the family material α-Bi_4I_4 with different stacking sequence, which is considered to be topologically trivial. Interestingly, these two-material phases can be selectively controlled just by temperature around room temperature, and thus opening a possible way to switch the band topology.

To verify the possible WTI state and the topological phase transition, we perform laser-SARPES at ISSP. Fig. 1(a) shows the experimental geometry Since the incident laser light with 50 μm in spot size illuminates both the terraces and facets exposed on the cleaved surface, the ARPES signals from the (001) and (100) planes are accumulated all together in the experiments. The mapping of photoelectron intensities at the Fermi energy (E_F) exhibits clearly different for the two materials [Figs. 1(b, c)]: a quasi-1D like shape is obtained in β-phase, whereas the island-like intensities are detected only around $\bar{M}$ in BZ of the (001) plane for the α-phase. Figures 1(d-g) display the ARPES maps in the α-phase at different emission angles (θ) with respect to the normal of the top-surface (001). No in-gap TSS is observed at high-symmetry momenta, the $\bar{\Gamma}$ [Fig. 1(d)] and $\bar{M}$ points [Fig. 1(g)], revealing its trivial band topology. In sharp contrast, we find a Dirac-cone like energy dispersion near E_F in the β-phase [Figs. 1(h-m)]. This band shows a quasi 1D character seen in Fig. 1(c), and it is only weakly dispersive in energy along $k_{x/z}$ (or with θ-variation). Since this state is not detected in the trivial α-Bi_4I_4, it should be TSS. Remarkably, the Dirac-state is observed even at θ=0°, or $\bar{\Gamma}$ in the BZ of the (001) surface, whereas no such state is predicted by the DFT calculations for any cases of band topology. The only possible explanation for it is that the observed quasi-1D Dirac-state is derived from the side-surface (100). The nontrivial band topology of either STI or WTI can be determined by comparing the observed surface dispersions with theoretical expectations: a large gap should be observed for a STI at the $\bar{Z}$ point, while no gap is expected for a WTI. In Figs. 1(l-m), we show the ARPES band maps obtained at θ=49° and 72°, which cut across the $\bar{Z}$ and $\bar{\Gamma}$ points along k_y, respectively, in the BZ for the (100) surface. The observed Dirac dispersions are gapless at the both k points. Moreover, in-plane spin polarizations are observed by spin-resolved measurements at θ=49°, ensuring the existence of TSS at the $\bar{Z}$ point of the (100) surface [Fig. 1(n, o)]. All of these results validate the classification of β-Bi_4I_4 as a WTI [6].

Our work will stimulate further in-depth study on exotic quantum phenomena of the WTI state as well as provide technological possibilities of functional topological materials using the topological phase transition accompanying the structural transition.

REFERENCES

[1] L. Fu and C. L. Kane, Phys. Rev. B **76**, 45302 (2007).
[2] Y. Xia *et al.*, Nat. Phys. **5**, 398 (2009).
[3] Y. L. Chen *et al.*, Science **325**, 178 (2009).
[4] G. Autès *et al.*, Nat. Mater. **15**, 154 (2015).
[5] C.-C. Liu *et al.*, Phys. Rev. Lett. **116**, 66801 (2016).
[6] R. Noguchi *et al.*, arXiv:1802.03860(2018).

SPIN-POLARIZED QUASI ONE DIMENSINAL ELECTRONIC STRUCTURE OF BI/INAS(110)-(2×1)

Takuto Nakamura[1], Yoshiyuki Ohtsubo[1,2], Ayumi Harasawa[3], Koichiro Yaji[3], Shik Shin[3], Fumio Komori[3], Shin-ichi Kimura[1,2]

[1]*Department of Physics, graduate School of Science, Osaka University*
[2]*Graduate School of Frontier Bioscience, Osaka University*
[3]*The Institute for Solid State Physics, The University of Tokyo*

Spin-polarized one-dimensional (1D) electronic structures are extensively studied as one of the promising platform for the basic research of exotic low-dimensional phenomena such as Majorana bound states [1] and spin-selective density wave formation [2]. In order to realize such spin-split 1D states, Rashba-type spin-orbit interaction (SOI) driven from space-inversion asymmetry in crystal surfaces and interfaces has been gathering attentions in this decade [1-3].

To realize sizable Rashba SOI, surface atomic structures containing heavy elements are regarded as a good candidate. Among them, we focused to the Bi/InAs(110)-(2×1) surface because its surface atomic structure is constituted with heavy Bi atoms forming quasi-1D (Q1D) atomic structure, implying anisotropic surface states [4]. Despite such interesting surface atomic structure, the detailed surface electronic structure, especially its spin polarization, has never been studied so far.

In this work, we have found the spin-polarized Q1D state on Bi/InAs(110)-(2×1) surface. The band structure and spin polarization of the Bi/InAs(110)-(2×1) surface electronic states were measured by laser-based angle-resolved photoelectron spectroscopy (ARPES) and spin-resolved ARPES (SARPES) at the Institute for Solid State Physics [5]. For the SARPES measurements, the photon-incident plane was (001), and the electric-field vector of the linearly polarized photons were normal to the incident plane (001). The InAs(110) surface was prepared by cleaving the side face of the InAs(001) wafer in an ultra-high vacuum chamber. Then, Bi were evaporated at room temperature. After annealing at 563 K for 15 minutes, a (2×1) periodic structure was observed by low energy electron diffraction (LEED), consistent with a previous study [4].

Figure 1 shows the ARPES intensity plot along $\overline{\Gamma}$–$\overline{\mathrm{X}}$. k_x is defined parallel to [$\bar{1}$10] direction. A pair of the hole bands lie slightly below the Fermi level, showing a semiconducting character. Figure 2 displays ARPES constant energy contour: k_y is defined parallel to [001]. The contour shape is highly anisotropic and waving along k_x, indicating that this state is Q1D state with inter-chains interaction. Since such states were not observed on the as-cleaved InAs(110) surface, they should be derived from Q1D Bi chains on the surface.

Figure 3 shows the SARPES energy distribution curves (EDCs) taken along k_x at $\overline{\Gamma}-\overline{\mathrm{X}}$ (k_y =0.00 Å^{-1}) and $\overline{\mathrm{Y}}-\overline{\mathrm{M}}$ (k_y =0.26 Å^{-1}) at 40 K. The filled (open) triangles correspond to spin polarization parallel (anti-parallel) to [001].The peaks of EDC in Fig. 3 disperse downward from $\overline{\Gamma}$. Such dispersions are consistent with the paired hole bands in Fig. 1. The spin direction of EDCs inverts together with the sign of the emission angle. Such paired parabolic dispersion with spin-polarization without breaking time reversal symmetry strongly suggests the Rashba-type spin splitting.

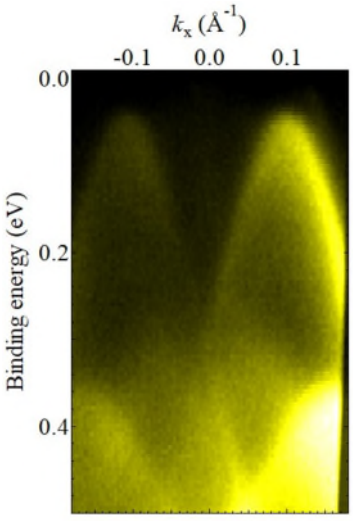

Figure 1. ARPES intensity plot of Bi/InAs(110)-(2×1) along $\overline{\Gamma}$–$\overline{\mathrm{X}}$ (k_y = 0.00Å^{-1}) measured at 40K with circular polarized photons.

Assuming parabolic dispersions with spin splitting along k_x, the size of the Rashba SOI, scaled by the Rashba parameter α_R, is evaluated as 5.5 eVÅ along $\overline{\Gamma} - \overline{X}$. This value is the largest among other 1D and Q1D Rashba systems [6, 7] and is comparable with typical giant Rashba systems such as BiTeI and Bi/Ag surface alloys [8, 9].

In summary, we have reported the spin polarized Q1D surface state on Bi/InAs(110)-(2×1) surface by using laser-SARPES. The surface state of Bi/InAs(110)-(2×1) showed large spin-polarized Q1D state driven by Rashba-type SOI. This Q1D state would be a good template for further research on spin-dependent 1D physics as well as a future application to spintronics [10]. In parallel, detailed research on spin-orbital entanglement of the Q1D states as well as the origin of the giant Q1D Rashba SOI is in progress.

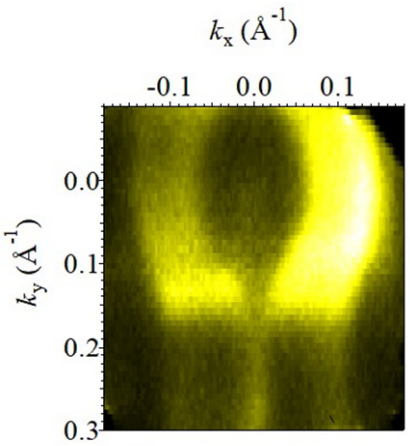

Figure 2. ARPES constant energy contour at a binding energy of 100 meV.

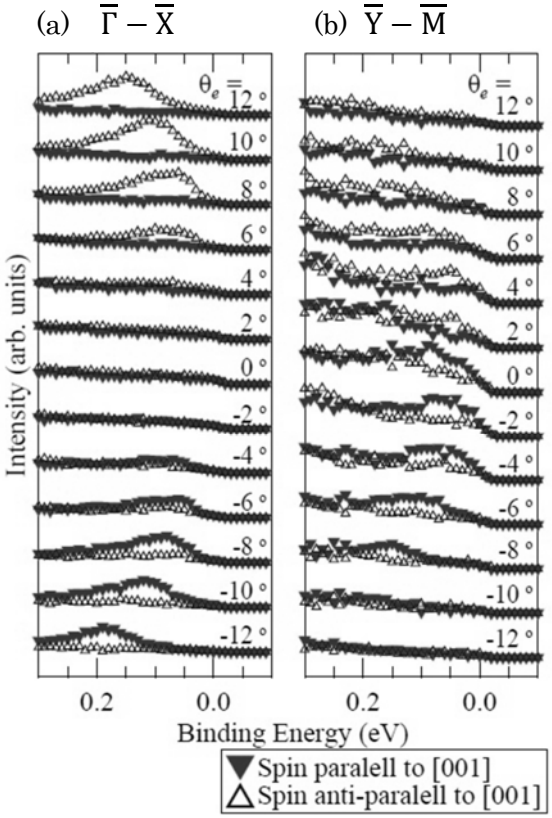

Figure 3. SARPES energy distribution curves taken along k_x at (a) $\overline{\Gamma} - \overline{X}$ (k_y = 0.00 Å^{-1}) and (b) $\overline{Y} - \overline{M}$ (ky = 0.26 Å^{-1}) at 40 K. θ_e = 10 ◦ corresponds to 0.14 Å^{-1}

REFERENCES

[1] V. Mourik *et al*., Science **336**, 1003 (2012).
[2] B. Braunecker *et al.,* Phys. Rev. B **82**, 045127 (2010).
[3] E. I. Rashba, Sov. Phys.-Solid State **2**, 1109 (1960).
[4] M. G. Betti *et al.,* Phys Rev. B **58**, R4231(R) (1998)
[5] K. Yaji *et al.,* Rev. Sci. Instrum. **87**, 053111 (2016).
[6] A. Takayama *et al.,* Phys. Rev. Lett. **114**, 066402
[7] J. Park *et al.,* Phys. Rev. Lett. **110**, 036801 (2013).
[8] C. R. Ast *et al.,* Phys. Rev. Lett. **98**, 186807 (2007).
[9] K. Ishizaka *et al.,* Nature Mater. **10**, 521 (2011).
[10] W. Han *et al.,* npj Quantum Materials **3**, 27 (2018).

Laser SARPES study on spin-orbit coupled surface states of topological insulators: helicity dependence of photoelectron spin

K. Kuroda, R. Noguchi, K. Yaji, A. Harasawa, T. Kondo, F. Komori, S. Shin
The Institute for Solid State Physics, The University of Tokyo

Introduction:

A central subject in the research for spintronic application is realization of functional capabilities to generate highly spin-polarized electrons and control its spin degree of freedom. As a promising spintronic material, a highly spin-polarized topological surface state (TSS) in three-dimensional topological insulators (TIs) has grabbed particular attentions. The TSS forms Dirac-cone-like energy dispersion and exhibits helical spin texture in momentum space due to the strong spin-orbit coupling (SOC) [1]. The peculiar spin texture protects the TSS electron from backscattering, which makes the TSS robust against perturbations. The TSS therefore can be useful as a novel spin generator and conductor.

Here, the TSS faces a new challenge for optical control over its spin properties. In addition to the helical spin texture, it was proposed that the relativistic SOC plays an important role to blend quantum states with different spin and orbitals, which gives a rise to a "spin-orbital texture" in TSSs [2, 3]. Since electric field of light directly couples with the orbitals, through the entanglement between the spin and orbital wavefunctions, it may enable us to optically manipulate the spin degree of freedom.

Recently, we use laser-SARPES at ISSP, and show a great capability of linear-polarizations to optically control photoelectron's spin in three-dimension (see Fig. 1). This light-polarization evolution of the spin orientation is successfully described by interference between spin-up or spin-down spinor wavefunctions from the initial spin-orbital textures [4, 5]. In this report, we here extend this photoemission model to include circular polarization effect that is considered as a superposed field of *p*- and *s*-polarizations with a relative phase of $\pi/2$. We demonstrate that the rotation of the excited photoelectron's spin follows the coherent optical superpositions.

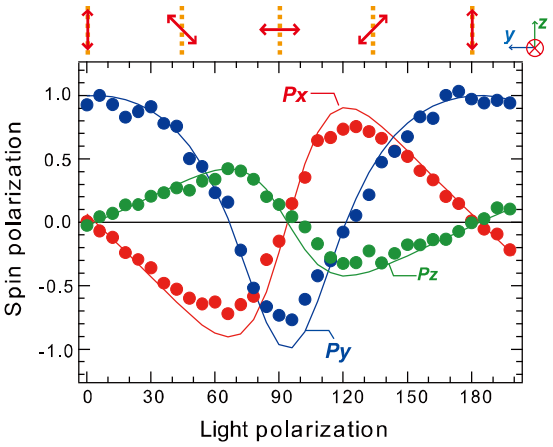

Figure 1: Plots of previously observed spin polarizations for *x*, *y* and *z* axis of the TSS as a function of the linear-polarization angle (θ) with respect to the mirror plane at k_x=−k_F [4]. At θ=0°, the electric field of the laser is aligned in the *x*-*z* plane [see Fig. 2(a)] and thus *p*-polarization. From 0° to 90°, the electric field changes from *p*- to *s*-polarization, and becomes *p*-polarization again at θ=180°.

Experimental:

Laser-SARPES was performed at laser-SARPES machine at ISSP with high-flux 6.994-eV laser light [6]. The laser-SARPES machine is based on two high-efficient VLEED spin-polarimeters and the hemispherical analyzer with photoelectron deflector function (ScientaOmicron DA30L). This spectrometer can resolve spin polarization components of photoelectrons for in-plane ($P_{x,y}$) and out-of-plane (P_z) orientation. During the measurement, the sample temperature was kept below 20 K, and instrumental energy and angular resolutions were set below 20 meV and 0.7°, respectively. Experimental configurations is shown in Fig. 2(a) where the light incidence plane and the detection plane match the mirror plane of the crystal (*x*-*z* plane). The *p*- (*s*-) polarization excites *even* (*odd*) parity orbitals with respect to the mirror plane [4, 5]. The light polarizations are controlled by half- and quarter-waveplates.

Results:

Figure 2(b) represents spin-integrated ARPES intensity map for Bi_2Se_3 along the Γ-M high

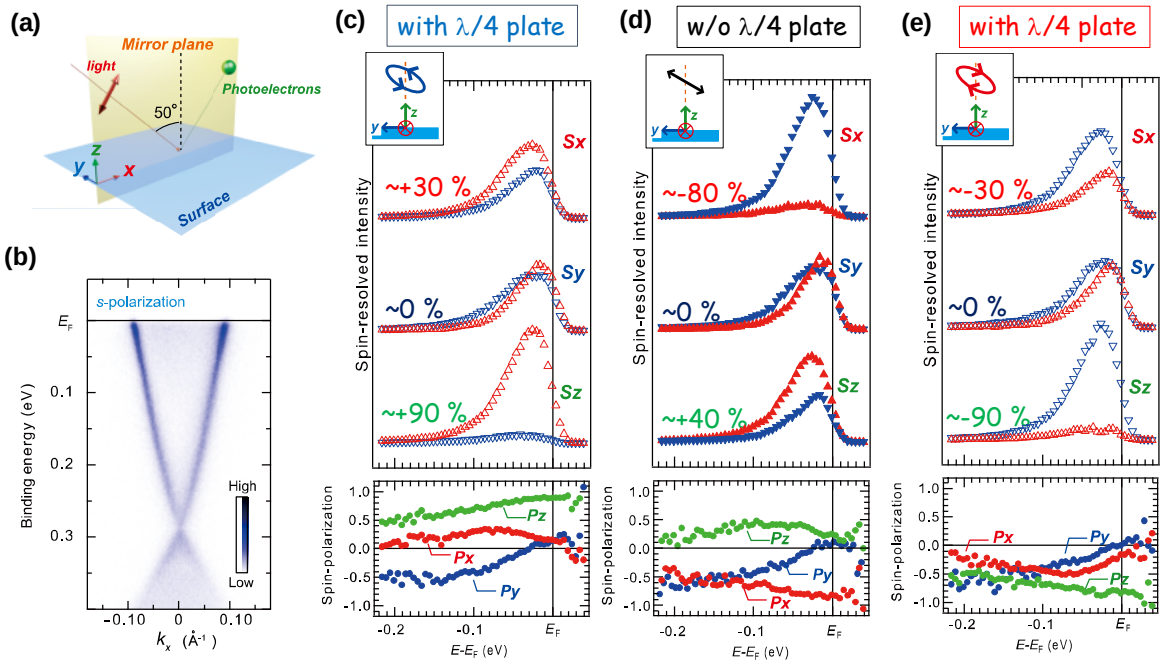

Figure 2: (a) Experimental geometry. In the geometry, according to pure orbital selection rule, *p*- and *s*-polarized lights selectively excite spin-up and spin-down states, respectively. (b) ARPES intensity map, showing Dirac-cone like energy dispersion of TSS in Bi_2Se_3. (c-e) Spin-resolved photoemission intensities and the corresponding spin polarization as a function of binding energy obtained by various light polarizations, (c) left-handed elliptical, (d) tilted linear, (e) right-handed elliptical (see the inset). These light polarizations are obtained by a combination of half- and quarter-waveplates for 7eV laser. The obtained spin axes correspond to those in (a).

symmetry line. The data well resolves the sharp TSS with the Dirac-cone-like energy dispersion of the surface state. All of the SARPES measurements shown below are performed at (k_x, k_y) = (–k_F, 0), which is the same *k* point [4]. By using tilted linear polarization with half-waveplate and without quarter-waveplate, we see almost no-spin polarization along *y* axis while large spin-polarizations for *x* and *z*. In particular, the size of the spin polarization for *x* achieves 80 %. This behavior is quite consistent with the previous result as shown in Fig. 1 (θ~65°).

As a heart of our interests, we now verify helicity dependence, which gives an optically induced "phase" in the photoemission interference process, since the light has own relative phase (–π/2 or +π/2) depending on its helicity. To demonstrate this, we now fix the half-wave plate angle, to produce the tilted polarization, and insert quarter-waveplate. The resulting light field is expected to be elliptical with a long-axis along the tilted linear-polarization [see the inset of Figs. 2(c) and 2(e)]. Depending on the quarter-wave plate angle, we tune its helicity with either left-handed (–π/2) or right-handed (+π/2). By the left-handed polarization [see Fig. 2(c)], one can immediately see the impact of the helicity by looking at the data for *x* and *z* compared to those for the linear polarization [Fig. 2(d)]. Apparently, there is a cross relation in not only the size of the spin-polarization but also the shape of the spectra. This cross relation indicates that the resulting spin-polarization rotates by –π/2 in P_x-P_z plane. Moreover, the similar relation is clearly observed for the right-handed [Fig. 2(e)], and but the resulting spin direction is completely opposite with respect to that obtained in the left-handed [Fig. 2(c)]. These data unambiguously demonstrate that the light helicity induce "phase" in the spin matrix elements which is directly visualized by laser-SARPES.

References:

[1] M. Z. Hasan, C. L. Kane, Rev. Mod. Phys. **82**, 3045 (2010).
[2] H. Zhang, C.-X. Liu, S.-C. Zhang, Phys. Rev. Lett. **111**, 066801 (2013).
[3] Y. Cao *et al*., Nature Phys., **9**, 499 (2013).
[4] K. Kuroda, K. Yaji *et al*., Phys. Rev. B **95**, 165162 (2016).
[5] K. Yaji, K. Kuroda *et al*., Nature Commun., **8**, 14588 (2017).
[6] K. Yaji *et al*., Rev. Sci. Instrum., **87**, 053111 (2016).